March 3, 2008; CEA Saclay
Internal report: IRFU-08-21
EURISOL DS/Task11
www.eurisol.org

Optimization of in-target yields for RIB production: Part I: direct targets

Sébastien Chabod [1,2], Nicolas Thiollière [1], Jean-Christophe David [1], Valentin Blideanu [3], Diane Doré [1], Dana Ene [1], Benjamin Rapp [1], Danas Ridikas [1]

[1] CEA-Saclay, Irfu/Service de Physique Nucléaire, 91191 Gif-sur-Yvette, France
[2]LPSC, Université Joseph Fourier Grenoble 1, CNRS/IN2P3, Institut Polytechnique de Grenoble, 38000 Grenoble, France
[3] CEA-Saclay, Irfu/Service d'Expertises Nucléaires en Assainissement et Conception, 91191 Gif-sur-Yvette, France

Abstract:
In the framework of the EURISOL DS project and within Task 11, we have performed in-target yield calculations for different configurations of thick direct targets. The production rates have been estimated using the MCNPX transport/generation code, coupled with the CINDER'90 evolution program. The yield distributions as a function of charge number Z and mass number A have been evaluated. Their production rates have been optimized for 11 selected elements and 23 of their isotopes of interest. Finally, the isotopic distributions for each of these 11 elements have been optimized in terms of the target material, its geometry, and incident proton energy.

1. Context and objectives

The EURISOL collaboration aims to design, build and operate the next generation radioactive ion beam (RIB) facility based on ISOL method in order to provide deeper knowledge in fundamental nuclear physics (study of exotic nuclei far from stability, measurements of key nuclear astrophysics cross sections, tests of theories beyond standard model, possible use of neutrino factories, etc.) beyond, say, 2015. To meet this objective, the EURISOL network had consequently launched a design study to investigate the eligible technological options with the first guidelines available now in Ref. [1]. The proposed driver accelerator is a multi megawatt linear superconducting proton machine with incident energy around 1 GeV with a possibility to accelerate some light ions as projectiles, namely d and ^{3}He ions. The future EURISOL facility will use two different target configurations:

- Direct configuration: A 100 kW proton beam is focalized on a thick target to produce RIB directly.
- Two-stage configuration: A multi MW protons beam is directed on a converter target to generate high neutron fluxes by spallation-evaporation process. Exotic nuclei are

then produced by fission reactions induced by the secondary neutrons on actinide targets surrounding the converter.

Finally, the extracted and ionised radioactive nuclei will be post-accelerated up to 150 MeV per nucleon in order to provide high intensity and high quality RIB to the experimental areas.

In the framework of the EURISOL DS and within Task 11, we aim to estimate and optimize the nuclei production rates using direct targets option. To achieve this objective, we have consequently performed calculations of the in-target isotope yields for different configurations, by varying several intrinsic or external parameters such as the target chemical compositions, target volumes, or the incident proton energies. The production rates have been simulated using the MCNPX reaction-transport code, coupled with the CINDER'90 evolution code. The methodology of our approach is described in part 2. In part 3, we present the nuclei production rates as a function of their charge number Z and mass number A. In parts 4 and 5, we conduct the yield optimization for 11 elements of interest and study their isotopic distributions to estimate the individual secondary beams before the conclusions are drawn at the end. Finally, most of the figures are placed in Appendices.

2. Tools and database

Radioactive nuclei are produced by spallation reactions induced by the primary beams or by the secondary particles. According to the material used fission process can occur and, in the case of double-stage target, exotic nuclei production is exclusively based on fission reactions induced by the secondary (rapid or thermal) neutrons[*]. Moreover the nuclei obtained are also the result of decay chains of radioactive parents. To estimate the production rates of the nuclei of interest, we have consequently carried out simulations of these nuclear processes using event generators, transport and evolution codes.

2.1. Overview of the simulation parameters for direct targets

In order to achieve a full picture of RIB predictions, a complete optimization study requires tests of a huge number of target configurations. Among the primary parameters which should be studied are evidently:

- The physical characteristics of the production targets. We have indeed to test different types of materials (refractory or molten metals, oxides, carbides, etc.), different densities ρ (linked to the porosity and chemical state of the target), and different geometries, even if we restrict ourselves to cylinders (length L and radius R of the target).
- The beam characteristics. Different beam powers P and energies E must be explored, as these parameters directly govern the spallation processes and the nuclei production yields. In addition, we can take into account different incident particle types (p, d, or ^{3}He) and spatial distributions of the beam impact zone on the target (here we will assume that the beam has a gaussian profile with its σ defined as the full width at half maximum).

[*] It will be the subject of another report (Part II)

Following the discussions within Task 3 (direct target) [2, 3], we decided to simulate 320 different configurations of cylindrical targets, whose characteristics are summarized in Table 1. The choice of the beam spot $\sigma = R/3$ came from a previous study [3, 4]. As σ values cannot be smaller than 3 mm [3], the minimal target radius R was automatically equal to 9 mm. The other radii have been chosen to successively increase the target volume by a factor 2 for a given length. Then, we have considered different target lengths, until the Bragg peak (stopping range) is reached for each chosen material. According to the ongoing EURISOL DS, the incident proton energy will remain close to the 1 GeV level. Thus, we have selected E values ranging from 0.5 to 2 GeV in our study. Finally, as EURISOL targets are designed to stand up to 100 kW of the primary beam power, we have consequently fixed P to this maximal value, which corresponds to a 100 μA beam of 1 GeV protons. Indeed, for a given energy E, the secondary nuclei yields are proportional to the beam intensity, and consequently to the beam power.

Target material	Al_2O_3	SiC	Pb (molten)	Ta	UC_3
ρ [g.cm^{-3}]	2.0	3.2	11.4	12.5	2.418
R [mm]	9.0 – 12.7 – 18.0 – 25.5				
L [cm]	50 – 75 – 100 – 125	32 – 48 – 64 – 80	9 – 18 – 27 – 36	8 – 16 – 24 – 32	40 – 60 – 80 – 100
Beam particles	Protons				
P [kW]	100				
E [GeV]	0.5 – 1.0 – 1.5 – 2.0				
σ [mm]	$R/3$				

Table 1: Simulation parameters used for this study.

2.2. Presentation of the simulation codes and analysis steps

To obtain the production yields of the radioactive nuclei, we have called upon two different modelling tools: MCNPX and CINDER. The first one, the MCNPX 2.5.0 code [5], is based on Monte Carlo procedures and computes the transport of light particles (n, p, d, t, ^{3}He, α, π, etc.), the secondary emitted particle flux and the production rates of reaction products (spallation fragments and fission products). MCNPX uses data libraries for low energetic neutrons (E_n < 20 MeV) and models for the other reactions. It computes the complete list of the reaction products obtained for all processes (all particles) at all energies, except reactions involving low energetic neutrons (below 20 MeV). Within EURISOL Task 11, MCNPX has been extendedly benchmarked [6, 7] and it appeared that the precision of its output results remains highly sensitive to the quality of the models used to describe the spallation reactions. Taking into account the conclusions of these benchmarks, we have thus decided to use two quite different cascade/de-excitation models available within MCNPX: INCL4/ABLA [8, 9] and CEM2k [10]. Two of the most striking differences between these two models are the presence of an explicit pre-equilibrium phase in CEM2k, whereas it is considered as non-necessary in INCL4. In addition, INCL4 is coupled to the fission part computed by PROFI included in ABLA, while the RAL fission model [11] is used when CEM2k is called.

Starting from the MCNPX output files, the nuclei production rates have been extracted using the standard analysis code HTAPE3X, delivered with the main MCNPX package[†]. In order to manage statistical error and calculation time, we have performed simulations using $5x10^6$ incident particles for each configuration mentioned in Table 1.

As we mentioned earlier, the MCNPX code does not provide the reaction product yields due to low energetic neutrons (below 20 MeV). We have consequently reprocessed the MCNPX outputs with CINDER'90, a standard material evolution program [12]. CINDER can indeed simulate the nuclear reactions (capture, fission, (n,xn), (n,p), (n,d), etc.) induced by neutrons below 25 MeV. Moreover, it can also account for the nuclei loss/creation through the natural decay process. On the other hand, CINDER does not propagate the statistical uncertainties resulting from the MCNPX calculations. As a consequence, the error levels on the nuclei yields could not be estimated in this report. On the other hand, once the statistical uncertainties from the Monte Carlo approach become significant, we notice the reader about it.

For each set of target parameters (see Table 1), we performed 4 (MCNPX → HTAPE3X → CINDER) simulation cycles (see Figure 1):

- 2 for each eligible spallation models (CEM2k or INCL4/ABLA),
- then, for each model, 2 different CINDER computations: calculation of the nuclei yields by taking into account, or not, the reactions induced by the low energy secondary neutrons.

CINDER evolution times ranged from 1 ms (instantaneous nuclei production rates) to 3 months (rough estimation of the impact of exotic nuclei finite lifetimes on their production rates being at equilibrium with the decay rates). Each simulation cycle generated output files which contained the complete list of the nuclei yields.
Among these calculated yields, we wanted to study specifically the production rates of 11 nuclei of interest: 7 were given by the NUPECC board (Be, Ar, Ni, Ga, Kr, Sn and Fr) [13] and additional 4 elements, which could play a pre-eminent role in the experiments programmed within the EURISOL framework (Li, Ne, Mg and Hg) [14]. Finally, each of these elements has different isotopes of interest (ex: ^{11}Be being one-halo nucleus and ^{12}Be being two-halo nucleus with Z = 4). As a conclusion, for the 320 chosen modelling configurations, we had to analyse more than 1200 output files containing dozens of key isotopes and different evolution times. For this reason this work could only be achieved through some automatic procedures.

[†] After the HTAPE3X reprocessing step (see Figure 1), the production rates of hydrogen/helium isotopes and the yields of heavier elements are automatically displayed into two separate default files. To achieve a complete calculation of gas production inside EURISOL targets, we have consequently merged for each target configuration these two outputs in a single file, used thereafter for the CINDER evolution steps.

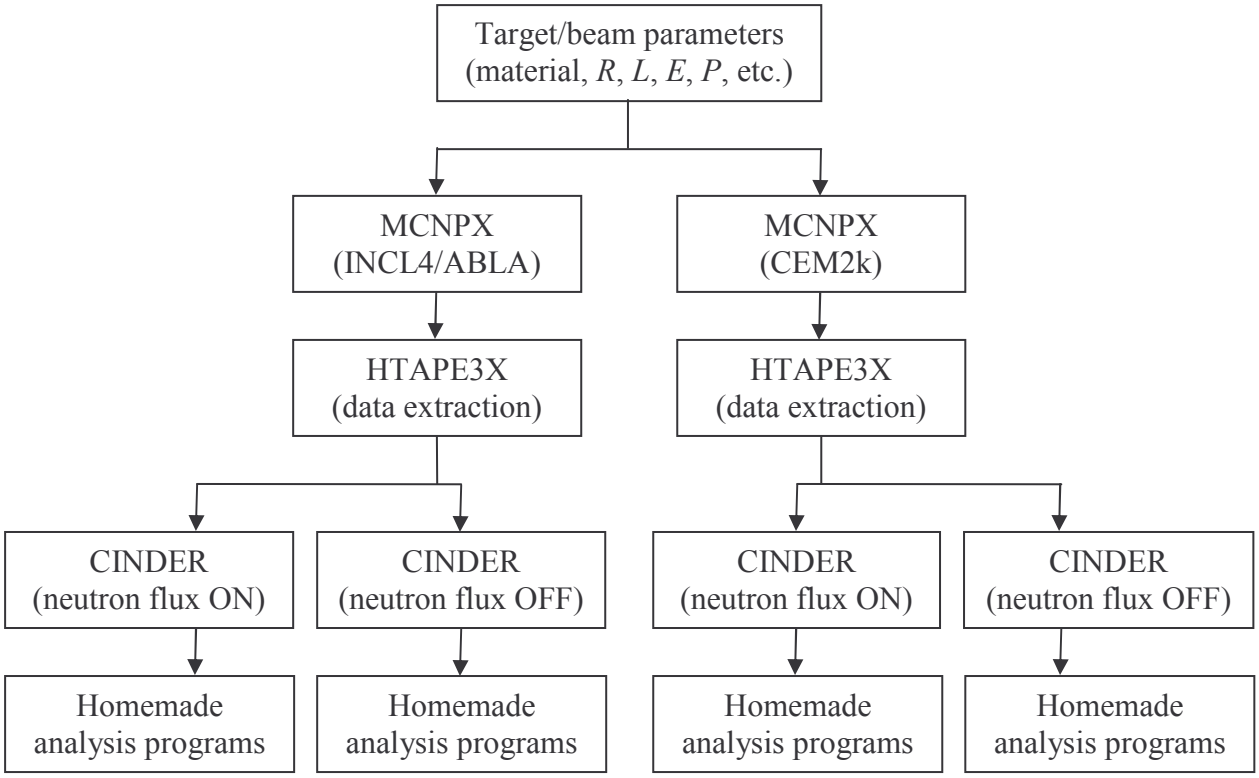

Figure 1: Simulation steps for the in-target yields calculations.

2.3. Automation of the simulation and analysis procedures

The automation of the MCNPX, HTAPE and CINDER calculations was ensured by C++ programs and UNIX routines. Their results were deployed on the branches of a directories tree in order to speed up the search for isotopes of interest (see Figure 2). The first level of the data tree regrouped the target types (direct or double-stage), the second - the spallation models used for MCNPX simulations (INCL4/ABLA and CEM2k), the third - the materials retained for the targets (lead, silicon carbide, etc. as shown in Table 1), the fourth - the radii of the targets, the fifth - their lengths, the sixth - the energies of the incident protons, and finally the output files of the simulation codes were displayed in the seventh and last level of the tree.

To perform the analysis of these results, we have then written a C++ search engine. This program called *routine* requires the data tree, a secondary program called *sub_routine* and 3 simple input files (see Appendix A). To ensure an easy navigation in the data tree, the *routine* engine accepts 11 different arguments which are linked to different analysis types and are summarized in the same Appendix A.

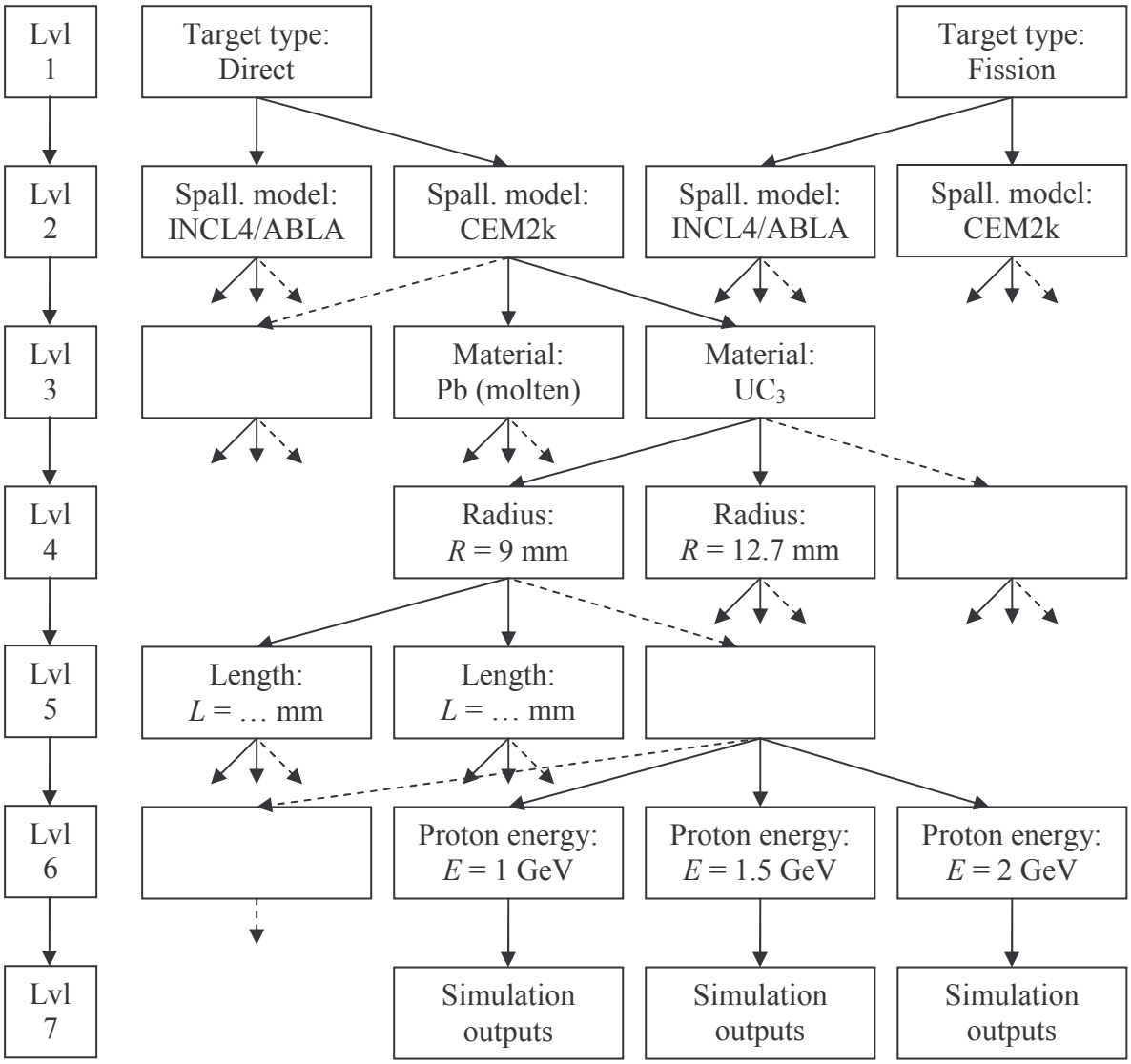

Figure 2: Organisation of the data.

3. Charge and mass distributions of the secondary nuclei

To maximize the in-target yields of exotic isotopes, we studied first their distributions as a function of charge number Z and mass number A. These distributions, reported on Figures 3 to 6, have been calculated for each target material retained in our report (see Table 1), using MCNPX simulations followed by CINDER to get the low energy neutron contribution (very short evolution time: 1 ms). To obtain the very first idea of the leading target/beam configurations, the results have been plotted for different spallation models and proton energies. Finally, to simplify this comparison work, we have decided to consider targets of identical radii (18 mm) and same masses (2 kg), i.e. different lengths due to different densities.

On Figures 3 to 6, we retrieve the characteristic shapes of the distributions, formed by successive parts from heavy to light charges and masses:

- hedges located close to the charge and mass number of each target compound element,

- decreasing evaporation slopes,
- "spallation valleys", which are progressively filled with increasing proton energy. These valleys correspond to the zone where the evaporation step of the excited target nucleus "meets" either the fission (for fissionable nuclei as Ta, Pb and U) process or another mechanism not fully understood today, namely multi-fragmentation or transition state of asymmetric splitting modes [15] for lighter nuclei.

On Figures 3 and 5, we can observe quick falls of the production rates in the $Z \approx 87$ and $A \approx 215 - 217$ regions. These falls are not artefacts of the calculation: they appear due to the very short half-lives (~ μs) of the corresponding isotopes, which rapidly decay by alpha radioactivity during the 1st ms taken into account by CINDER temporal evolution.

Z	Best material
≈ 7	Al_2O_3
≈ 15	SiC
$30 \leq Z \leq 55$	UC_3
$65 \leq Z \leq 70$	Ta
$75 \leq Z \leq 80$	Pb
$Z \geq 85$	UC_3

A	Best material
≈ 15	Al_2O_3
≈ 30	SiC
$160 \leq A \leq 180$	Ta
$185 \leq A \leq 210$	Pb
$A \geq 215$	UC_3

Table 2: Optimal target materials for the in-target production of radioactive nuclei (R = 18 mm, $M = \pi.\rho.R^2.L$ = 2 kg, P = 100 kW, spallation models = INCL4/ABLA and CEM2k. MCNPX 2.5.0 simulations followed by 1 ms CINDER'90 evolutions).

Starting from Figures 3 to 6, we have determined the optimal target materials for the production of specific elements (see Table 2). For Z and A numbers not reported in Table 2, two or more materials are eligible. Moreover, we have verified that these conclusions remain valid for calculations using both spallation models. Concerning the 11 elements of interest (see paragraph 2.2), we can observe that:

- Fr nuclei can only be produced using UC_3 targets,
- Hg isotopes can essentially be produced using Pb targets,
- Kr and Sn isotopes can essentially be produced using UC_3 targets,
- Ar, Ni and Ga nuclei can be produced both with Pb or UC_3 targets,
- Ne and Mg nuclei can essentially be produced using Al_2O_3 or SiC targets,
- Li and Be isotopes can essentially be produced using Al_2O_3, SiC or UC_3 targets.

For all these nuclei, tantalum targets seem to be not optimized for the moment. However, at this level it is important to recall that these first data deal with the direct production of isotopes inside the EURISOL targets. To obtain the corresponding secondary beam intensities, our simulated yields will have to be convoluted with the ion extraction and ionization efficiencies, estimates of which are in progress within Task 2, 3 and 11 [16]. Indeed, even if an exotic isotope is produced in high quantities, if its escape time from the target by diffusion/effusion processes reveals too long (due for example to excessive density or volume or sticking to the target material or beam lines, etc.), its natural decay will prevent it to constitute a valuable radioactive beam. Consequently, further analysis will be necessary, involving successive adjustments and final calculations using our in-target yield database.

As we can see on Figures 7 to 10, the impact of the low energetic secondary neutron flux on the instantaneous production rates (MCNPX calculations followed by 1 ms CINDER

evolutions) is almost negligible. As expected, substantial differences appear only for the nuclei very close to the target nuclei and for the fission region of uranium targets (especially in the range of fission product yields for $30 \leq Z \leq 60$ and $80 \leq A \leq 160$). We observe also an increase in the ^{9}Be production rate due to (n,α) processes on ^{12}C, and the formation of deuterium/tritium isotopes by (n,d) and (n,t) reactions on light elements.

We show on Figures 11 to 18 that the differences between INCL4/ABLA and CEM2k results are small for fission fragments around stable nuclei, and for nuclei with $Z \leq 6$. For the other nuclei, relative differences between INCL4/ABLA and CEM2k can reach almost a factor 2 and consequently lead to a 100 % modelling uncertainty on our results (far more than statistical error for most isotopes).
It is important to quote that several spallation models, including CEM2k and INCL4/ABLA codes, have been benchmarked within EURISOL framework [6, 7]. Their predictions have been tested using experimental data from ISOLDE [16, 17] and Dubna installations [18]. At this occasion, it had been demonstrated that the deexcitation model combined to CEM2k in MCNPX2.5.0 induces a high overestimation of the neutron rich/neutron deficient fission products formation, where INCL4/ABLA was doing much better. At the same time, INCL4/ABLA model is not perfect in other regions: it appeared that it overestimates the production of π^{+} particles and gives questionable results for light nuclei. As we will discover it in next section, these modelling specificities can play sometimes an important role in the prediction of the exotic nuclei production rates.

4. Production optimization of selected exotic nuclei

In this section, we present an overview of the results obtained for the 11 nuclei of interest and some of their isotopes. According to the recommendations presented in the previous sections, we have considered the targets and beam parameters described in Table 1, simulated with MCNPX 2.5.0. MCNPX calculations are followed by 1 ms CINDER'90 temporal evolutions in the low energetic secondary neutron flux. Results have been plotted for different target lengths L, spallation models and proton energies E, in order to easily visualise the best target configurations.

To conduct our optimization studies on the proton energies (see Table 1), we have assumed that the acceleration cost due to an increase in E would be higher than the cost of an increase in the beam intensity. Consequently, if two simulations conduct to equivalent nuclei yields, we will choose the lower energy configuration operating at higher intensity for a given beam power. For this reason we have divided in this section the production rates τ of the nuclei by the energy E parameter in GeV. Taking into account these remarks, the optimal proton energy for a given isotope will be then simply the energy which maximises the τ/E value. For instance, if the normalized production rate τ/E of an isotope is higher for a 1 GeV beam than for a 2 GeV beam at a given incident beam power, then it implies that the 2 GeV energy is not optimal.

To estimate the optimal lengths L and radii R of the targets, we have to remember that the exotic nuclei should still effuse and diffuse efficiently before they can be ionised and post-accelerated afterwards. As the extraction times t inevitably increase with the target

dimensions[‡], excessive volumes V will induce important losses by radioactive decay and even prevent heavy elements from reaching the target surface. Thus, we must choose L and R values that represent reasonable compromises between significant boosts of the nuclei production rates and limited volume growths. As it was done in section 3, we first considered targets of identical 18 mm radii. Then, we have reported for comparison in Figures 64 to 93 the isotope production rates as a function of R and L parameters.

4.1. Francium isotopes

Due to its heavy charge number, $_{87}$Fr element can only be generated using uranium targets. Concerning the production of ^{205}Fr (neutron deficient isotope) we observe on Figures 19 and 20 that both spallation models lead to an optimal $L \approx$ 40-60 cm uranium target irradiated with a 1 GeV proton beam. One has to note however that the production rates obtained using INCL4/ABLA and CEM2k differ by two orders of magnitude.

As long as the production of ^{231}Fr (neutron rich isotope) is concerned, we notice that CEM2k leads to null values of the production rates. Starting from ^{235}U, ^{231}Fr nuclei can be formed during spallation reactions involving 5 proton emission and the formation of a π^+ pion. Starting from ^{238}U, ^{231}Fr production can be achieved through {6 p + 2 n} or {5 p + 3 n + 1 π^+} emission from the compound {^{238}U + p} nucleus. These "complicated" reaction channels can explain the quasi-null production rates given by both spallation models (see Figure 21). In addition, INCL4/ABLA results can be questioned if we remember that this model overestimates the formation of π^+ particles.

4.2. Mercury isotopes

As it is shown on Figure 3, $_{80}$Hg elements are located in the UC_3 "spallation valley" and therefore their production is favoured if lead target is employed. On Figures 22 to 25, we observe that the optimal configuration for the production of ^{180}Hg neutron deficient isotopes is the $L \approx$ 27 cm length Pb target irradiated with a 1 GeV proton beam, whereas the best target for production of ^{206}Hg (n-magic) neutron rich isotopes is somewhat shorter ($L \approx$ 18 cm) Pb target irradiated with a 0.5 GeV proton beam.

4.3. Nickel, Gallium, Krypton and Zinc isotopes

As it is shown on Figures 28-29, 32-33, 36-37 and 40-41 for both spallation models, the production of ^{72}Ni (p-magic), ^{81}Ga (n-magic), ^{92}Kr and ^{132}Sn (double-magic) neutron rich fission products is optimal for $L \approx$ 40 cm UC_3 targets irradiated with a 0.5 GeV proton beam. Having in mind the last section 3 remark on the validity domain of CEM2k, we can deduce that this model will overestimate the yields values, whereas the best predictions will be obtained using INCL4/ABLA simulations.
For ^{56}Ni (double-magic), ^{63}Ga, ^{74}Kr and ^{107}Sn isotopes, it is unfortunately impossible to obtain definitive conclusions. Indeed, INCL4/ABLA calculations exhibit quasi-null results and therefore with high statistical errors (less than 10 events are obtained despite of 5×10^6 incident protons), whereas CEM2k simulations lead to higher yield values (see Figures 26-27, 30-31, 34-35 and 38-39). As ^{56}Ni, ^{63}Ga, ^{74}Kr and ^{107}Sn are all neutron deficient fission products (see Figure 3), we can suppose again that the CEM2k results would be overestimated.

[‡] For a specific target, $t \sim V^{\beta}.\exp(-\alpha/T)$, where V and T are the target volume and temperature. α and β are geometry-material dependent parameters.

INCL4/ABLA results are certainly closer to reality, but would require more precise simulations involving prohibitive computation times in order to obtain good statistical errors[§].

4.4. Magnesium and Argon isotopes

On Figures 42 and 43, we observe that the optimal configurations for the formation of ^{20}Mg (n-magic, neutron deficient isotope) are SiC targets with $L \approx 64$ cm. However, the spallation models considered in this study lead to notable differences. In particular, the predictions using CEM2k show unexpected variations with energy of the production rates: τ/E factors increase by a factor 10 between targets irradiated with 0.5 and 2 GeV protons beams. Contrary, the INCL4/ABLA outputs are coherent for Al_2O_3 and SiC targets and could consequently be more reliable, giving the optimal energy of protons ~1 GeV.

For ^{30}Mg (neutron rich isotope), it is even more difficult to conclude. Indeed, the INCL4/ABLA models exhibit quasi-null values and therefore result in high statistical errors, whereas CEM2k is susceptible to overestimate notably the production rates (see Figures 44 and 45). Situation is identical for the production of ^{46}Ar (n-magic, neutron-rich nucleus) from Pb or UC_3 targets (see Figures 46 and 47).

4.5. Neon isotopes

From Figures 48 and 49 we notice again high discrepancies between the model results for ^{25}Ne (neutron rich isotope). First, its production with UC_3 targets is higher for CEM2k than for INCL4/ABLA. As this target opens also fission channel, we could discard CEM2k results remembering that gives non-reliable predictions for fission products far from stability. This conclusion is reinforced by the appearance of unexpected energy dependence in the CEM2k production rates: As in the case of ^{20}Mg, the distributions of τ/E factors with E are rather unexpected. Secondly, production through Al_2O_3 targets requires successive cascade/evaporations of 3 protons from $\{^{27}Al+p\}$ compound nucleus, altogether with a π^+ formation. As INCL4/ABLA model tends to overestimate π^+ production, its predictions are consequently to be considered with caution. Finally, the unique target that seems trustworthy for ^{25}Ne production could be the SiC target, for which CEM2k and INCL4/ABLA simulations give rather close values (optimal configuration: $L \approx 32$-48 cm with a 1 GeV proton beam).

For ^{18}Ne (n-magic, neutron deficient isotope), Figures 50 and 51 show that the best configurations are the $L \approx 48$-64 cm length SiC targets, irradiated with a 1 GeV proton beam. However, as for ^{25}Ne case, notable differences are observed between different model outputs. Concerning ^{17}Ne (2p-halo, neutron-deficient nucleus), it is again difficult to obtain a definitive conclusion. As observed for ^{20}Mg and ^{25}Ne isotopes, the CEM2k energy dependence on the production rates are unusual, which suggests using INCL4/ABLA simulations (see Figures 52 and 53). The optimal configuration would thus be the $L \approx 48$ cm length SiC target irradiated with a 1 GeV proton beam.

4.6. Lithium and Beryllium isotopes

[§] Our calculations have been parallelized on 2 bi-processors AMD Opteron Dual-core 275 at 2.2 GHz each. On these processors, 640 MCNPX simulations cycles of 10^8 incident particles followed by 1280 CINDER evolutions will take several months for completion.

As it is shown on Figures 54 to 57 for both spallation models, the optimal configurations for ^{11}Be (1n-halo, neutron rich nucleus) and ^{12}Be (2n-halo, n-magic, neutron rich nucleus) production are the $L \approx$ 50-75 cm length Al_2O_3 targets, irradiated with a 1 GeV proton beam. Concerning ^{7}Be (neutron deficient nucleus), Figures 58 and 59 reveal that the maximal production rates are obtained using the $L \approx$ 48 cm thick SiC targets irradiated with a 0.5 GeV proton beam, again with a rather good agreement between CEM2k and INCL4/ABLA predictions.

For ^{11}Li (2n-halo, n-magic, neutron rich isotope), the optimal configuration is obtained with the $L \approx$ 75 cm length Al_2O_3 target irradiated with a 1 GeV proton beam (see figures 60 and 61). However, in this case, notable differences appear between the spallation models used. These discrepancies become especially high for the production of ^{9}Li (neutron rich nucleus), with the consequence that a determination of the optimal targets is almost impossible. As it was expected (see Figure 3), the Pb, Ta and UC_3 targets seem however non-optimized to produce these nuclei (also see Figures 62 and 63).

In this section, we have determined for a number of exotic nuclei far from stability which target configuration could be retained or discarded for their optimal production. As expected, our analysis was highly sensitive to the spallation models employed and therefore has required dedicated individual studies. For this reason, in the next section, we will study the isotopic distributions of the 11 elements of interest in order to examine the "exoticism" of radioactive nuclei that EURISOL targets can produce, and also evaluate in more detail the reliability of predictions of the different spallation models within MCNPX.

5. Isotopic distribution of the elements of interest

The exotic nuclei studied in the previous sections will be extracted from EURISOL targets, ionised and post-accelerated in order to produce secondary radioactive beams. The isotopes accessible with these beams will be used to feed physical experiments studying the properties of nuclear structure, creation of super-heavy elements, etc. For all these studies, the full isotopic distribution of the given element will impact directly the quality and duration of the associated experimental programs allowing systematic research from stable to the more and more exotic radioactive isotopes. To enlighten this problematic, we have consequently studied in this last section the isotopic distributions of the 11 elements of interest presented in Section 2 (see Figures 94 to 115).

As for previous sections, calculations are done using MCNPX 2.5.0 simulations, followed by 1 ms CINDER temporal evolutions, for targets of identical radii (18 mm) and masses (2 kg). Both INCL4/ABLA and CEM2k spallation models have been considered in order to estimate the impact of the chosen physics models on our results.

From Figures 99, 101 or 103 we can notice immediately that the isotopic distributions calculated with the CEM2k model for light nuclei exhibit strong oscillations of the productions rates, whose minima and maxima appear for odd and even neutron numbers respectively. This behaviour could be explained by a strong nucleon pairing effect in CEM2k pre-equilibrium/evaporation step. For the INCL4/ABLA model, this effect can be observed on Figure 102 for argon isotopes but vanishes quickly for heavier nuclei.

More generally, INCL4/ABLA distributions remain rather smooth and preserve their quasi-gaussian forms. On the opposite, CEM2k results are less regular and excessively flat. A good illustration of this unexpected (non-physical) behaviour can be observed for magnesium production (see Figure 101), where the production rates remain constant for mass numbers ranging from 20 to 34. This effect remains important for heavier nuclei and confirms thus our remarks (see Part 3) concerning CEM2k overestimation of the neutron rich/neutron deficient reaction product formation. Another illustration of this phenomenon is given on Figures 116 to 123, which summarize the nuclei productions rates for Al_2O_3 and UC_3 targets of 18 mm radii and 2 kg masses.

As the low energetic secondary neutron flux contribution must be taken into account, CINDER temporal evolutions (decay and transmutation in neutron fluxes) are necessary. Consequently, decrease in the isotopic yields (see Figures 114 and 115) for ^{215}Fr, ^{216}Fr and ^{217}Fr is observed. Indeed, the half-lives of these nuclei are 0.09 µs, 0.7 µs and 22 µs respectively and this suppression (see Figures 120-123) is simply due to the natural decay of the corresponding nuclei within 1 ms decay time, being the CINDER evolution time. This behaviour exists also for other isotopes, but it is less pronounced.

		E = 0.5 GeV					*E* = 2 GeV				
Elements	Isotopes	Al_2O_3	Pb	SiC	Ta	UC_3	Al_2O_3	Pb	SiC	Ta	UC_3
Li	^{9}Li	0.86		5.670		7.62	1.55	23.67	2.41		5.04
	^{11}Li	0.05		0		0	0.12	17.03	0.007		0.017
Be	^{7}Be	40.62		30.120		26.67	49.98	16.4	44.71		28.73
	^{11}Be	1.33		0.550		0.45	2.17	5.82	0.71		0.56
	^{12}Be	1.15		0.005		0.005	1	16.14	0.03		0.016
Ne	^{17}Ne	0.001	0	0.003	0	0	0.11	3.98	0.1	0	2.03
	^{18}Ne	0.04	16.66	0.080	0	0	0.33	13.15	0.41	0.02	5.88
	^{25}Ne	0	33.3	0.003	0	11.11	0.01	13.37	0.02	0	17.98
Mg	^{20}Mg	0.001	0	0.003	0	0	0.05	3.65	0.12	14.24	2.04
	^{30}Mg	0	8.34	0	33.29	8.32	0	10.49	0	0	13.2
Ar	^{46}Ar		10.85		18.75	20.12		7.61		0	10.22
Ni	^{56}Ni		3.05		0	0.25		1.16		4.35	0.59
	^{72}Ni		2.05		3.17	6.71		1.54		1.09	2.35
Ga	^{63}Ga		1.03		0	0.16		0.76		1.26	0.35
	^{81}Ga		2.13		0	6.6		0.7		0.63	2.18
Kr	^{74}Kr		0.37		1.2	0.05		0.43		0.001	0.09
	^{92}Kr		1.39		0	6.09		0.84		0.12	5.97
Sn	^{107}Sn		0.51		0	0.03		0.67		1.23	0.19
	^{132}Sn		0.07		0	2.07		0.03		0	2.9
Hg	^{180}Hg		0.001			0		0.01			0.05
	^{206}Hg		0.02			0		0.06			0
Fr	^{205}Fr					0.33					1.29
	^{231}Fr					0					0

Table 3: Proportion in percentage of isotopes ^{A}X produced per element X inside EURISOL direct targets (*R* = 18 mm, *M* = 2 kg, spallation model = CEM2k, the low energetic secondary neutron flux contribution is taken into account, CINDER evolution time = 1 ms). Numbers in grey ▣ are subject to caution due to the lack of statistics (see part 4). Numbers in blue ▣ correspond to the optimal materials as determined in part 4. Remark: The production rates per element X can be retrieved from Figures 11-12.

For both spallation models used in this study, we can observe on Figures 104 to 107 that an increase in the incident proton energy E involves a displacement of the distribution maxima towards lower neutron numbers. This effect is directly linked to the evaporation phase, which results in more excitation energy for higher incident E values and enhances consequently the nucleon emission, mainly neutrons as the light charged particle emission is suppressed due to the Coulomb barrier. For heavy fission products (Kr and Sn), we can notice that the increase in the incident proton energy seems to favour an asymmetric fission (see Figures 108-111). For nuclei situated closer to the targets elements (Hg for molten lead targets and Fr for UC_3 targets), there is no important impact of the protons energy on the isotopic distributions forms, only on their absolute value. Finally, Hg distributions (see Figures 112 and 113) show a pronounced peak for A = 206, due to the double magic shell closure Z = 80 and N = 126.

For {R = 18 mm, M = 2 kg} targets and both spallation models, Tables 3 and 4 give an estimate of the secondary beam isotopic compositions relative to the elemental yield. We believe this is an important quantity, which might help planning systematic studies with different isotopes of the same element.

		E = 0.5 GeV					E = 2 GeV				
Elements	Isotopes	Al_2O_3	Pb	SiC	Ta	UC_3	Al_2O_3	Pb	SiC	Ta	UC_3
Li	^{9}Li	0.63		0.002		0.28	0.83	2.38	0.37	1.18	0.31
	^{11}Li	0.003		0		0	0.004	0	0.003	0.57	0.002
Be	^{7}Be	47.49		70.23		64.36	46.75	32.75	61.1	38.06	51.46
	^{11}Be	0.44		0.08		0.04	0.77	3.64	0.26	7.49	0.06
	^{12}Be	0.09		0.007		0.004	0.16	5.37	0.05	2.2	0.006
Ne	^{17}Ne	0.002	0	0.006	0	0	0.01	0	0.02	0	0
	^{18}Ne	1.27	0	1.55	0	0	2.45	0	2.99	0	0
	^{25}Ne	0.01	0	0.005	0	0	0.03	2.94	0.007	1.05	5.32
Mg	^{20}Mg	0.05	0	0.13	0	0	0.1	0	0.34	0	0
	^{30}Mg	0	0	0	0	0	0	1.39	0	0.87	3.28
Ar	^{46}Ar		0		0	2.31		0.17		0	0.44
Ni	^{56}Ni		0.04		0	0		0.01		0.06	0
	^{72}Ni		0.23		0	1.36		0.04		0.03	0.53
Ga	^{63}Ga		0		0	0		0.01		0.05	0.002
	^{81}Ga		0		0	0.84		0		0	0.43
Kr	^{74}Kr		0		0	0		0.006		0.07	0.001
	^{92}Kr		0.03		0	7.31		0.03		0	6.77
Sn	^{107}Sn		0		0	0		0.11		0.57	0.007
	^{132}Sn		0		0	1.08		0		0	1.46
Hg	^{180}Hg		0.003			0		0.02			0.11
	^{206}Hg		0.53			0		0.96			0
Fr	^{205}Fr					0					0.08
	^{231}Fr					0.14					0.22

Table 4: Proportion in percentage of isotopes ^{A}X produced per element X inside EURISOL direct targets (R = 18 mm, M = 2 kg, spallation model = INCL4/ABLA, the low energetic secondary neutron flux contribution is taken into account, CINDER evolution time = 1 ms). Numbers in grey ▣ are subject to caution due to the lack of statistics (see part 4). Numbers in blue ▣ correspond to the optimal materials as determined in part 4. Remark: The production rates per element X can be retrieved on Figures 3-4 and 11-12.

6. Conclusion

A methodology has been developed to optimize the in-target production of radioactive isotopes using direct EURISOL targets. This method is based on simulations, whose results are progressively used to feed an increasing database. In particular, we have obtained the expected in-target nuclei production rates in terms of their charge Z and mass A distributions. We have also tried to optimize the in-target yields for 11 elements of interest (Li, Be, Ne, Mg, Ar, Ni, Ga, Kr, Hg and Sn) and for 23 of their isotopes. We have finally studied their isotopic distributions to estimate the RIB isotopic compositions. The results presented in this report will be coupled with their corresponding ion extraction efficiencies (in collaboration between Tasks 3 and 11) in order to obtain the secondary exotic beam intensities. Our future work will concentrate on in-target yields prediction and optimization for double-stage targets, where the primary beam power will exceed strongly the 100 kW level.

More detail information, tabulated data and analysis programs are available for interested users within the EURISOL DS project. For any requests please e-mail to: sebastien.chabod@lpsc.in2p3.fr, jean-christophe.david@cea.fr, or danas.ridikas@cea.fr.

7. Acknowledgement

We acknowledge the financial support of the EC under the FP6 "Research Infrastructure Action – Structuring the European Research Area" EURISOL DS Project; Contract No. 515768 RIDS; www.eurisol.org. The EC is not liable for any use that may be made of the information contained herein.

Finally, we wish to thank T. Stora for discussions and useful suggestions during this work. We also acknowledge the help of O. Bringer in the programming of the routine engine.

8. References

[1] EURISOL design study, available at: www.eurisol.org/site01/index.php

[2] T. Stora *et al.*, *The EURISOL facility: feasibility study for the 100 kW direct targets*, internal report for EURISOL-DS Task 3, available at: www.eurisol.org/site01/doc_details.php?EURpub=1&dID=374&tID=7

[3] T. Stora, *Baseline parameters 05/27/2005 Eurisol-DS task #3,* available at: www.eurisol.org/site01/doc_details.php?EURpub=1&dID=72&tID=7

[4] N. Thiollière *et al.*, *Optimization of ^{6}He production using W or Ta converter surrounded by BeO target assembly,* CEA Saclay internal report DAPNIA-06-274 for EURISOL-DS Task 3 (2006).

[5] MCNPX user's manual, version 2.5.0, LA-CP-05-0369 (Denise B. Pelowitz, editor) (2005)

[6] J.-C. David *et al.*, *Benchmark calculations on residue production within the EURISOL DS project, Part I: thin targets*, CEA Saclay internal report DAPNIA-07-04 for EURISOL-DS Task 11 (2007), available at: www.eurisol.org/site01/doc_details.php?EURpub=1&dID=781&tID=15

[7] J.-C. David *et al.*, *Benchmark calculations on residue production within the EURISOL DS project, Part II: thick targets*, CEA Saclay internal report DAPNIA-07-59 for EURISOL-DS Task 11 (2007), available at: www.eurisol.org/site01/doc_details.php?EURpub=1&dID=735&tID=15
[8] A. Boudard *et al.*, Phys. Rev. C 66 (2002) 044615
[9] A. R. Junghans *et al.*, Nucl. Phys. A 629 (1998) 655; J. Benlliure *et al.*, Nuclear Physics A 628 (1998) 458-478
[10] S. G. Mashnik and A. J. Sierk, *Recent developments of the cascade-exciton model of nuclear reactions*, LANL report LA-UR-01-5390 (2001)
[11] F. Atchison, "Spallation and Fission in Heavy Metal Nuclei under Medium Energy Proton Bombardment," in *Targets for Neutron Beam Spallation Sources*, Jul-Conf-34, Kernforschungsanlage Julich GmbH (January 1980).
[12] W.B. Wilson and T.R. England, *A manual for CINDER'90 version C00D and associated codes and data*, LA-UR-00-Draft (2001)
[13] The EURISOL report, *Feasibility study for the EURopean Isotope-Separation-On-Line radioactive beam facility (appendix C)* (2003), available at: www.ganil.fr/eurisol/Final_Report.html
[14] R.D. Page *et al.*, *Selection of key experiments with the associated instrumentation,* available at: www.eurisol.org/site01/doc_details.php?EURpub=1&dID=725&tID=14
[15] E. Le Gentil *et al.*, Phys. Rev. Lett. 100**,** 022701 (2008)
[16] S. Lukic *et al.*, Systematic comparison of ISOLDE-SC yields with calculated in-target production rates, NIM A565 (2006) 784-800
[17] Internal report CERN-EP/2002-048
[18] W. Pohorecki *et al.*, NIM A 5362 (2006) 750-754

APPENDIX A

Input files for *routine*

- *list_type.dat*: this file must contain the name of the first level repertories of the tree (EURISOL target classification: direct or two-staged) (see figure 2),
- *list_mod.dat*: this file must contain the name of the second level repertories (spallation models for MCNPX),
- *list_mat.dat*: this file must contain the name of the third level repertories (target materials) (see table 1).

Arguments for *routine*

To ensure an easy navigation in the data tree, the *routine* engine takes different arguments:

Argument 1: EURISOL target type (see *list_type.dat*).
arg. 1 = Direct → search is for direct targets.
arg. 1 = Fission → two-staged targets.
arg. 1 = all → search is for both types.

Argument 2: MCNPX spallation model (see *list_mod.dat*).
arg. 2 = CEM2k → search is for production rates calculated with CEM2k model.
arg. 2 = INCL4ABLA→ calculations with INCL4/ABLA model.
arg. 2 = all → search is for both models,

Argument 3: target material (see *list_mat.dat*).
arg. 3 = Al2O3 → search is for alumina targets.
arg. 3 = SiC → silicon carbide targets.
arg. 3 = Pb_molten → molten lead targets.
arg. 3 = Ta → tantalum targets.
arg. 3 = UCx → uranium carbide targets.
arg. 3 = all → search is for all different types.

Argument 4: target radius (see table 1).
arg. 4 = val_R → search is for targets of val_R radius.
arg. 4 = 0 → search is for all radii.

Argument 5: target length (see table 1).
arg. 5 = val_L → search is for targets of val_L lengths.
arg. 5 = 0 → search is for all lengths.

Argument 6: proton energies (see table 1).
arg. 6 = val_E → search is for proton beams of val_E energy.
arg. 6 = 0 → search is for all energies.

Arguments 7 and *8* are particular. Indeed, the program *routine* performs different tasks according to their values. The results displayed are:

- a production rate for a specific nucleus of charge number Z and mass number A:
  arg. 7 = Z (>0).

arg. 8 = A (>0).

- all the production rates for the whole nuclei produced in the target:
  arg. 7 = 0.
  arg. 8 = 0.
- the distribution in atomic number A for nuclei of specific charge Z:
  arg. 7 = Z (>0).
  arg. 8 = 0.
- the distribution in charge number Z for nuclei of specific mass A:
  arg. 7 = 0
  arg. 8 = A (>0)
- the distribution in charge number Z for all nuclei:
  arg. 7 = -1
  arg. 8 = 0
- the distribution in atomic number A for all nuclei:
  arg. 7 = 0
  arg. 8 = -1

Argument 9: Is the low energetic secondary neutron flux taken into account in CINDER calculations?
arg. 9 = 1 → no.
arg. 9 = 2 → yes.
arg. 9 = 0 → search is for both.

Argument 10: evolution time for CINDER'90 calculations.
arg. 10 = 1 → 1 ms.
arg. 10 = 2 → 3 months.
arg. 10 = 0 → search is for both.

Argument 11: name of the output file.

Examples of analysis

./routine Direct CEM SiC 18 all all 4 0 2 1 Be_output
This command line writes in an output file called "Be_output" the atomic mass distribution of the production rates for beryllium nuclei, calculated using MCNPX CEM2k spallation code, for silicon carbide direct targets of radius 18 mm, 32/48/64/80 cm lengths, 0.5/1.0/1.5/2.0 GeV protons beams, after a 1 ms CINDER evolution in the low energetic secondary neutron flux.

./routine Direct INCL4ABLA SiC 18 32 2 -1 0 1 1 dZ_distribution
This command line writes in a file called "dZ_distribution" the charge number distribution of the production rates for the whole nuclei created inside a SiC target of radius 18 mm, length 32 cm, irradiated with a 2 GeV protons beam. Calculations are done using MCNPX INCL4/ABLA spallation model, followed by a 1 ms CINDER evolution done in a neutron flux arbitrarily set to 0.

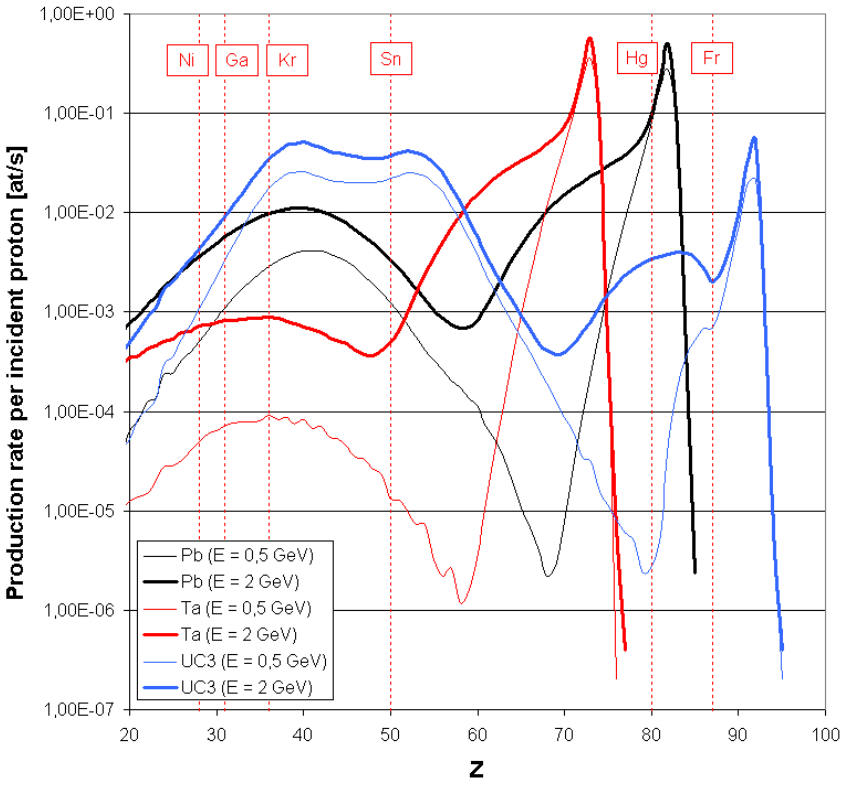

Figure 3: Charge number distribution of the production rates for the secondary nuclei produced inside Pb, Ta and UC_3 targets (R = 18 mm, $M = \pi.\rho.R^2.L$ = 2 kg, spallation model = INCL4/ABLA, the low energetic secondary neutron flux is taken into account, CINDER evolution time = 1 ms)

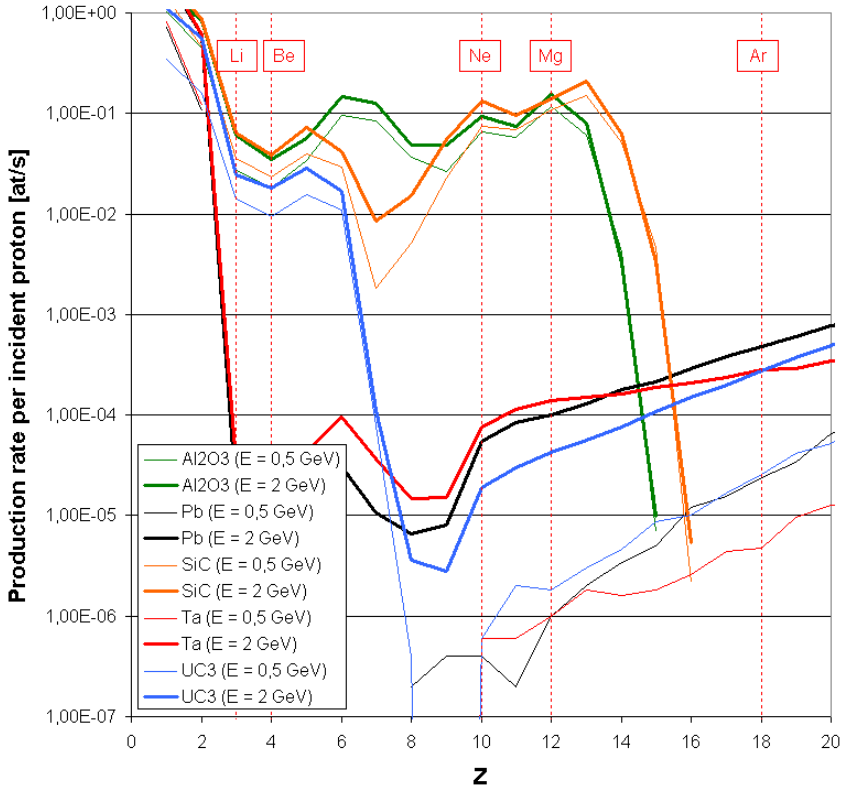

Figure 4: Charge number distribution of the production rates for the secondary nuclei produced inside Al_2O_3, Pb, Sic, Ta and UC_3 targets (R = 18 mm, M = 2 kg, model = INCL4/ABLA, the low energetic secondary neutron flux is taken into account, CINDER evolution time = 1 ms)

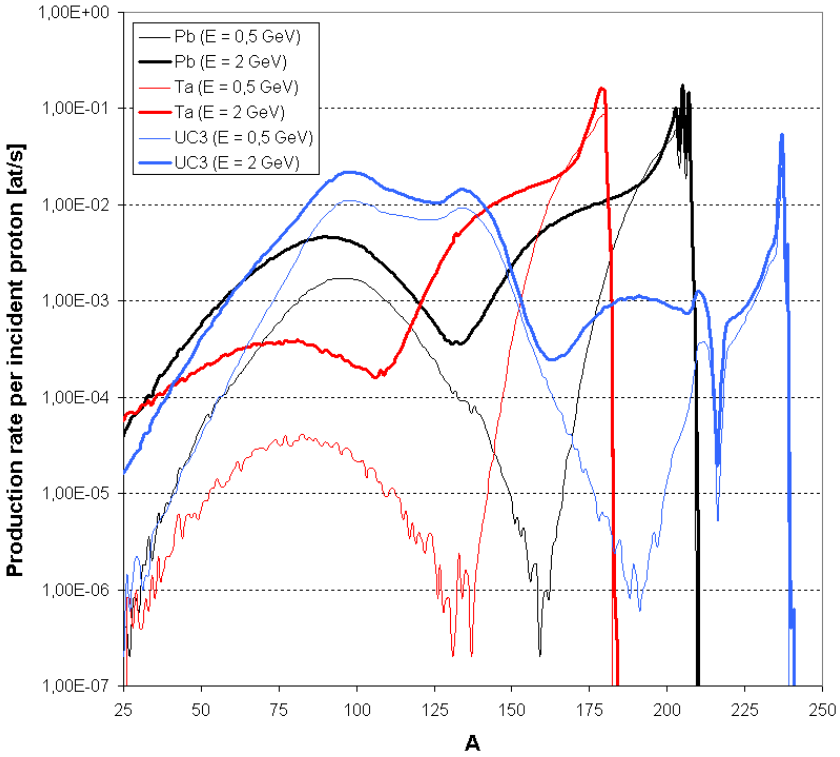

Figure 5: Mass number distribution of the production rates for the secondary nuclei produced inside Pb, Ta and UC_3 targets (R = 18 mm, M = 2 kg, model = INCL4/ABLA, the low energetic secondary neutron flux is taken into account, CINDER evolution time = 1 ms)

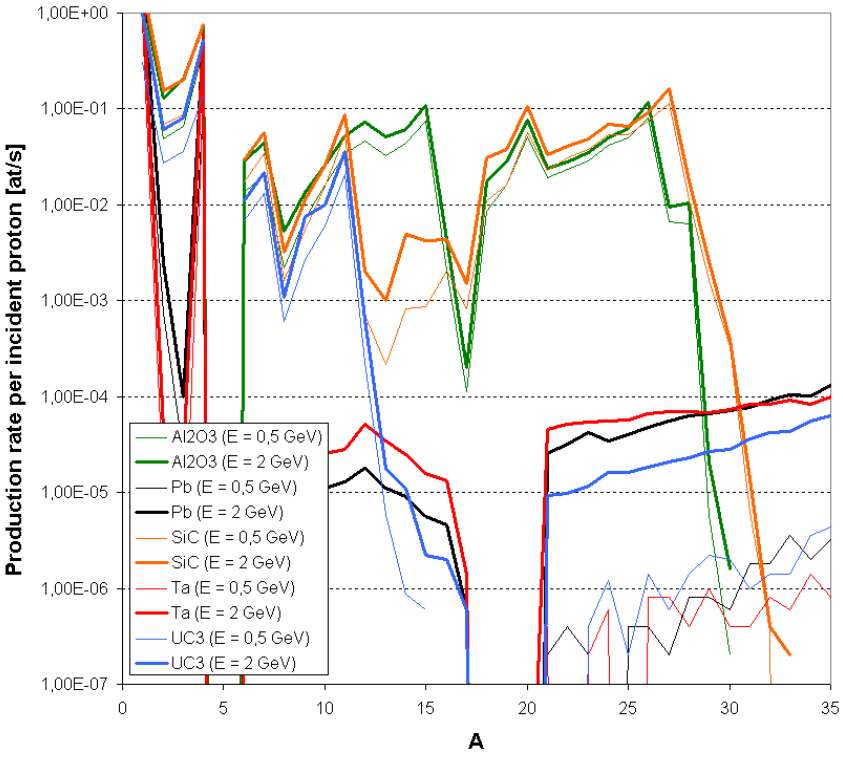

Figure 6: Mass number distribution of the production rates for the secondary nuclei produced inside Al_2O_3, Pb, SiC, Ta and UC_3 targets (R = 18 mm, M = 2 kg, model = INCL4/ABLA, the low energetic secondary neutron flux is taken into account, CINDER evolution time = 1 ms)

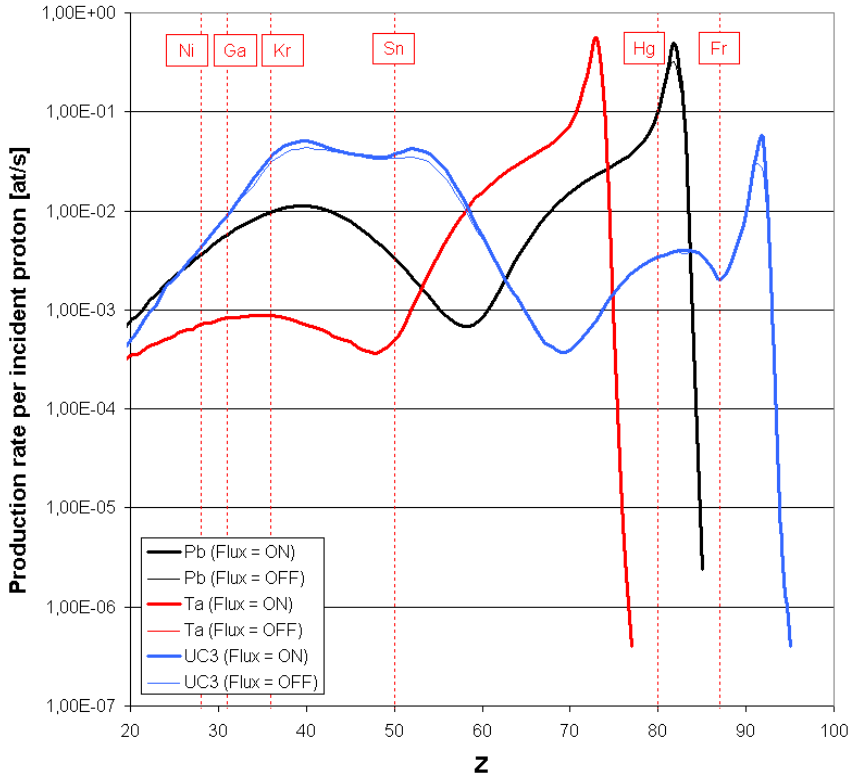

Figure 7: Impact of the low energetic secondary neutron flux on the charge number distribution of the production rates inside Pb, Ta and UC_3 targets (R = 18 mm, M = 2 kg, model = INCL4/ABLA, E = 2 GeV, CINDER evolution time = 1 ms).

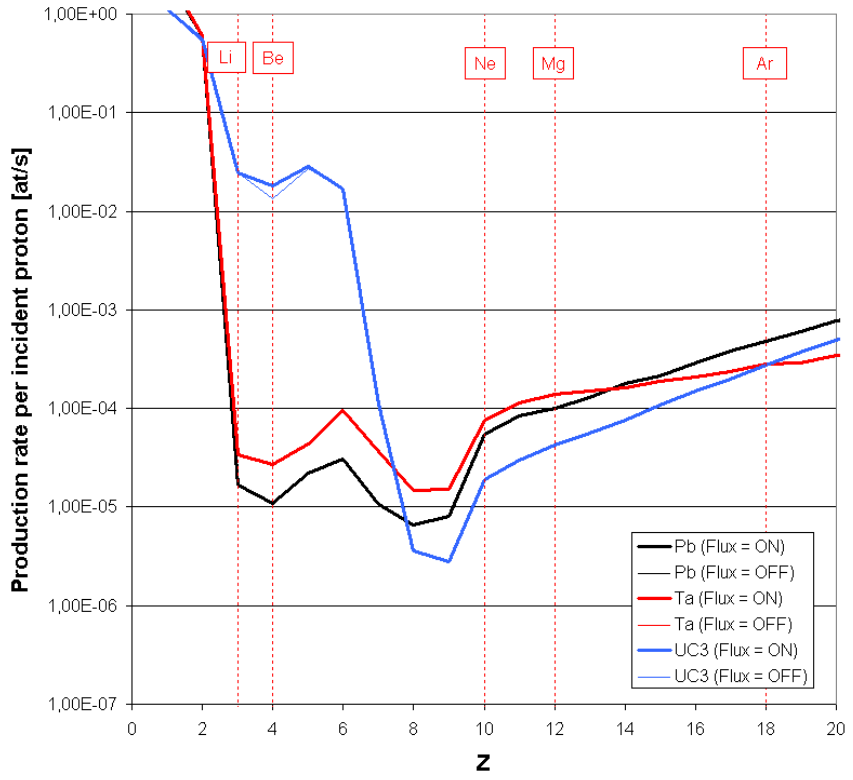

Figure 8: Impact of the low energetic secondary neutron flux on the charge number distribution of the production rates inside Pb, Ta and UC_3 targets (R = 18 mm, M = 2 kg, model = INCL4/ABLA, E = 2 GeV, CINDER evolution time = 1 ms).

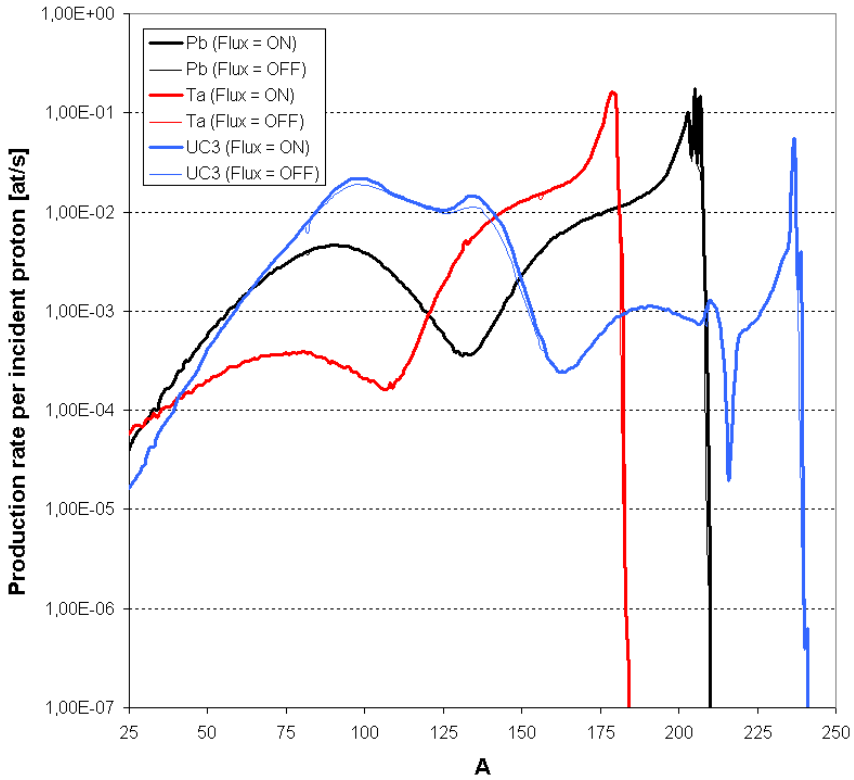

Figure 9: Impact of the low energetic secondary neutron flux on the mass number distribution of the production rates inside Pb, Ta and UC_3 targets (R = 18 mm, M = 2 kg, model = INCL4/ABLA, E = 2 GeV, CINDER evolution time = 1 ms).

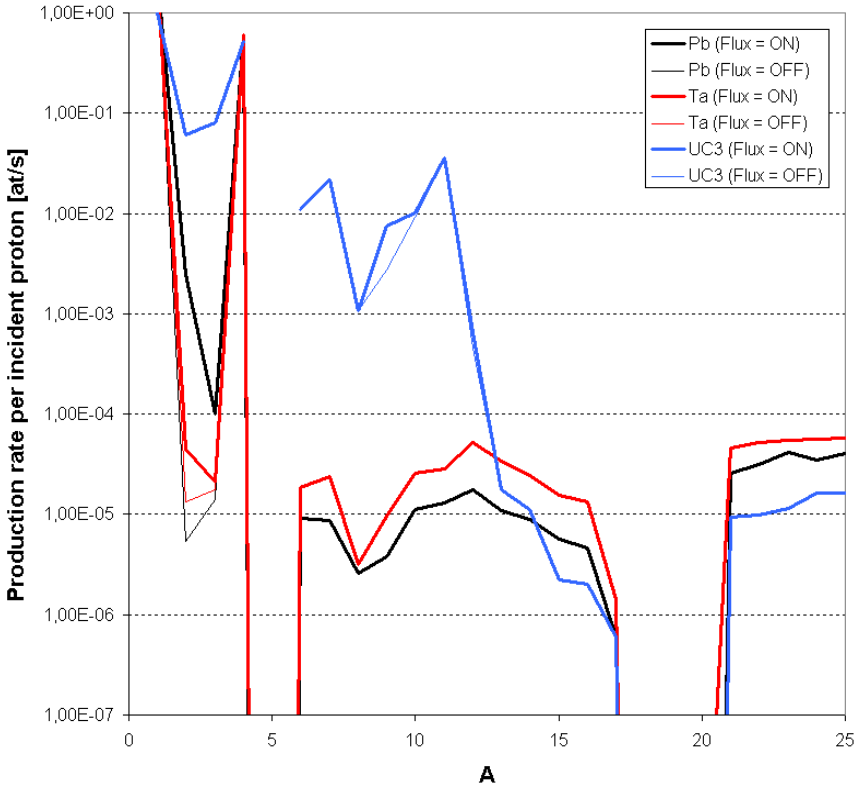

Figure 10: Impact of the low energetic secondary neutron flux on the mass number distribution of the production rates inside Pb, Ta and UC_3 targets (R = 18 mm, M = 2 kg, model = INCL4/ABLA, E = 2 GeV, CINDER evolution time = 1 ms).

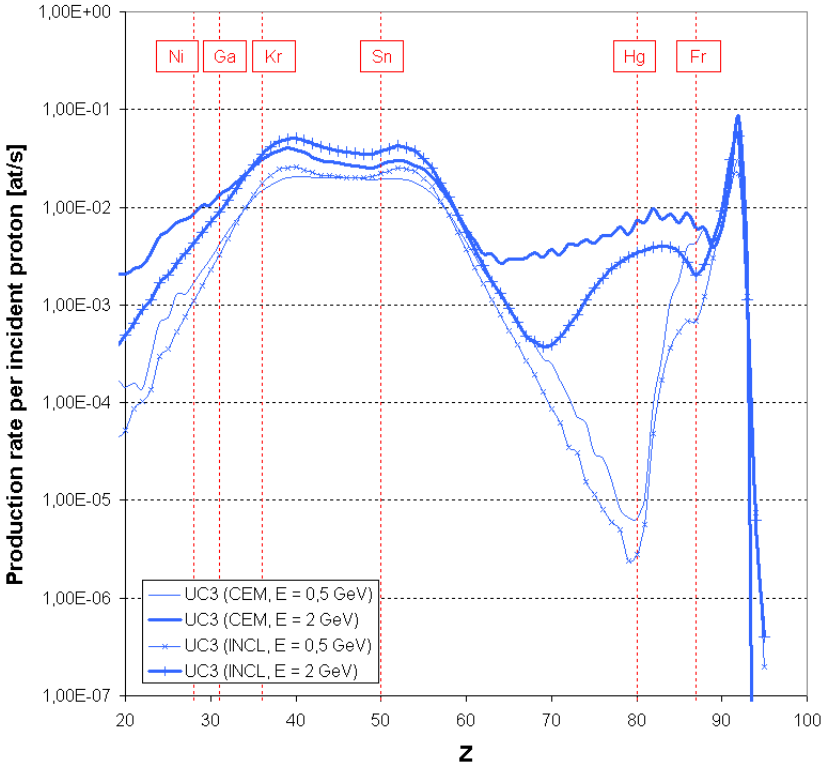

Figure 11: INCL4/ABLA and CEM2k results for the charge number distribution of the production rates for the secondary nuclei produced inside UC_3 targets (R = 18 mm, M = 2 kg, the low energetic secondary neutron flux is taken into account, CINDER evolution time = 1 ms)

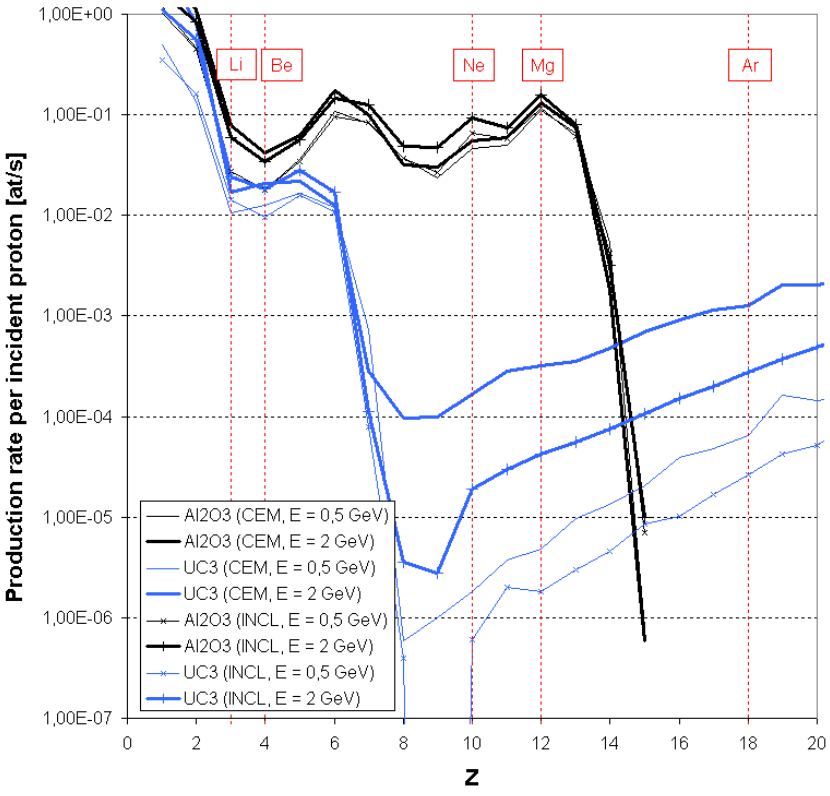

Figure 12: INCL4/ABLA and CEM2k results for the charge number distribution of the production rates for the secondary nuclei produced inside Al_2O_3 and UC_3 targets (R = 18 mm, M = 2 kg, the low energetic secondary neutron flux is taken into account, CINDER evolution time = 1 ms)

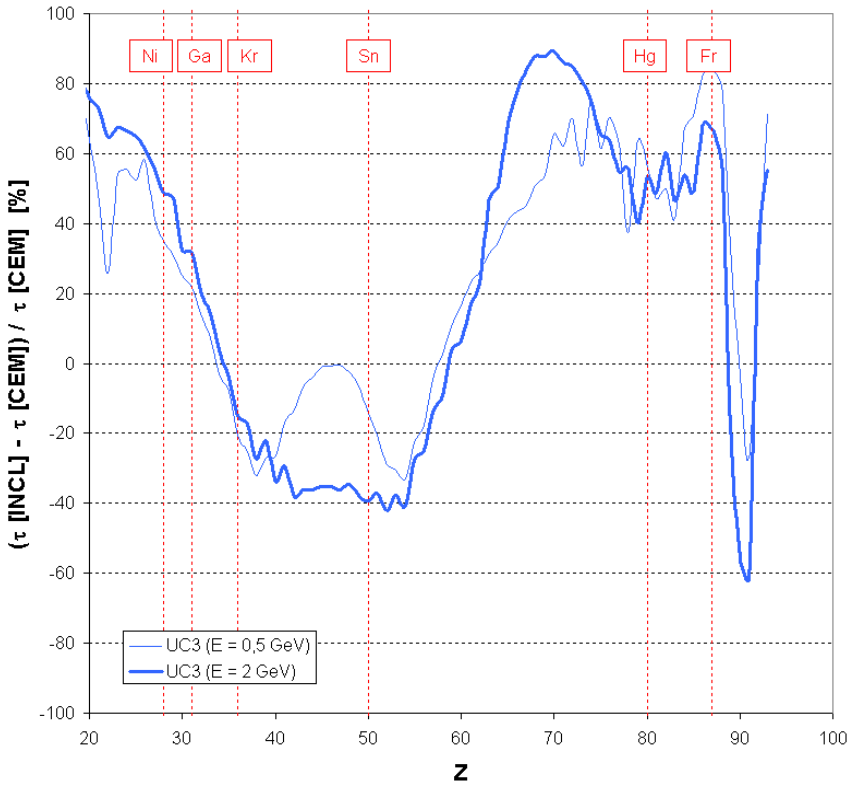

Figure 13: Charge number distribution of the relative ratios between INCL4/ABLA and CEM2k production rates τ results (target = UC_3, R = 18 mm, M = 2 kg, the low energetic secondary neutron flux is taken into account, CINDER evolution time = 1 ms).

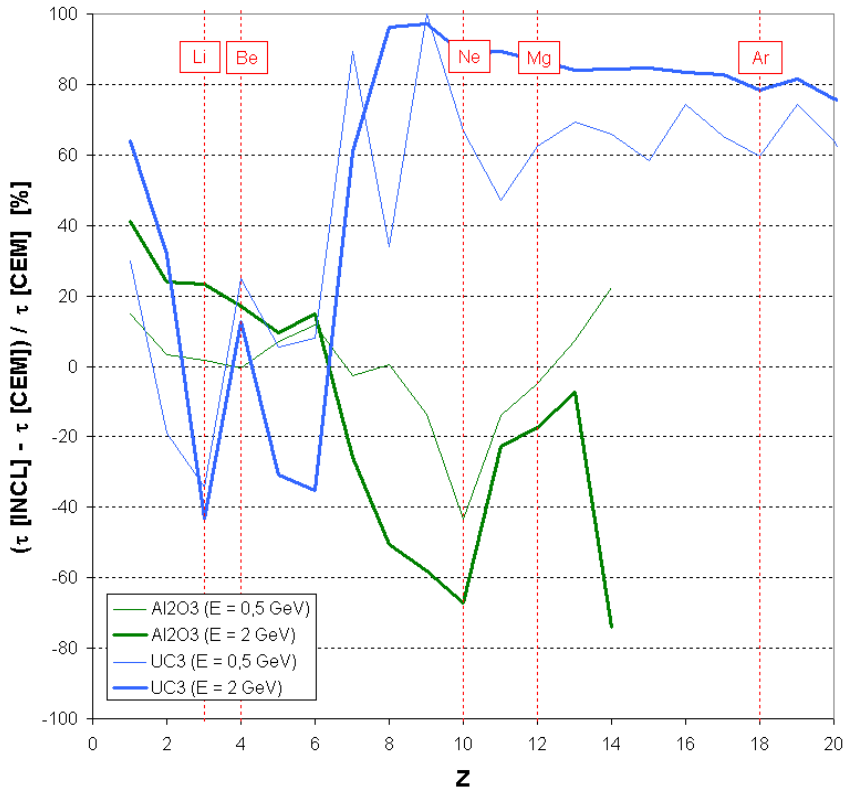

Figure 14: Charge number distribution of the relative ratios between INCL4/ABLA and CEM2k production rates τ results (target = Al_2O_3 and UC_3, R = 18 mm, M = 2 kg, the low energetic secondary neutron flux is taken into account, CINDER evolution time = 1 ms).

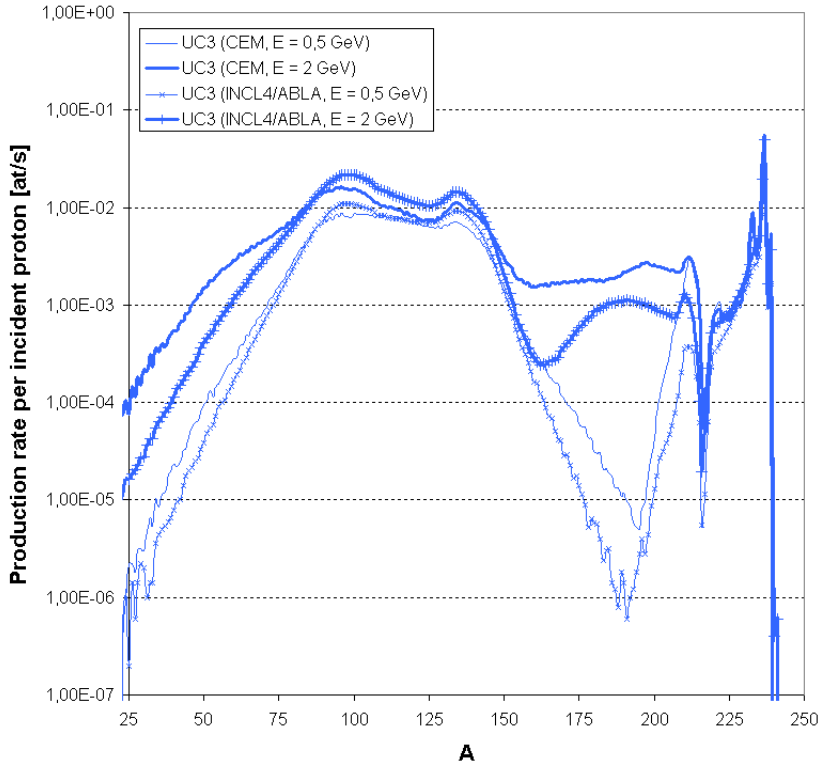

Figure 15: INCL4/ABLA and CEM2k results for the mass number distribution of the production rates for the secondary nuclei produced inside UC_3 targets (R = 18 mm, M = 2 kg, the low energetic secondary neutron flux is taken into account, CINDER evolution time = 1 ms)

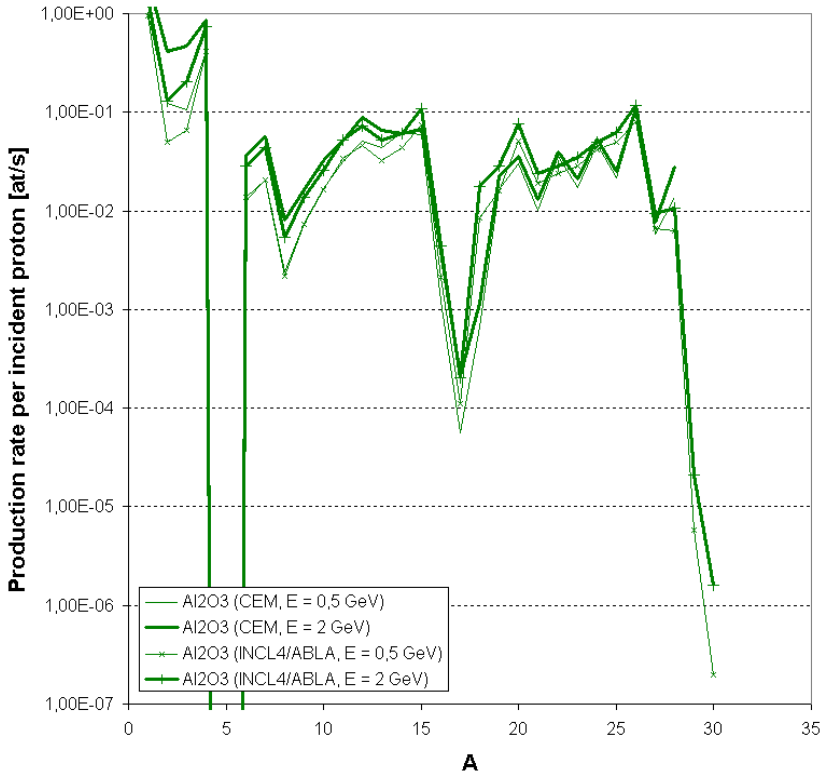

Figure 16: INCL4/ABLA and CEM2k results for the mass number distribution of the production rates for the secondary nuclei produced inside Al_2O_3 targets (R = 18 mm, M = 2 kg, the low energetic secondary neutron flux is taken into account, CINDER evolution time = 1 ms)

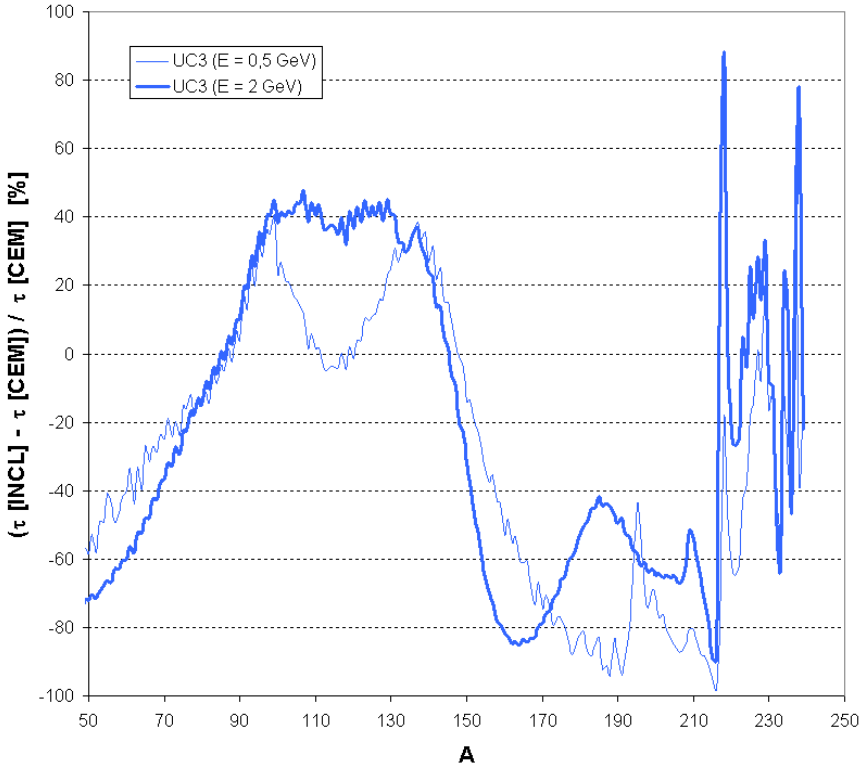

Figure 17: Mass number distribution of the relative ratios between INCL4/ABLA and CEM2k production rates τ results (target = UC_3, R = 18 mm, M = 2 kg, the low energetic secondary neutron flux is taken into account, CINDER evolution time = 1 ms).

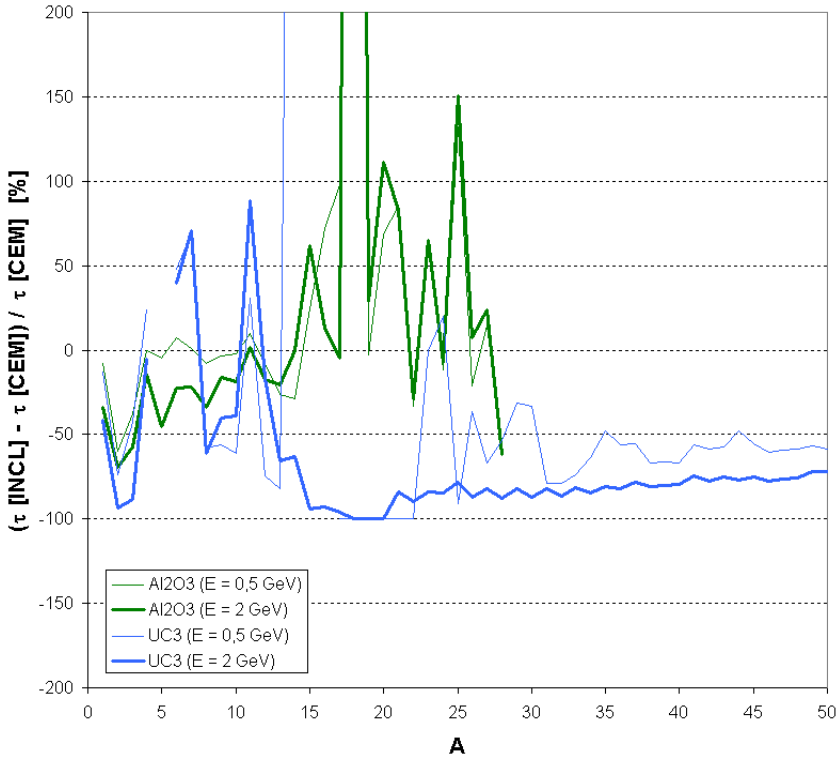

Figure 18: Mass number distribution of the relative ratios between INCL4/ABLA and CEM2k production rates τ results (targets = Al_2O_3 and UC_3, R = 18 mm, M = 2 kg, the low energetic secondary neutron flux is taken into account, CINDER evolution time = 1 ms).

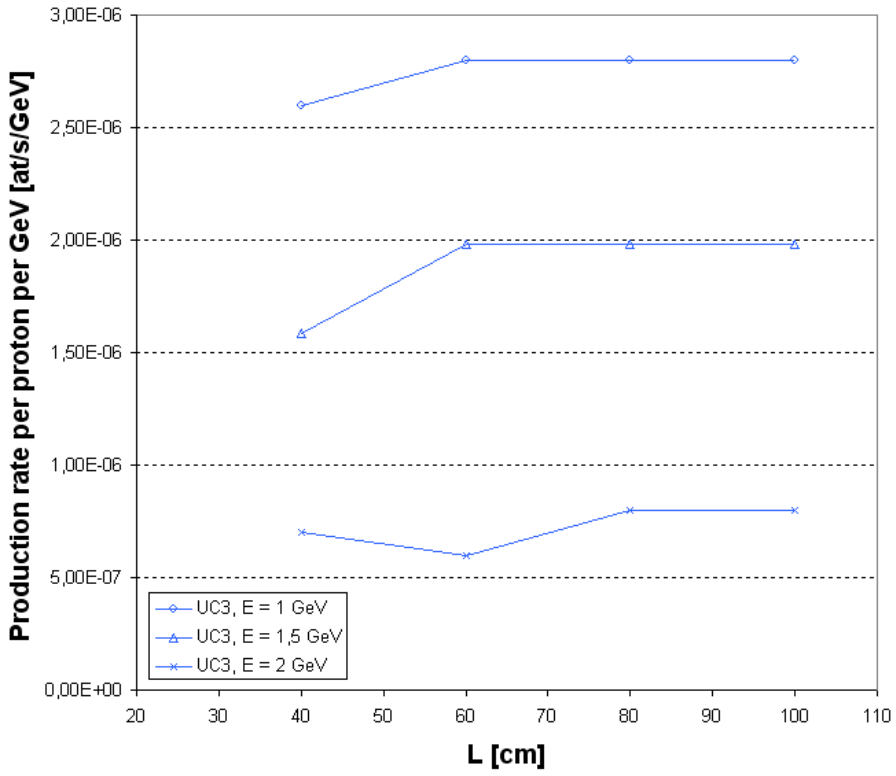

Figure 19: ^{205}Fr production rate per incident proton per GeV (R = 18 mm, spallation model = INCL4/ABLA, the low energetic secondary neutron flux contribution is taken into account, CINDER evolution time = 1 ms).

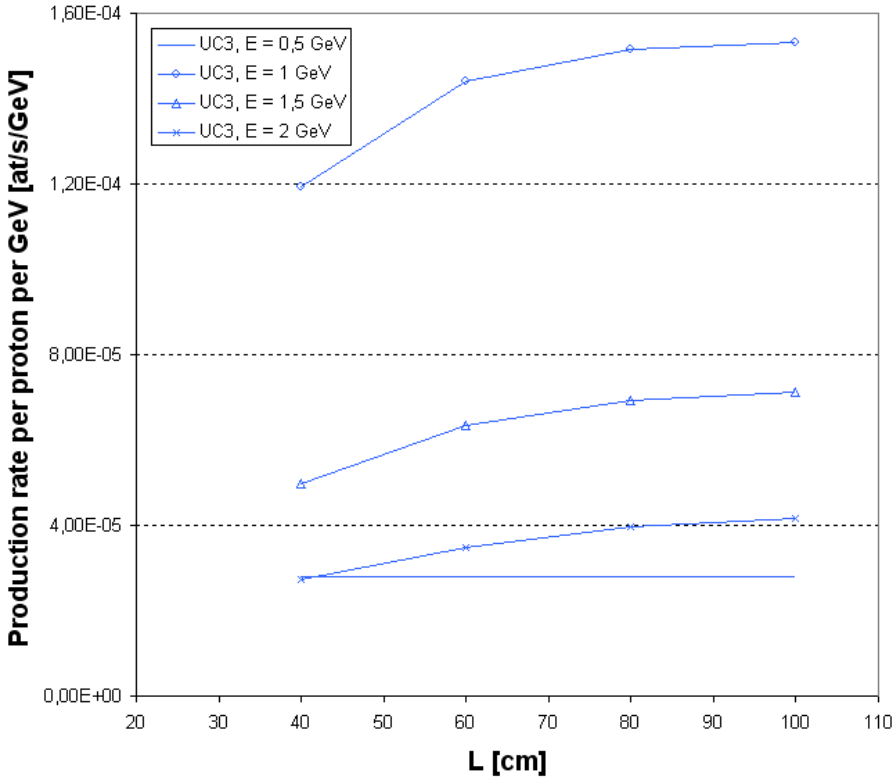

Figure 20: ^{205}Fr production rate per incident proton per GeV (R = 18 mm, spallation model = CEM2k, the low energetic secondary neutron flux contribution is taken into account, CINDER evolution time = 1 ms).

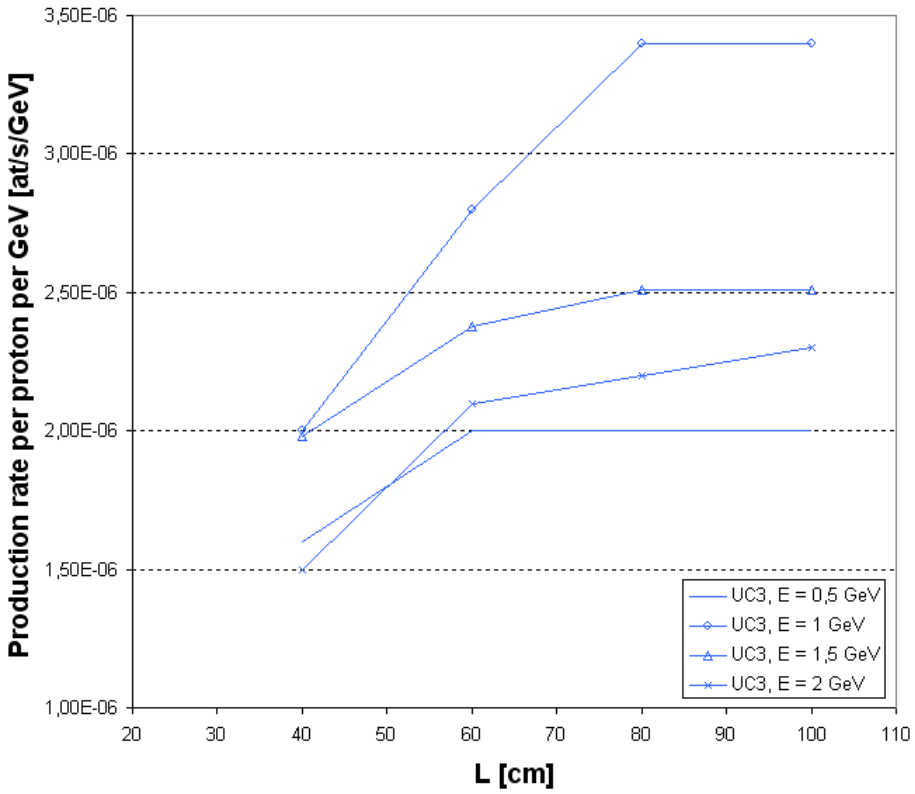

Figure 21: ^{231}Fr production rate per incident proton per GeV (R = 18 mm, spallation model = INCL4/ABLA, the low energetic secondary neutron flux contribution is taken into account, CINDER evolution time = 1 ms).

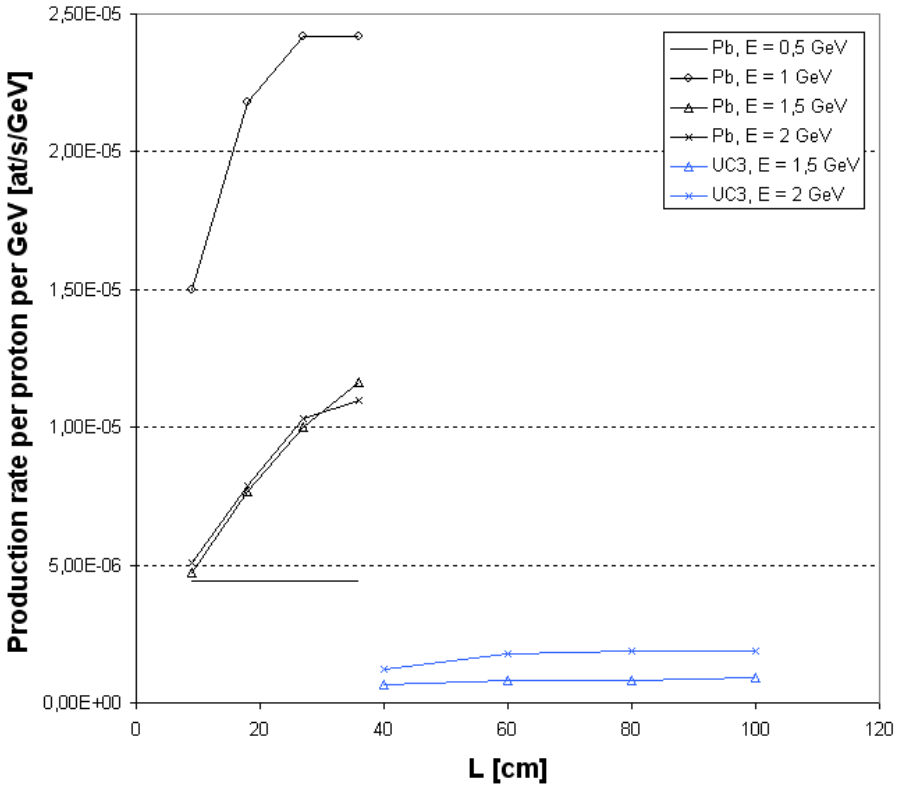

Figure 22: ^{180}Hg production rate per incident proton per GeV (R = 18 mm, spallation model = INCL4/ABLA, the low energetic secondary neutron flux contribution is taken into account, CINDER evolution time = 1 ms).

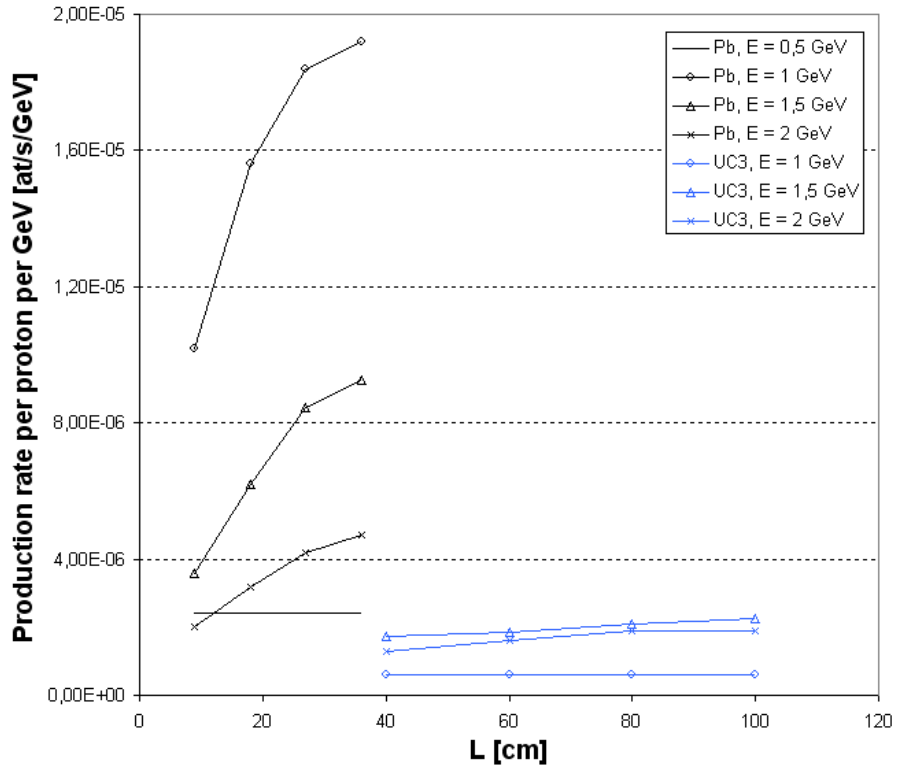

Figure 23: ^{180}Hg production rate per incident proton per GeV (R = 18 mm, spallation model = CEM2k, the low energetic secondary neutron flux contribution is taken into account, CINDER evolution time = 1 ms).

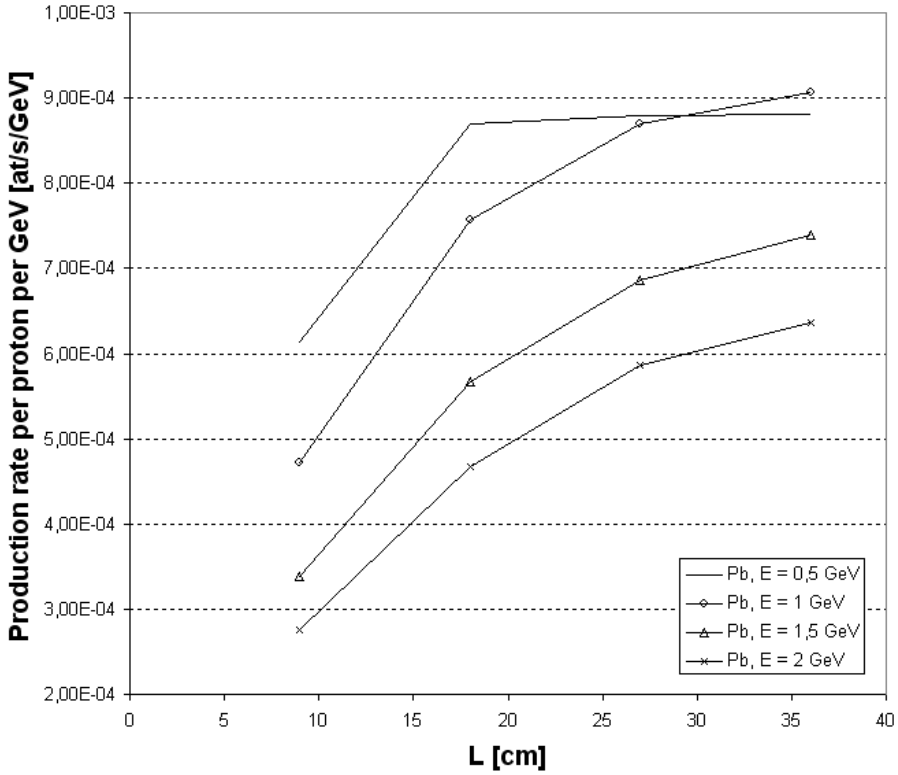

Figure 24: ^{206}Hg production rate per incident proton per GeV (R = 18 mm, spallation model = INCL4/ABLA, the low energetic secondary neutron flux contribution is taken into account, CINDER evolution time = 1 ms).

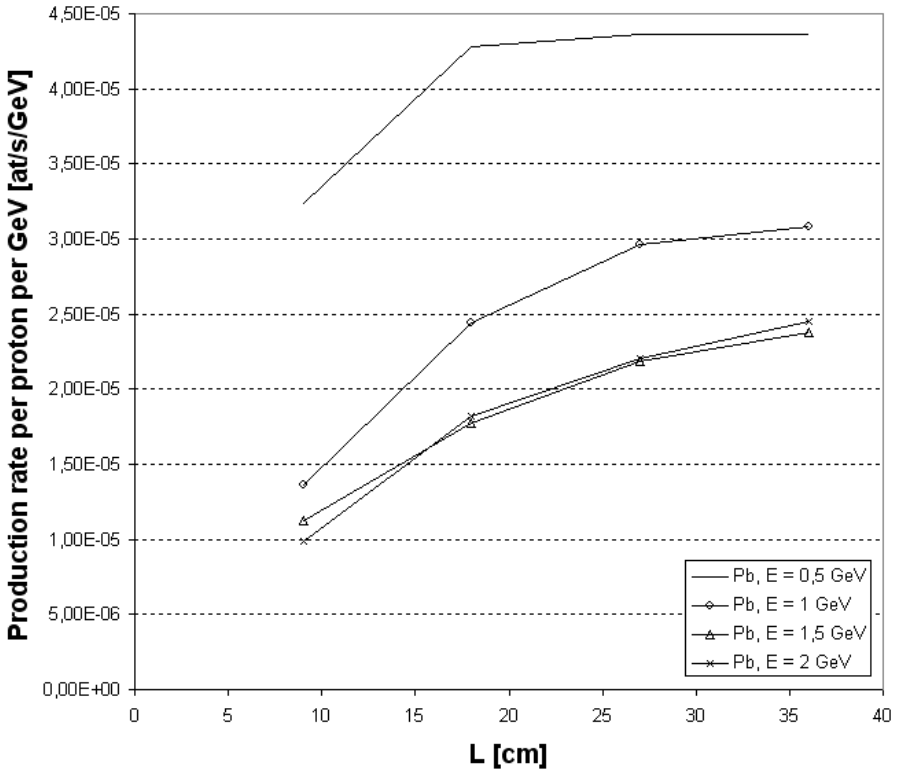

Figure 25: ^{206}Hg production rate per incident proton per GeV (R = 18 mm, spallation model = CEM2k, the low energetic secondary neutron flux contribution is taken into account, CINDER evolution time = 1 ms).

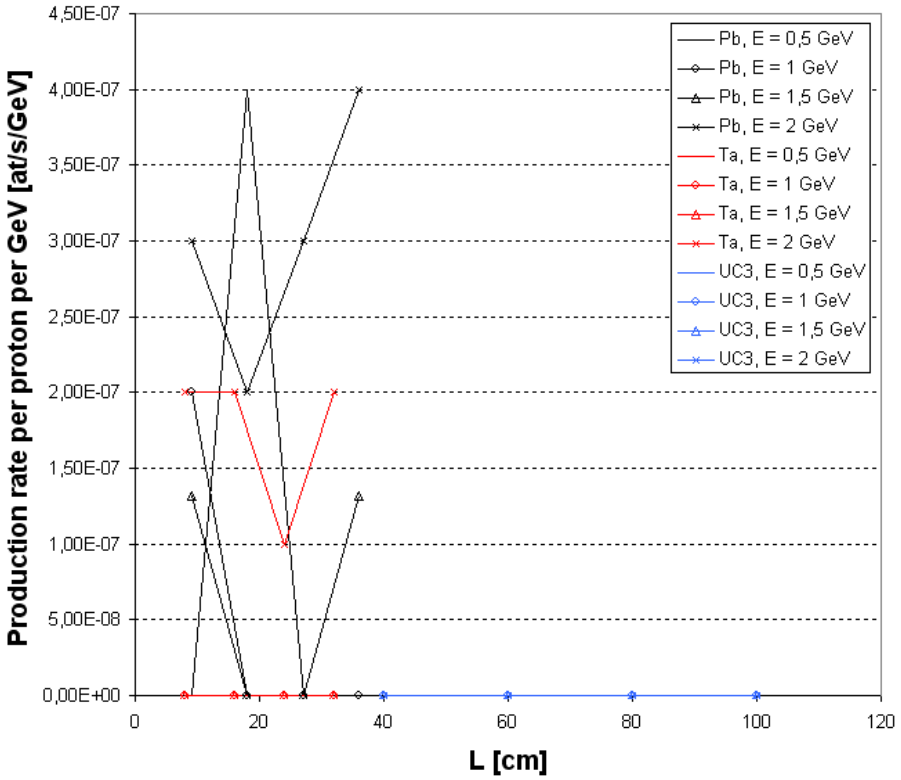

Figure 26: ^{56}Ni production rate per incident proton per GeV (R = 18 mm, spallation model = INCL4/ABLA, the low energetic secondary neutron flux contribution is taken into account, CINDER evolution time = 1 ms).

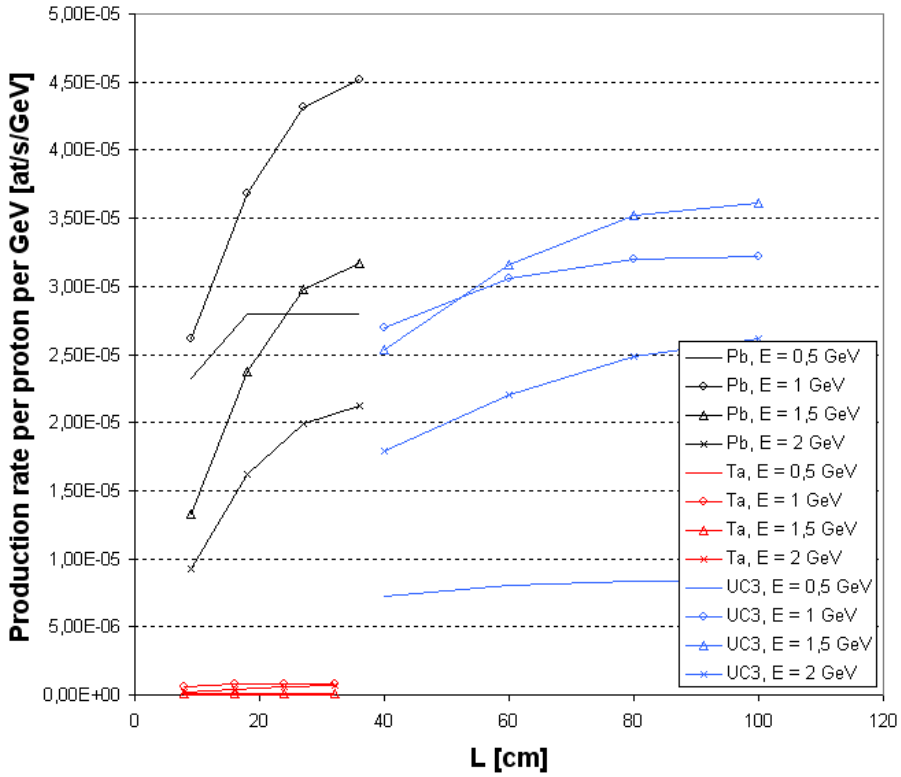

Figure 27: ^{56}Ni production rate per incident proton per GeV (R = 18 mm, spallation model = CEM2k, the low energetic secondary neutron flux contribution is taken into account, CINDER evolution time = 1 ms).

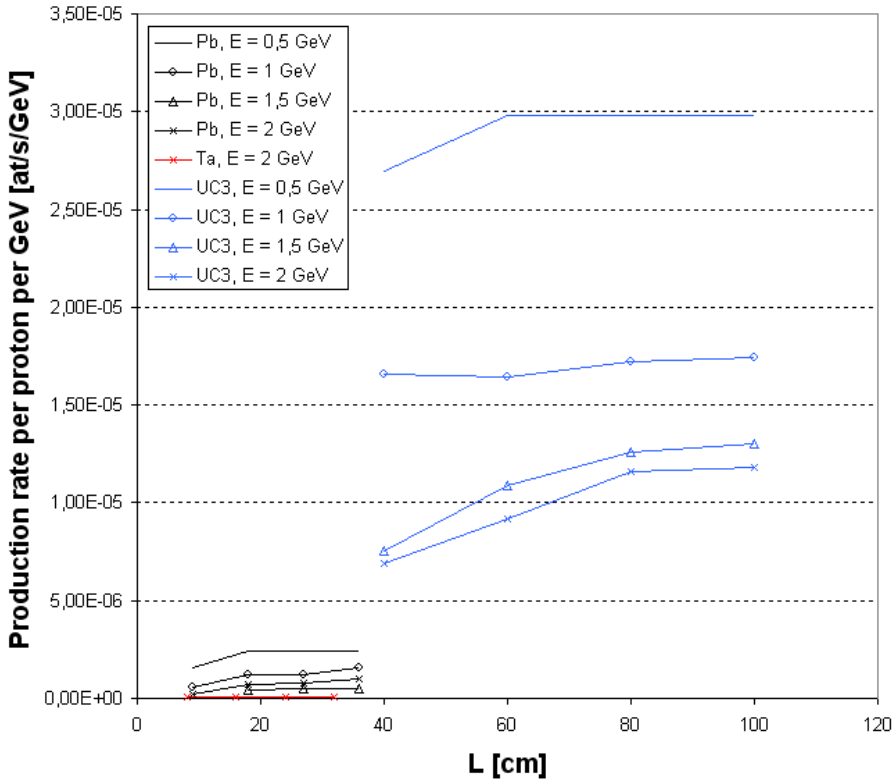

Figure 28: ^{72}Ni production rate per incident proton per GeV (R = 18 mm, spallation model = INCL4/ABLA, the low energetic secondary neutron flux contribution is taken into account, CINDER evolution time = 1 ms).

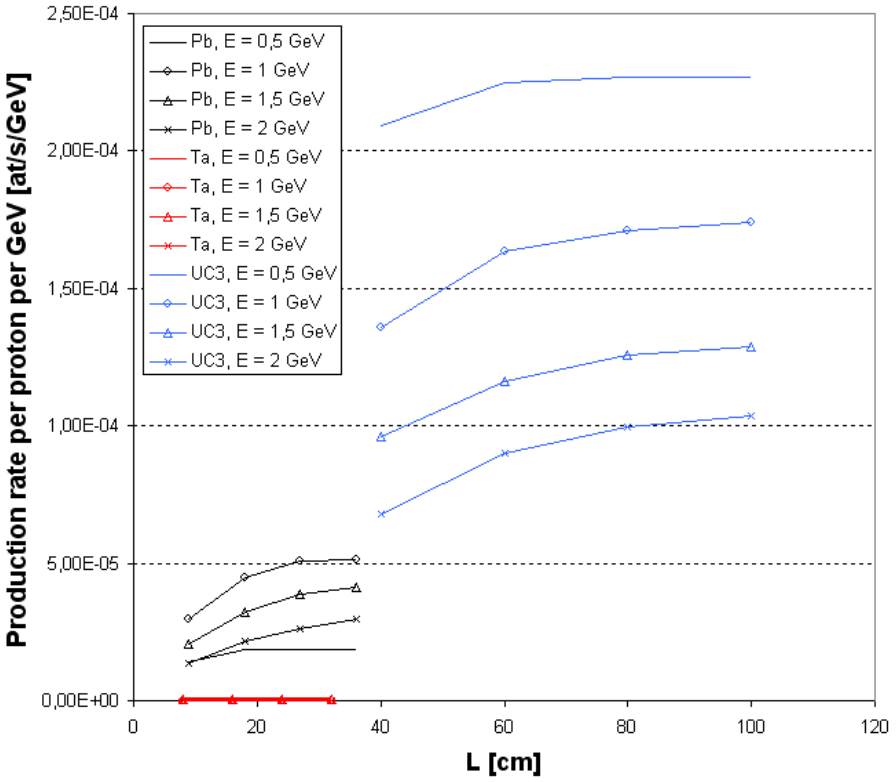

Figure 29: ^{72}Ni production rate per incident proton per GeV (R = 18 mm, spallation model = CEM2k, the low energetic secondary neutron flux contribution is taken into account, CINDER evolution time = 1 ms).

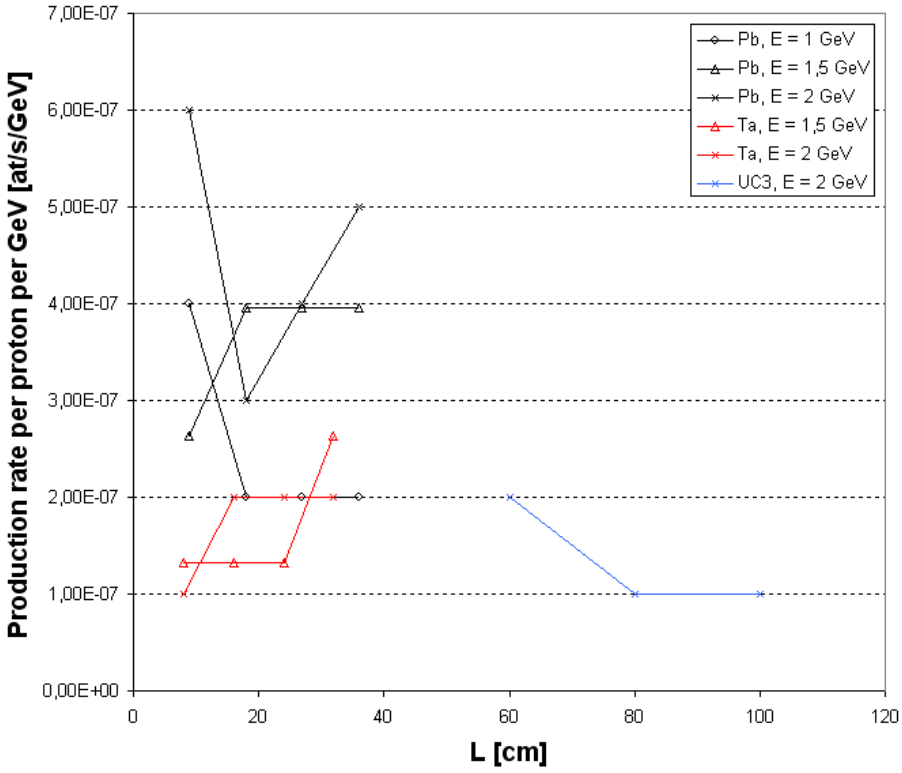

Figure 30: ^{63}Ga production rate per incident proton per GeV (R = 18 mm, spallation model = INCL4/ABLA, the low energetic secondary neutron flux contribution is taken into account, CINDER evolution time = 1 ms).

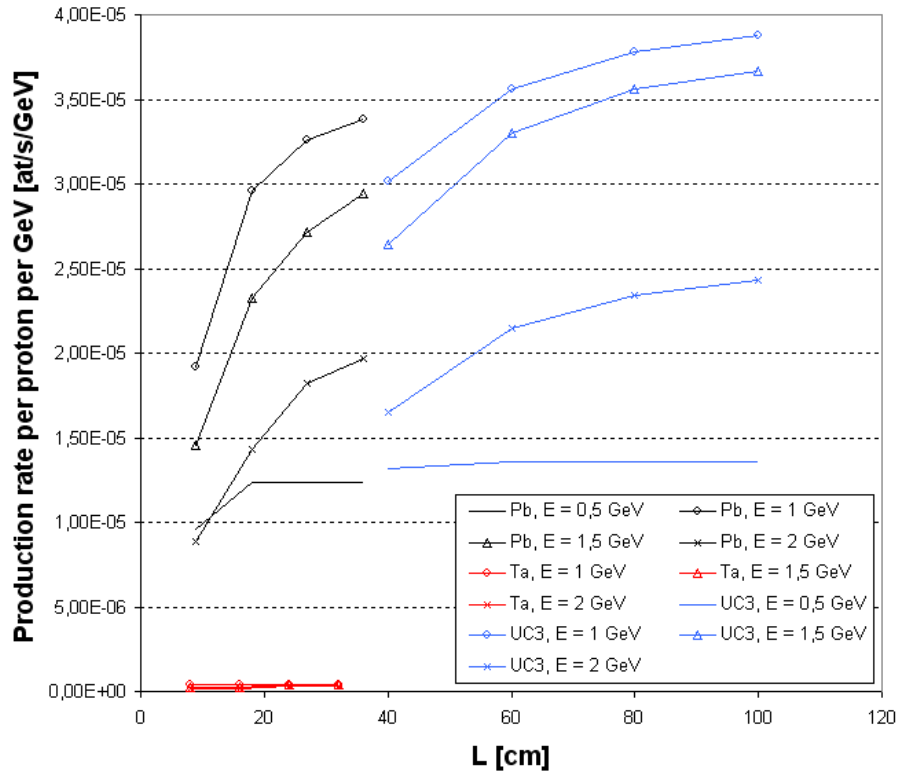

Figure 31: ^{63}Ga production rate per incident proton per GeV (R = 18 mm, spallation model = CEM2k, the low energetic secondary neutron flux contribution is taken into account, CINDER evolution time = 1 ms).

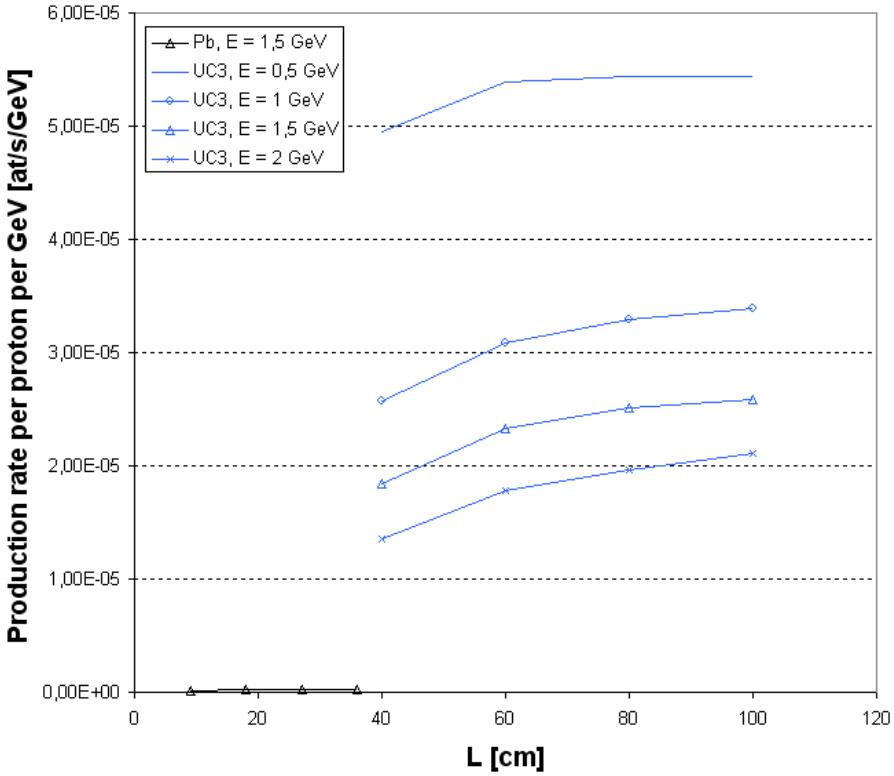

Figure 32: ^{81}Ga production rate per incident proton per GeV (R = 18 mm, spallation model = INCL4/ABLA, the low energetic secondary neutron flux contribution is taken into account, CINDER evolution time = 1 ms).

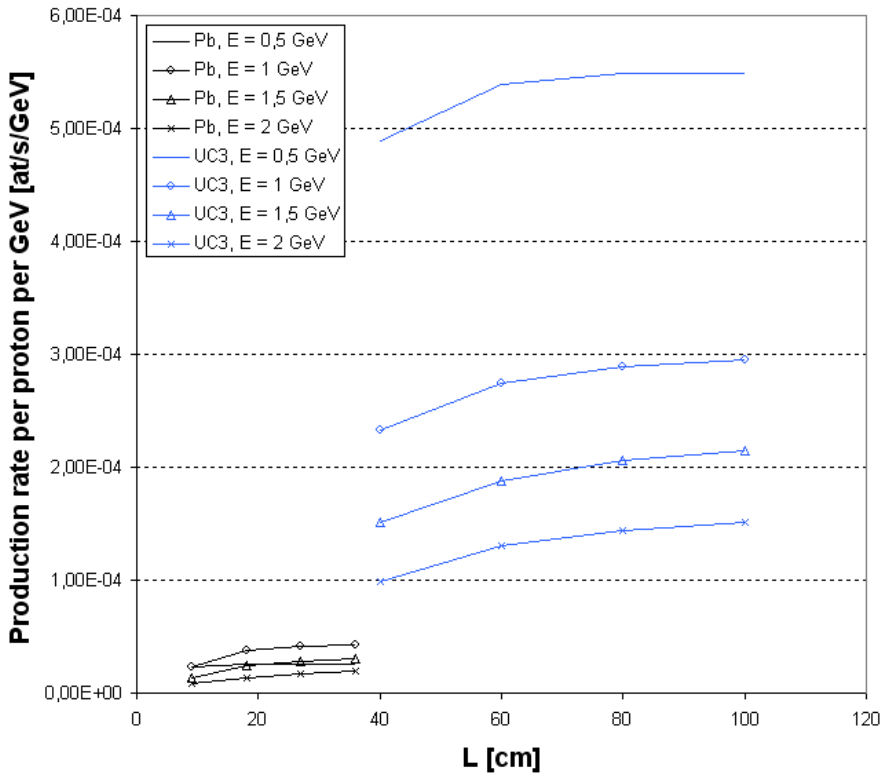

Figure 33: ^{81}Ga production rate per incident proton per GeV (R = 18 mm, spallation model = CEM2k, the low energetic secondary neutron flux contribution is taken into account, CINDER evolution time = 1 ms).

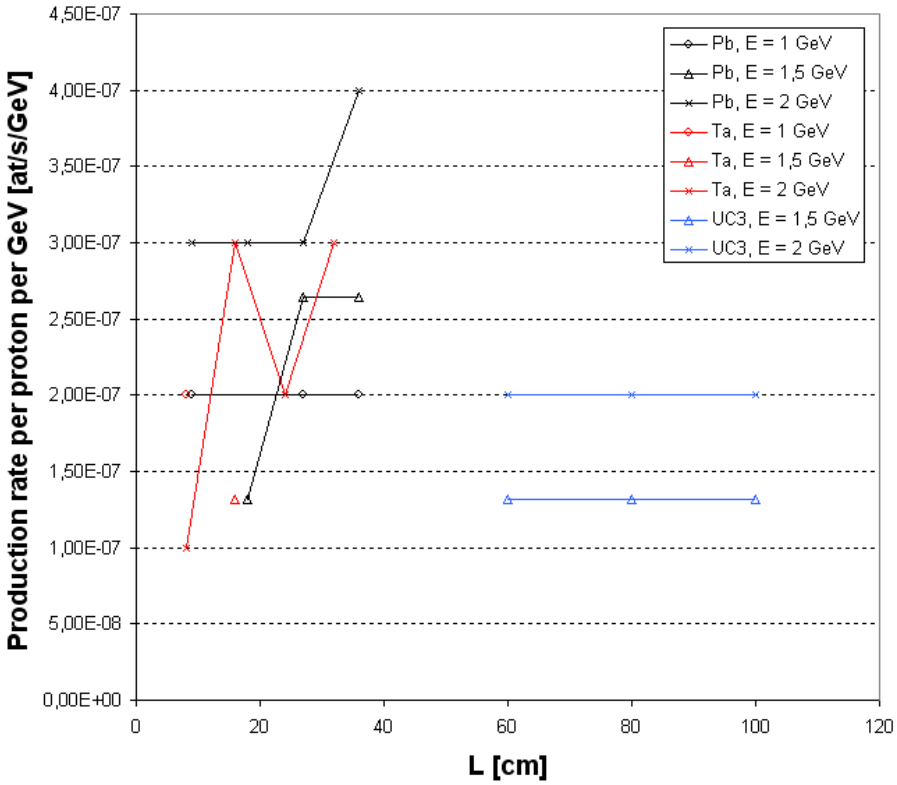

Figure 34: ^{74}Kr production rate per incident proton per GeV (R = 18 mm, spallation model = INCL4/ABLA, the low energetic secondary neutron flux contribution is taken into account, CINDER evolution time = 1 ms).

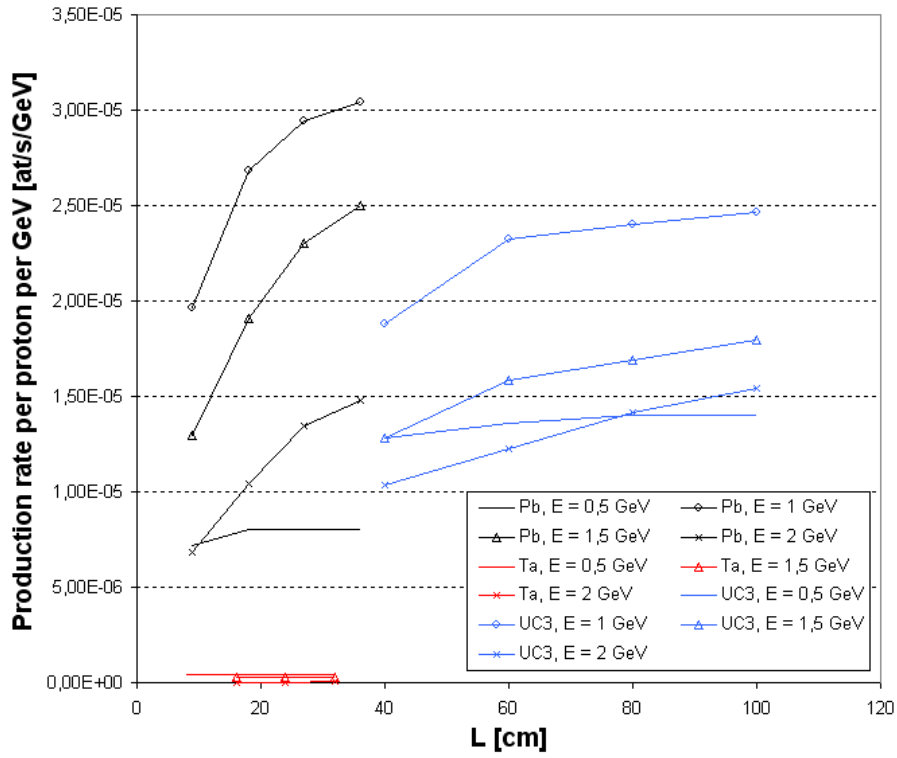

Figure 35: ^{74}Kr production rate per incident proton per GeV (R = 18 mm, spallation model = CEM2k, the low energetic secondary neutron flux contribution is taken into account, CINDER evolution time = 1 ms).

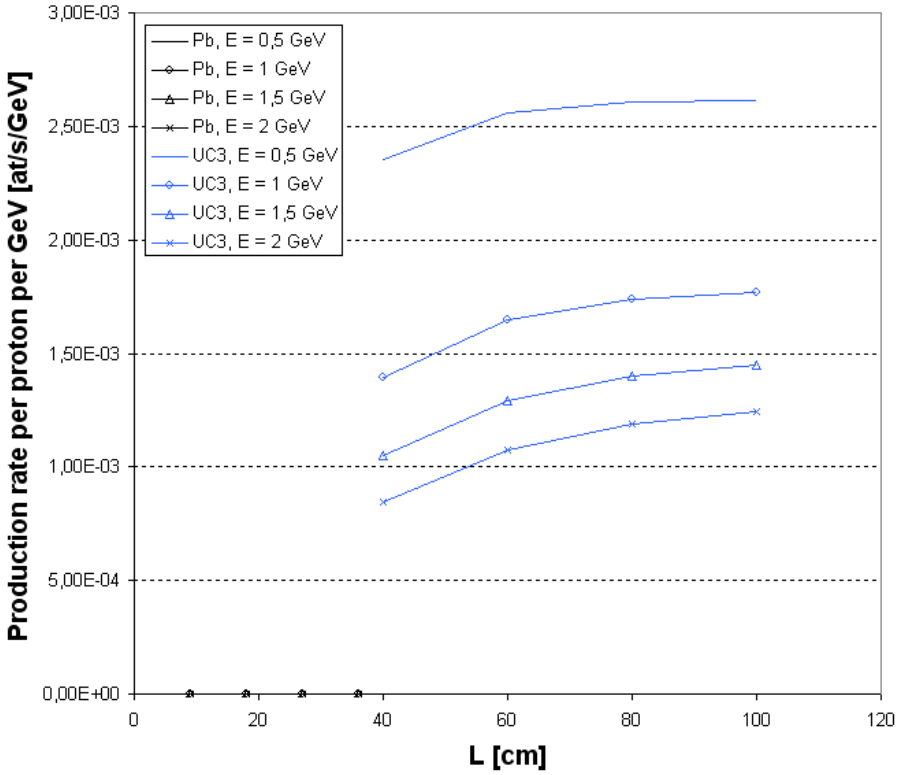

Figure 36: ^{92}Kr production rate per incident proton per GeV (R = 18 mm, spallation model = INCL4/ABLA, the low energetic secondary neutron flux contribution is taken into account, CINDER evolution time = 1 ms).

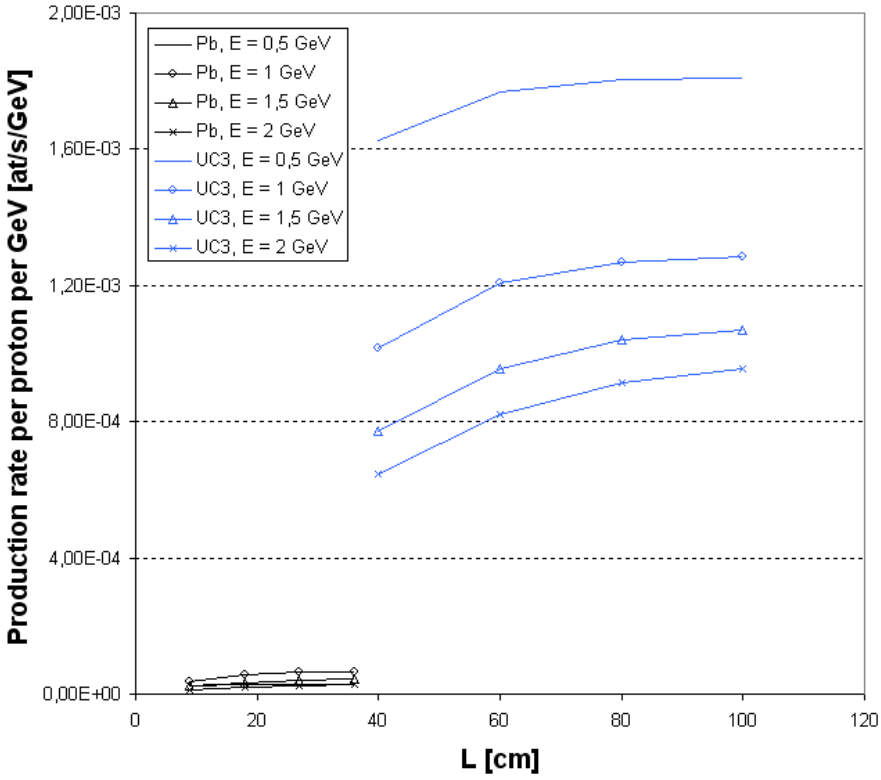

Figure 37: ^{92}Kr production rate per incident proton per GeV (R = 18 mm, spallation model = CEM2k, the low energetic secondary neutron flux contribution is taken into account, CINDER evolution time = 1 ms).

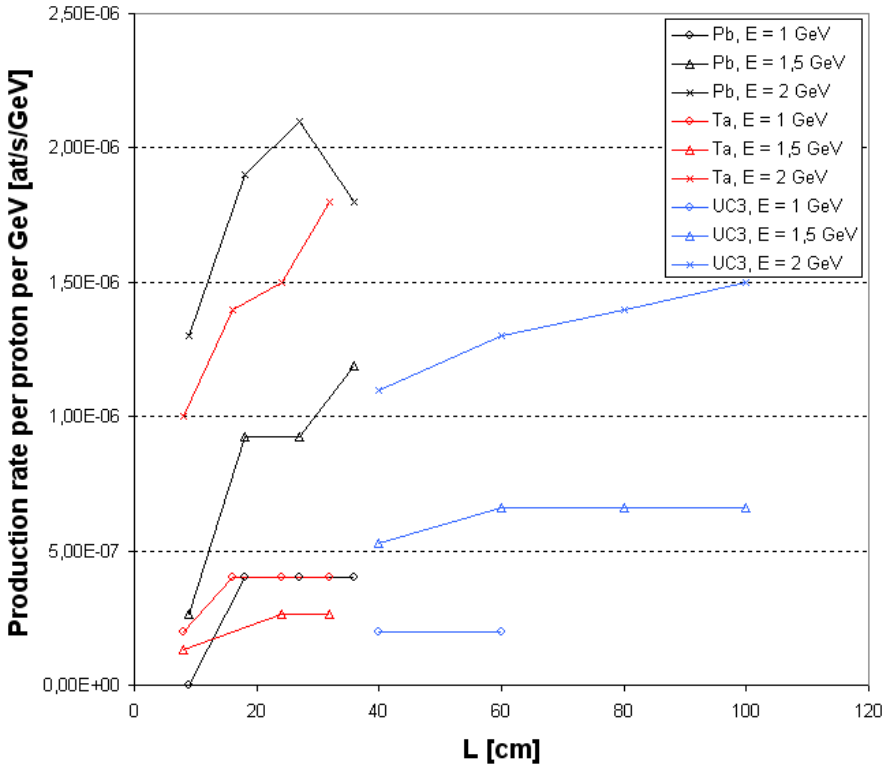

Figure 38: ^{107}Sn production rate per incident proton per GeV (R = 18 mm, spallation model = INCL4/ABLA, the low energetic secondary neutron flux contribution is taken into account, CINDER evolution time = 1 ms).

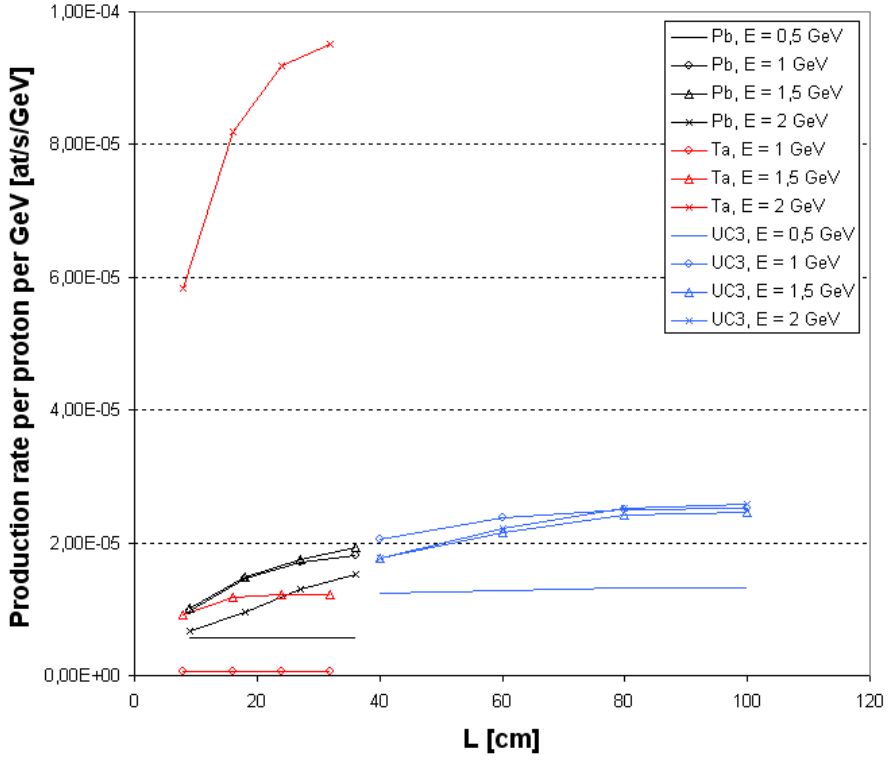

Figure 39: ^{107}Sn production rate per incident proton per GeV (R = 18 mm, spallation model = CEM2k, the low energetic secondary neutron flux contribution is taken into account, CINDER evolution time = 1 ms).

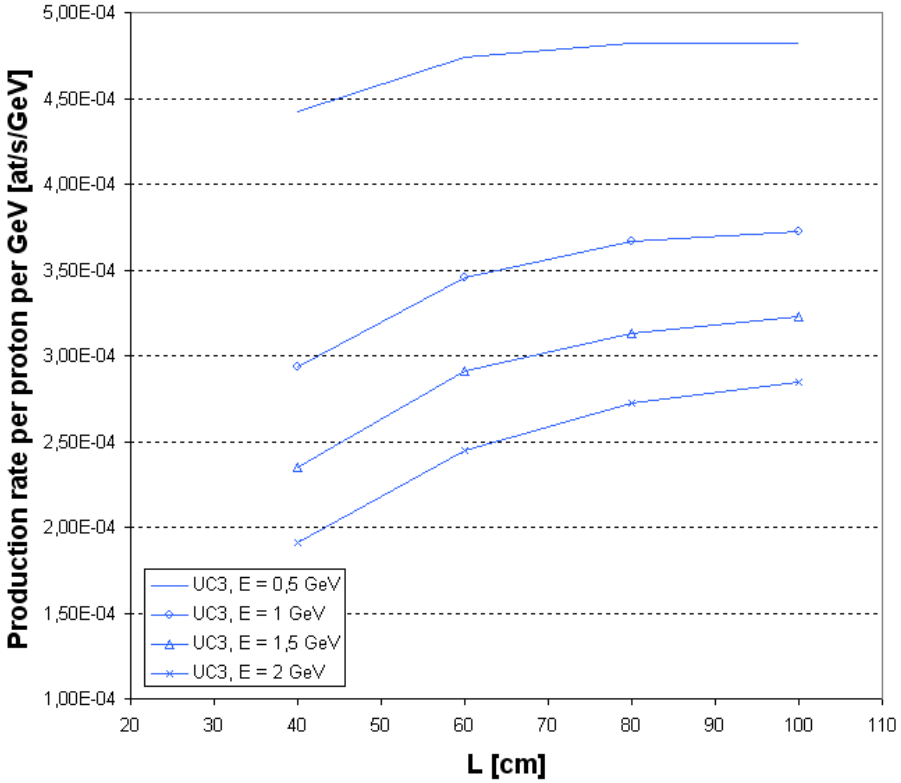

Figure 40: ^{132}Sn production rate per incident proton per GeV (R = 18 mm, spallation model = INCL4/ABLA, the low energetic secondary neutron flux contribution is taken into account, CINDER evolution time = 1 ms).

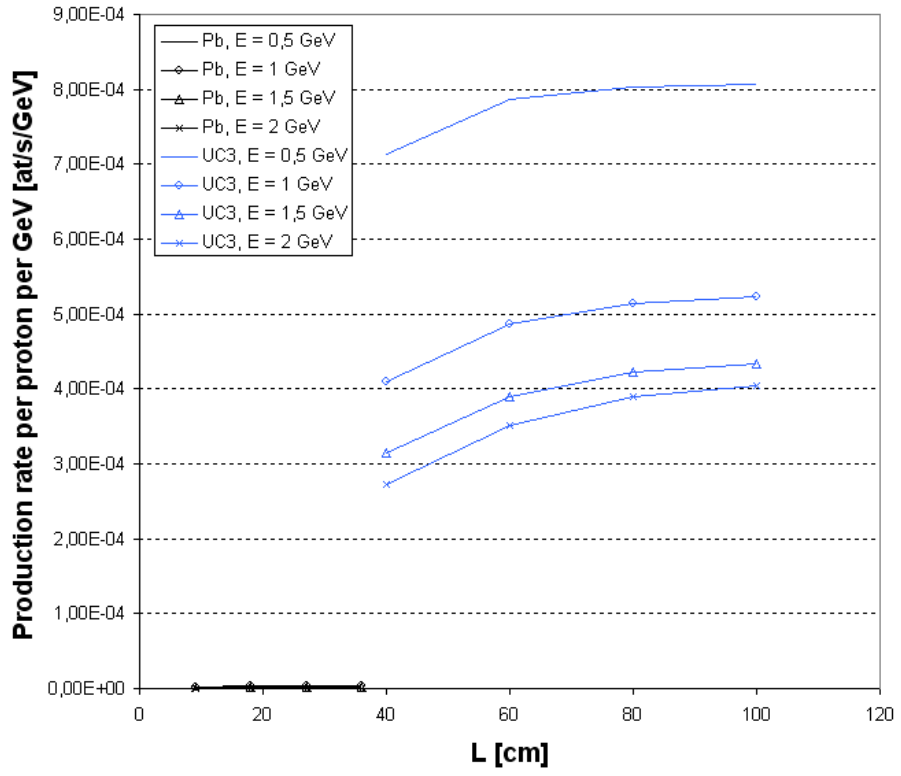

Figure 41: ^{132}Sn production rate per incident proton per GeV (R = 18 mm, spallation model = CEM2k, the low energetic secondary neutron flux contribution is taken into account, CINDER evolution time = 1 ms).

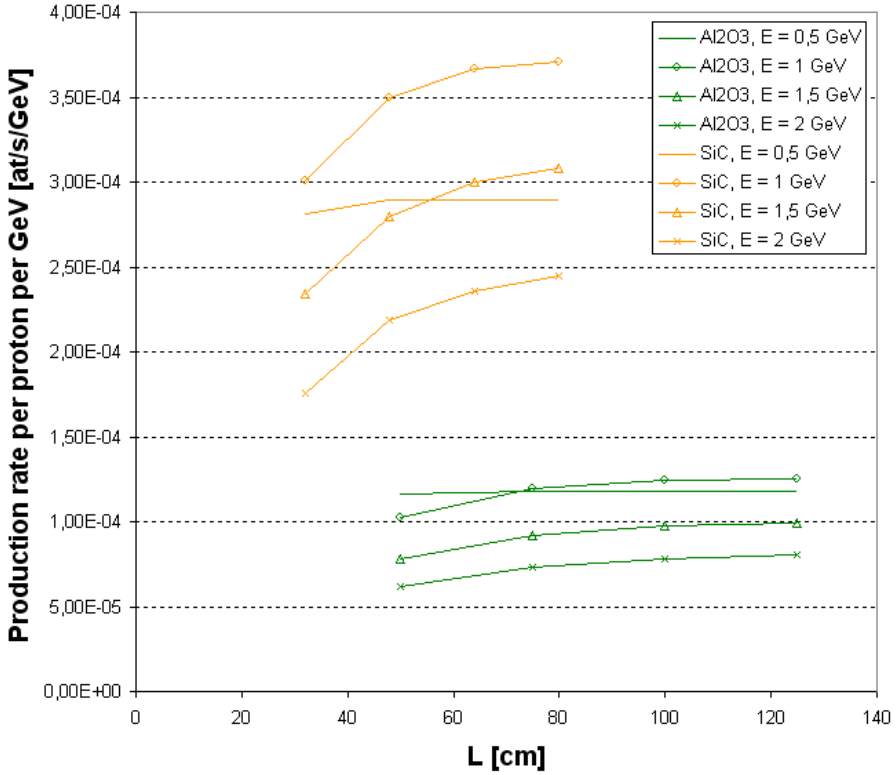

Figure 42: ^{20}Mg production rate per incident proton per GeV (R = 18 mm, spallation model = INCL4/ABLA, the low energetic secondary neutron flux contribution is taken into account, CINDER evolution time = 1 ms).

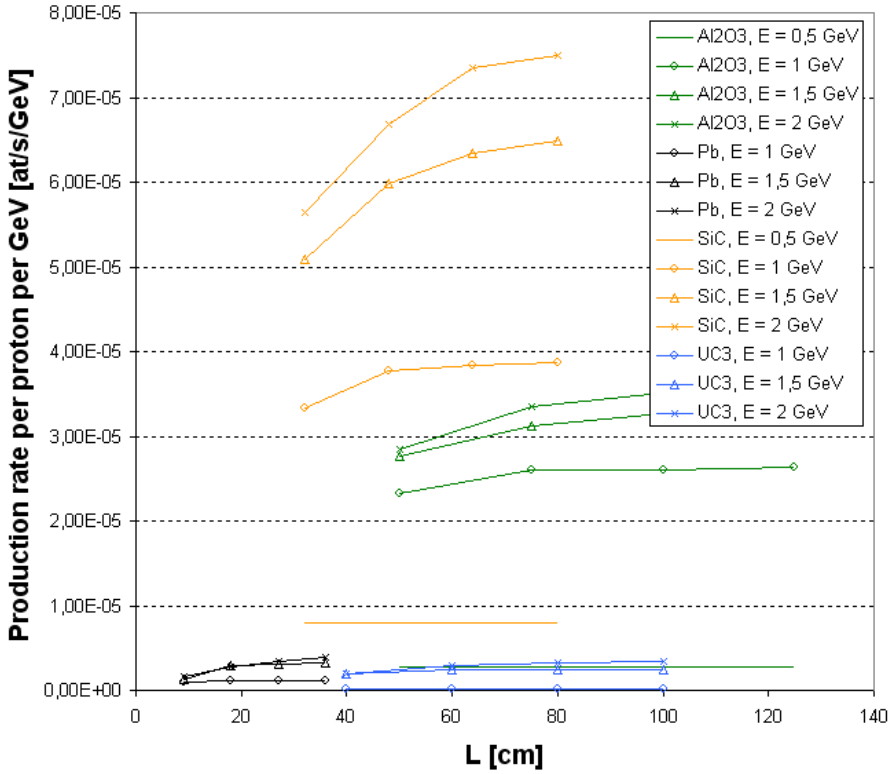

Figure 43: ^{20}Mg production rate per incident proton per GeV (R = 18 mm, spallation model = CEM2k, the low energetic secondary neutron flux contribution is taken into account, CINDER evolution time = 1 ms).

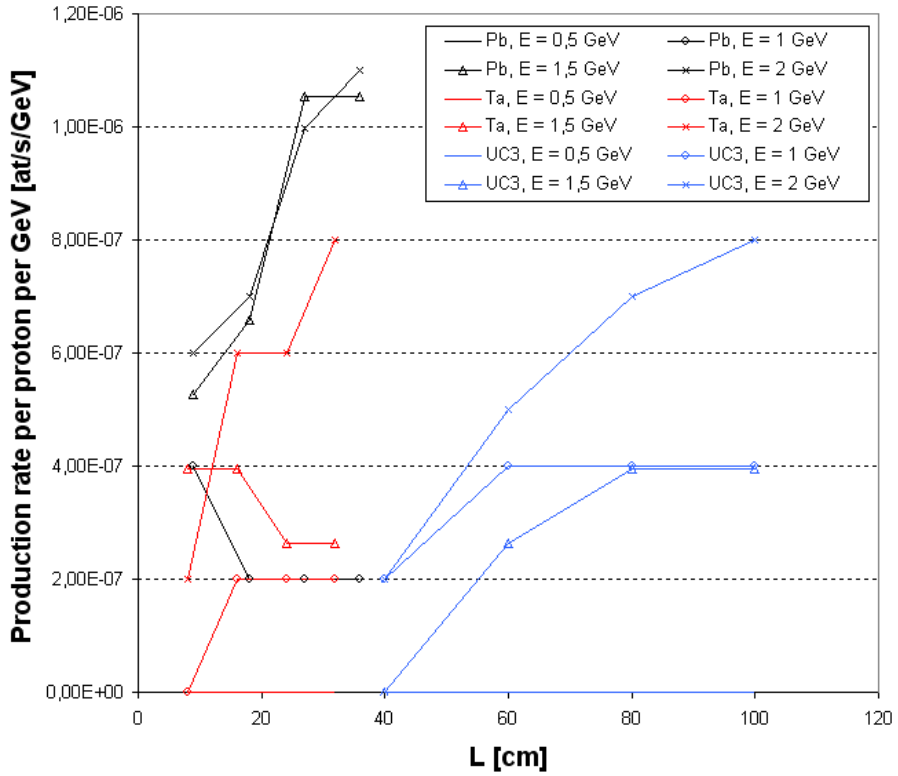

Figure 44: ^{30}Mg production rate per incident proton per GeV (R = 18 mm, spallation model = INCL4/ABLA, the low energetic secondary neutron flux contribution is taken into account, CINDER evolution time = 1 ms).

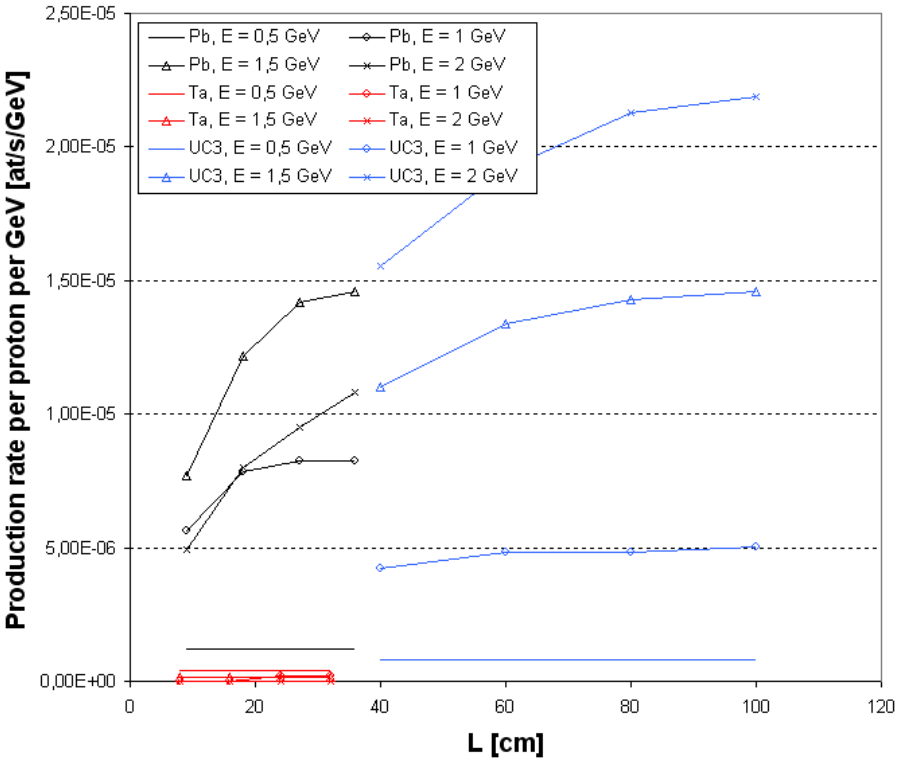

Figure 45: ^{30}Mg production rate per incident proton per GeV (R = 18 mm, spallation model = CEM2k, the low energetic secondary neutron flux contribution is taken into account, CINDER evolution time = 1 ms).

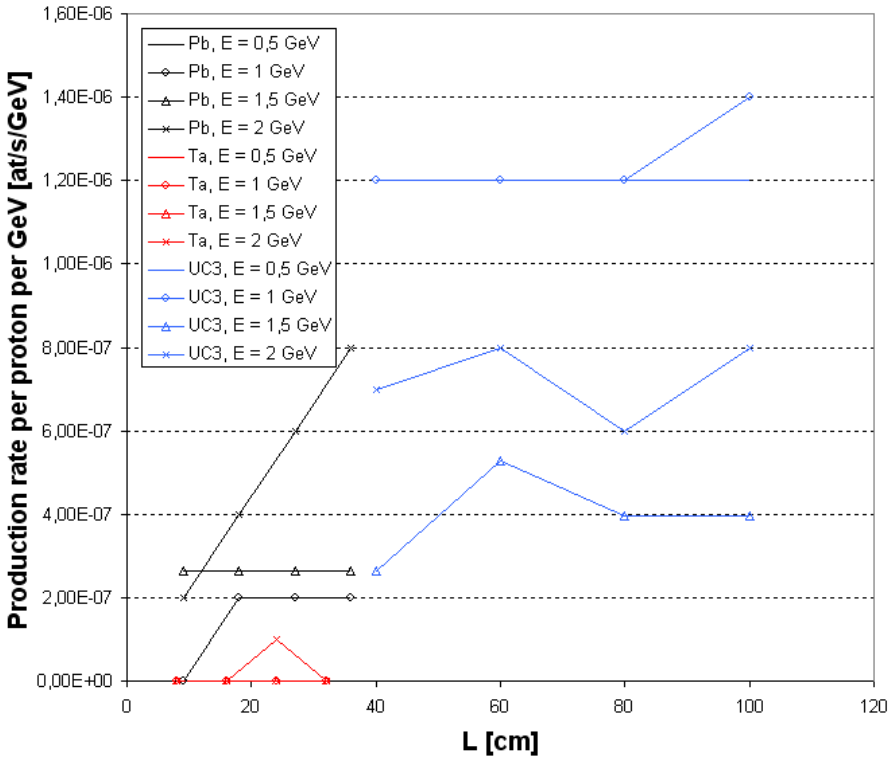

Figure 46: ^{46}Ar production rate per incident proton per GeV (R = 18 mm, spallation model = INCL4/ABLA, the low energetic secondary neutron flux contribution is taken into account, CINDER evolution time = 1 ms).

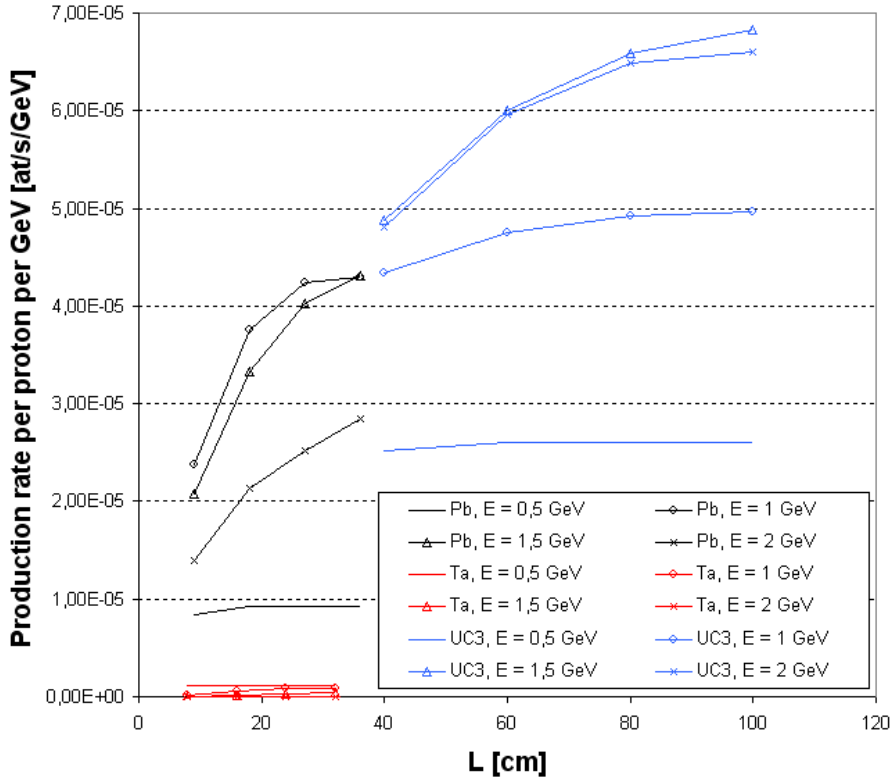

Figure 47: ^{46}Ar production rate per incident proton per GeV (R = 18 mm, spallation model = CEM2k, the low energetic secondary neutron flux contribution is taken into account, CINDER evolution time = 1 ms).

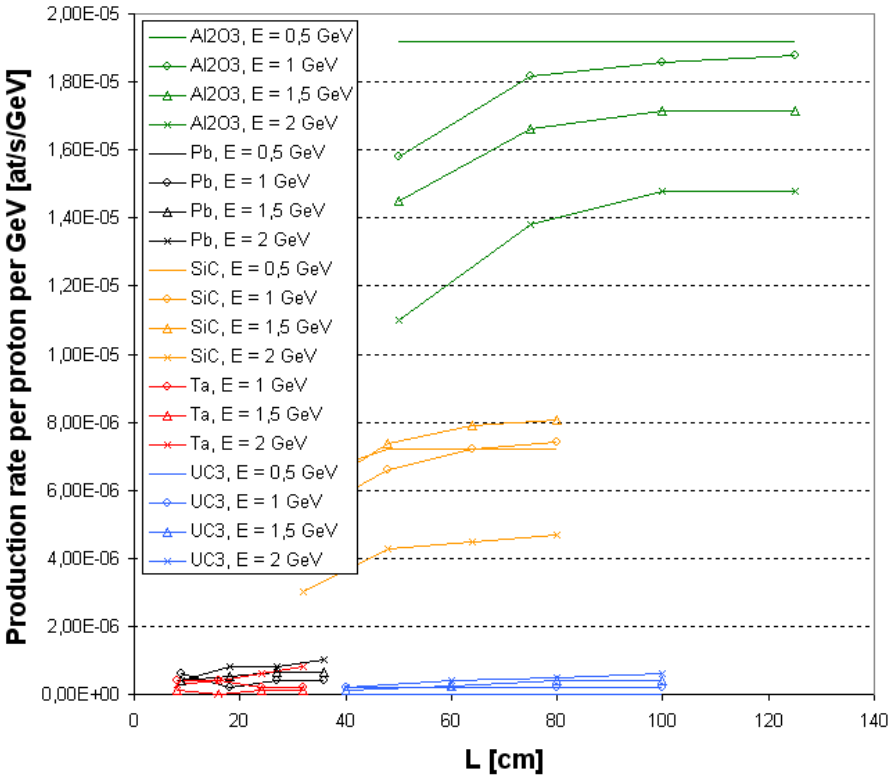

Figure 48: ^{25}Ne production rate per incident proton per GeV (R = 18 mm, spallation model = INCL4/ABLA, the low energetic secondary neutron flux contribution is taken into account, CINDER evolution time = 1 ms).

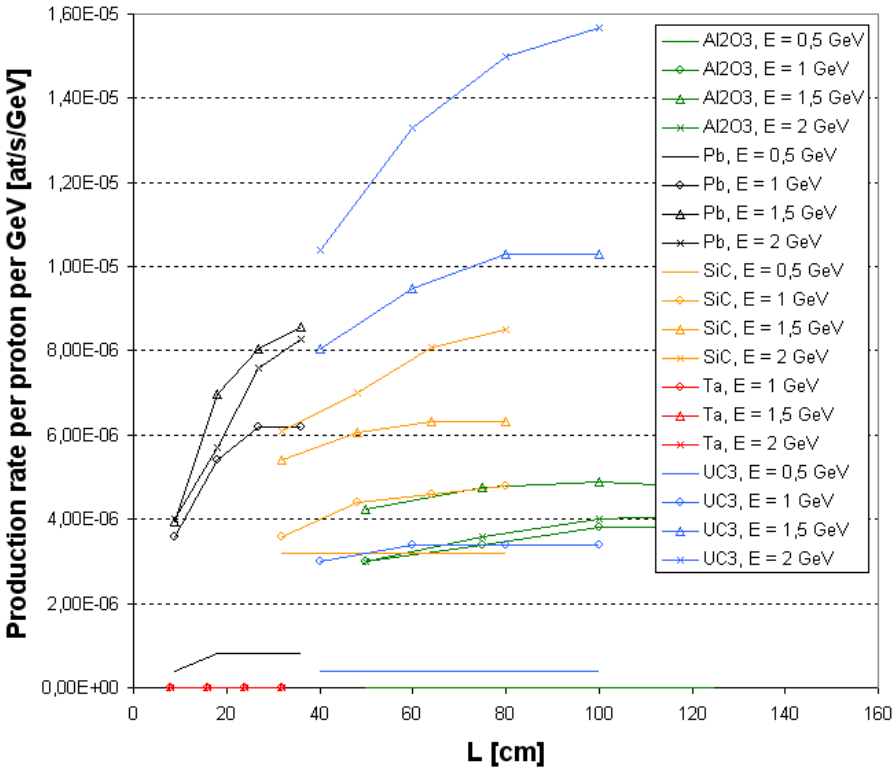

Figure 49: ^{25}Ne production rate per incident proton per GeV (R = 18 mm, spallation model = CEM2k, the low energetic secondary neutron flux contribution is taken into account, CINDER evolution time = 1 ms).

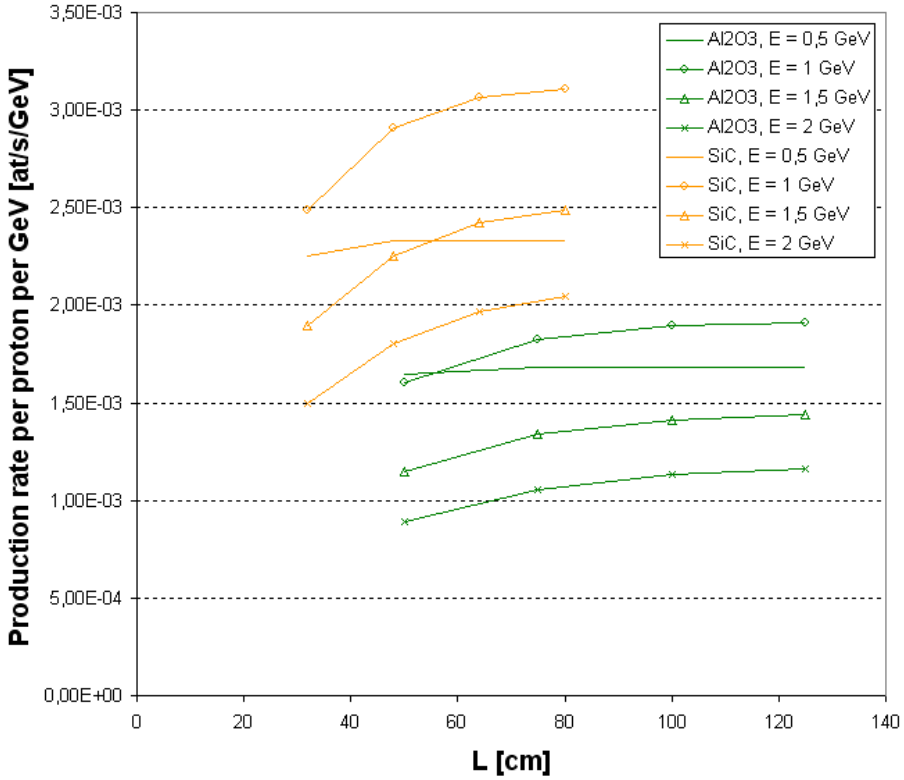

Figure 50: ^{18}Ne production rate per incident proton per GeV (R = 18 mm, spallation model = INCL4/ABLA, the low energetic secondary neutron flux contribution is taken into account, CINDER evolution time = 1 ms).

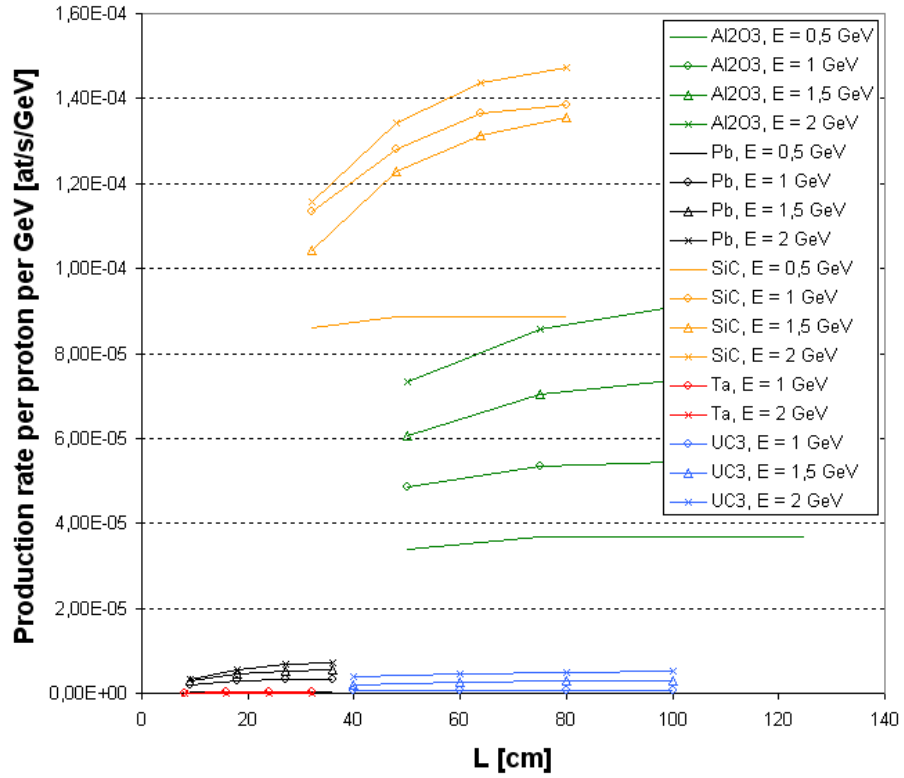

Figure 51: ^{18}Ne production rate per incident proton per GeV (R = 18 mm, spallation model = CEM2k, the low energetic secondary neutron flux contribution is taken into account, CINDER evolution time = 1 ms).

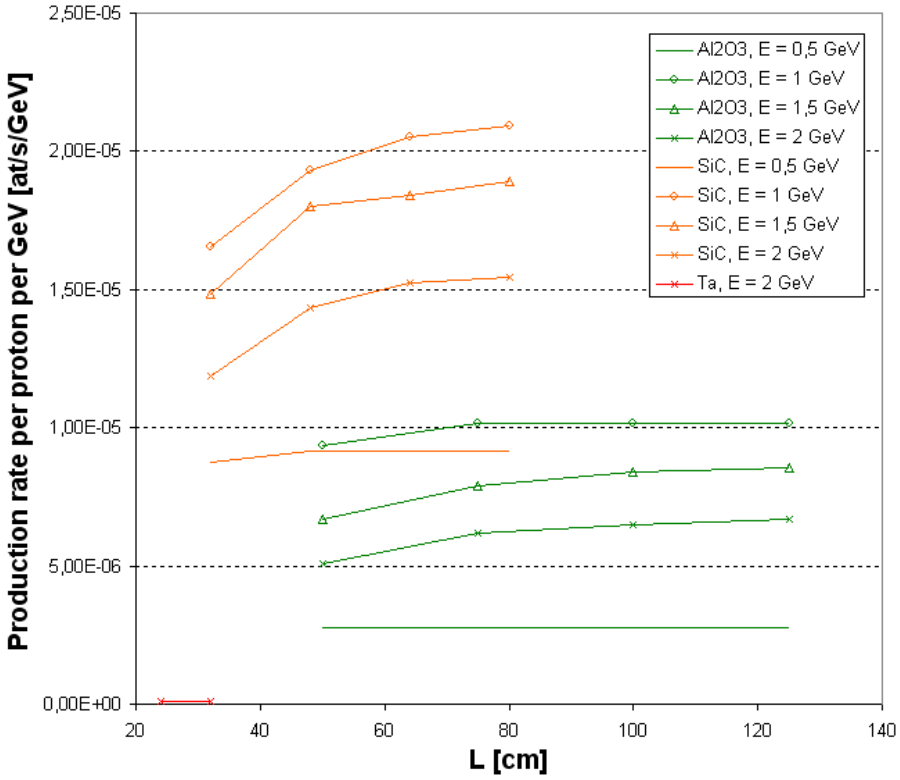

Figure 52: ^{17}Ne production rate per incident proton per GeV (R = 18 mm, spallation model = INCL4/ABLA, the low energetic secondary neutron flux contribution is taken into account, CINDER evolution time = 1 ms).

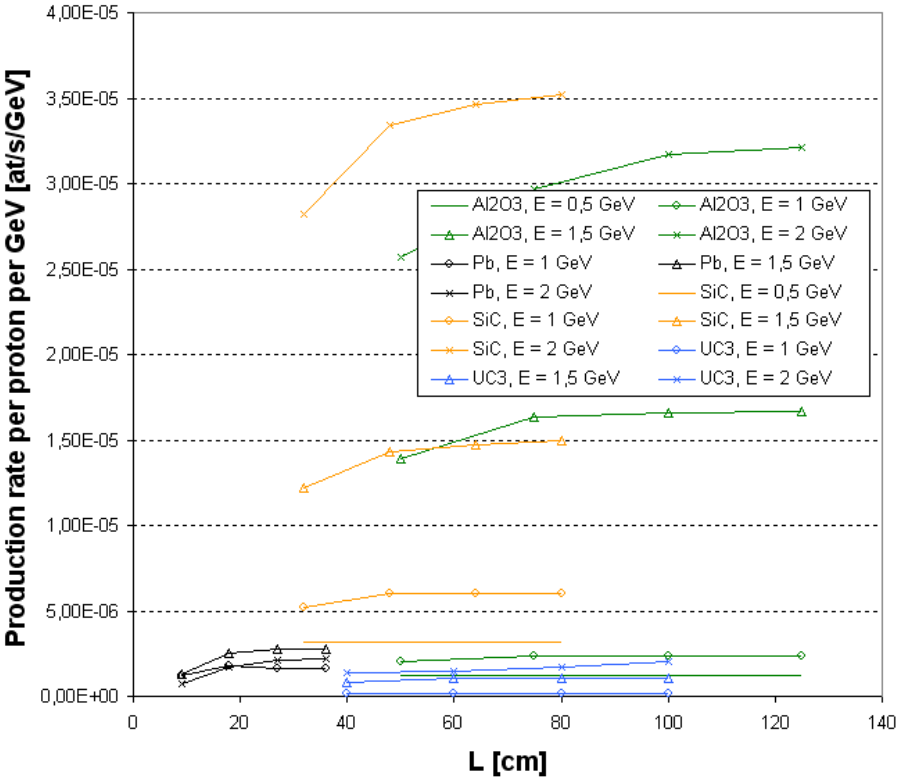

Figure 53: ^{17}Ne production rate per incident proton per GeV (R = 18 mm, spallation model = CEM2k, the low energetic secondary neutron flux contribution is taken into account, CINDER evolution time = 1 ms).

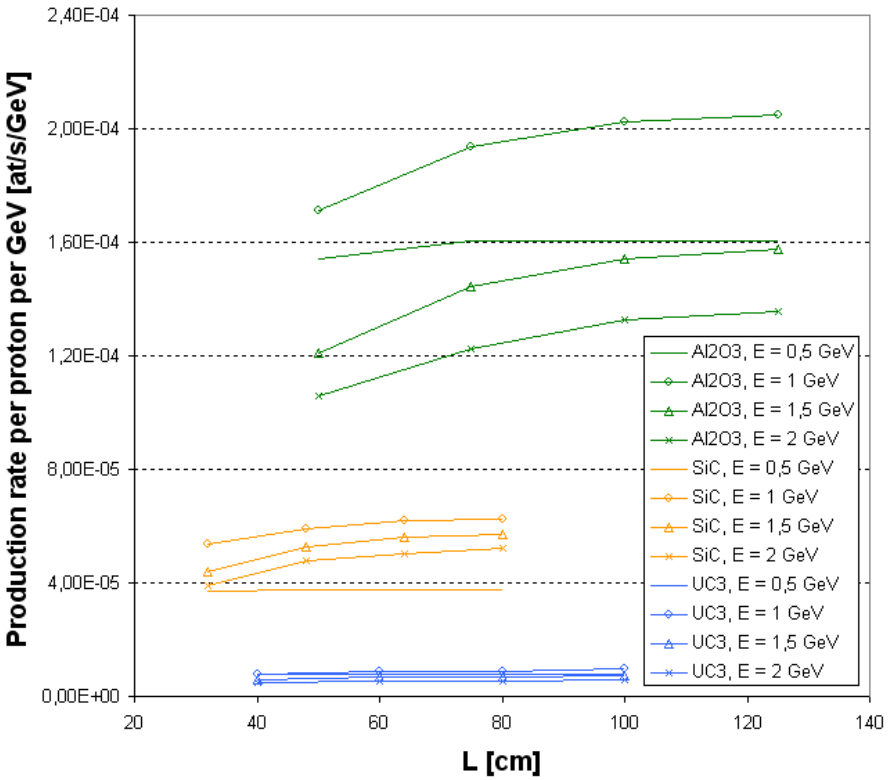

Figure 54: ^{11}Be production rate per incident proton per GeV (R = 18 mm, spallation model = INCL4/ABLA, the low energetic secondary neutron flux contribution is taken into account, CINDER evolution time = 1 ms).

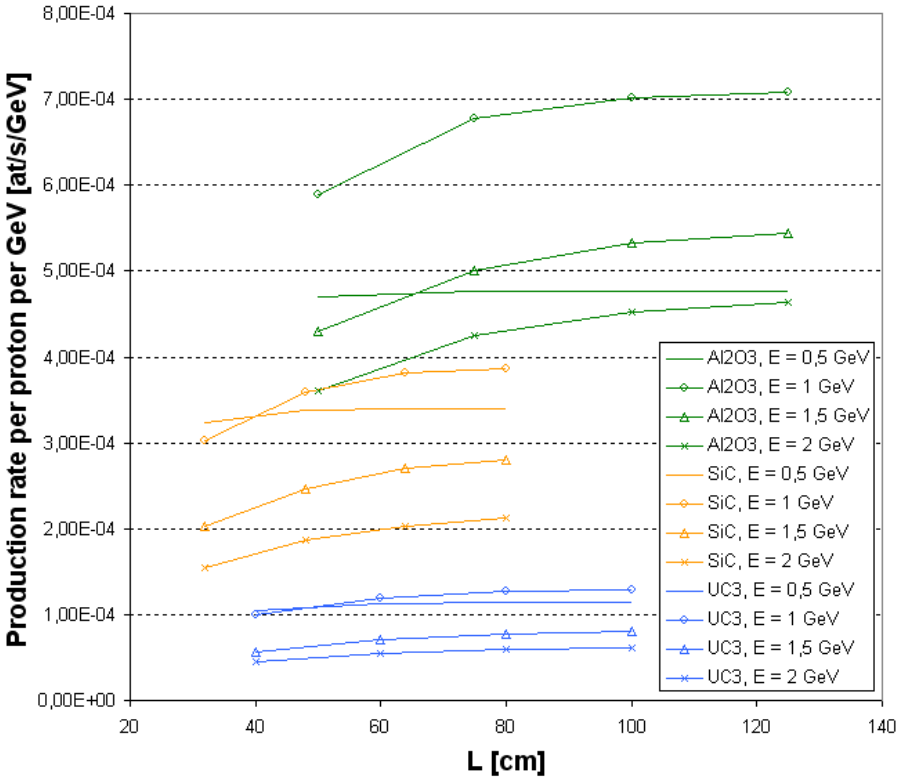

Figure 55: ^{11}Be production rate per incident proton per GeV (R = 18 mm, spallation model = CEM2k, the low energetic secondary neutron flux contribution is taken into account, CINDER evolution time = 1 ms).

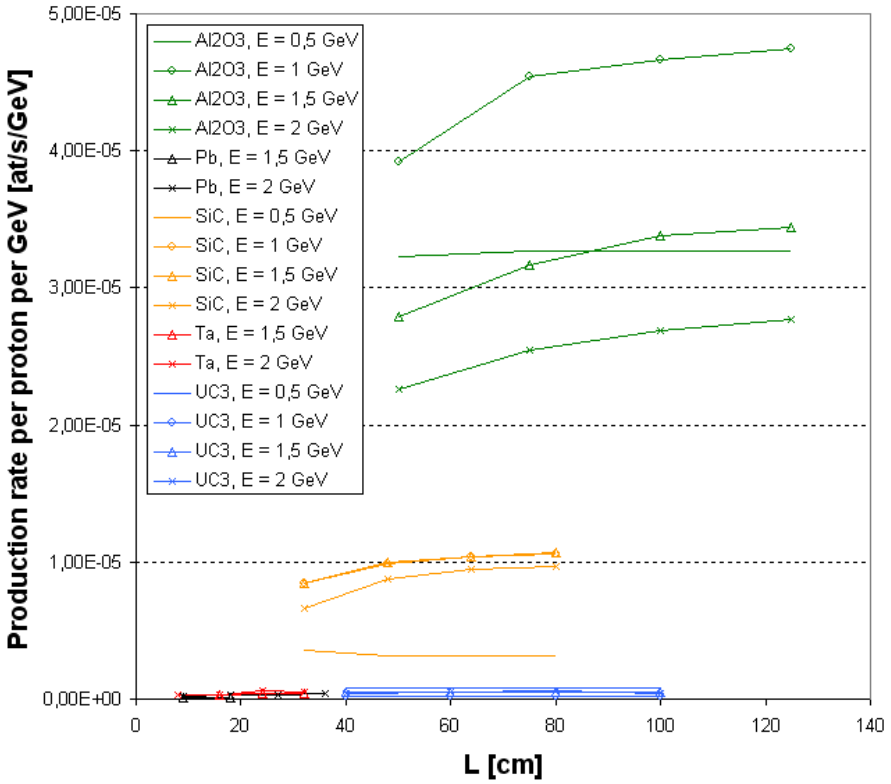

Figure 56: ^{12}Be production rate per incident proton per GeV (R = 18 mm, spallation model = INCL4/ABLA, the low energetic secondary neutron flux contribution is taken into account, CINDER evolution time = 1 ms).

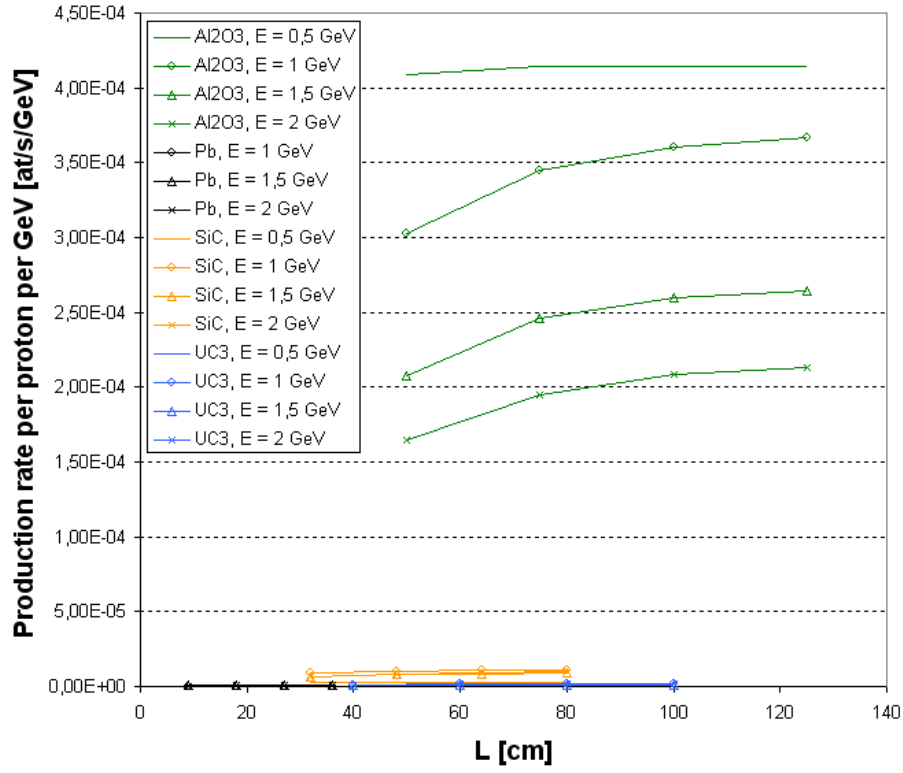

Figure 57: ^{12}Be production rate per incident proton per GeV (R = 18 mm, spallation model = CEM2k, the low energetic secondary neutron flux contribution is taken into account, CINDER evolution time = 1 ms).

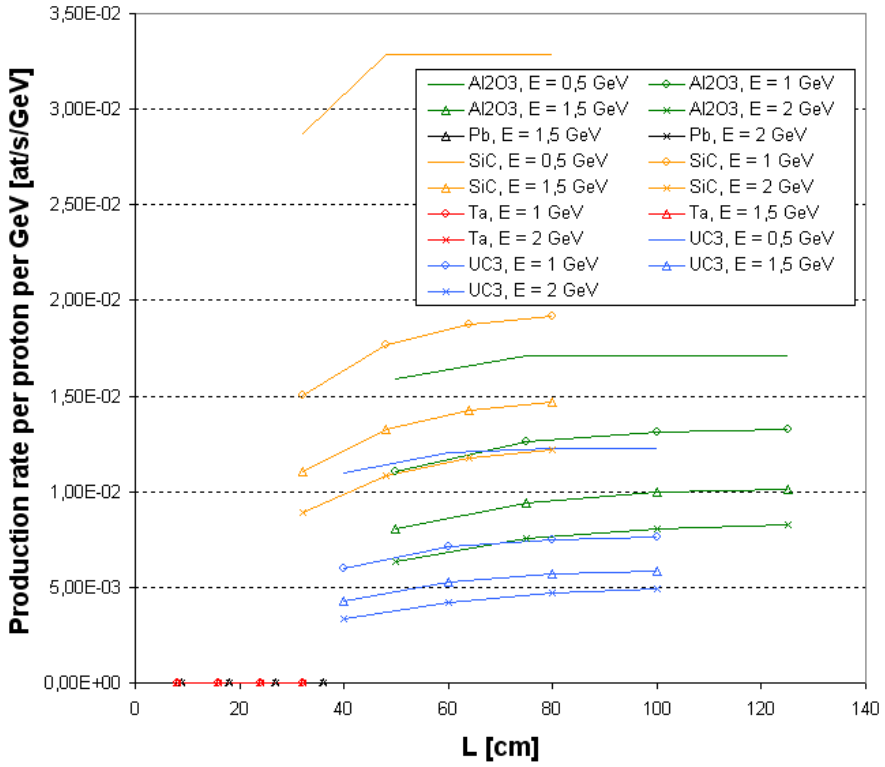

Figure 58: ^{7}Be production rate per incident proton per GeV (R = 18 mm, spallation model = INCL4/ABLA, the low energetic secondary neutron flux contribution is taken into account, CINDER evolution time = 1 ms).

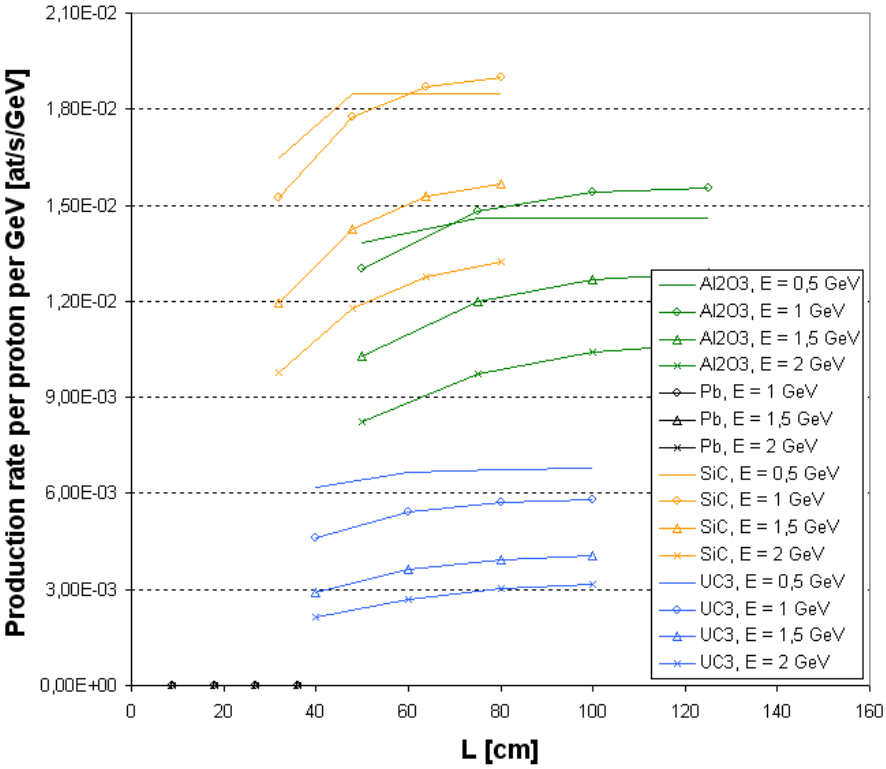

Figure 59: ^{7}Be production rate per incident proton per GeV (R = 18 mm, spallation model = CEM2k, the low energetic secondary neutron flux contribution is taken into account, CINDER evolution time = 1 ms).

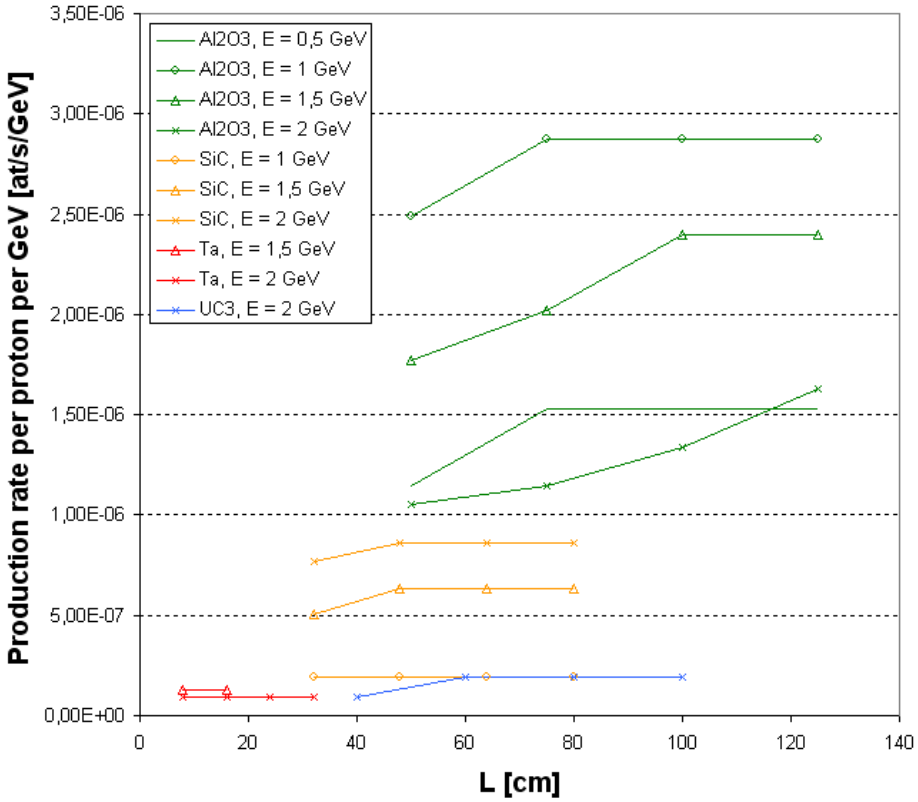

Figure 60: ^{11}Li production rate per incident proton per GeV (R = 18 mm, spallation model = INCL4/ABLA, the low energetic secondary neutron flux contribution is taken into account, CINDER evolution time = 1 ms).

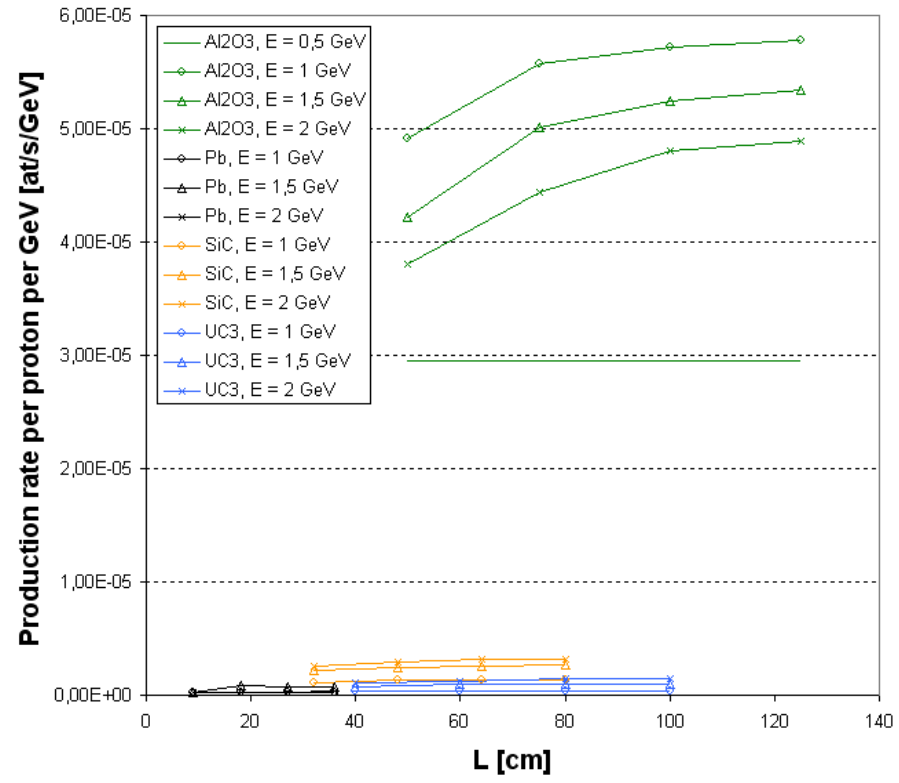

Figure 61: ^{11}Li production rate per incident proton per GeV (R = 18 mm, spallation model = CEM2k, the low energetic secondary neutron flux contribution is taken into account, CINDER evolution time = 1 ms).

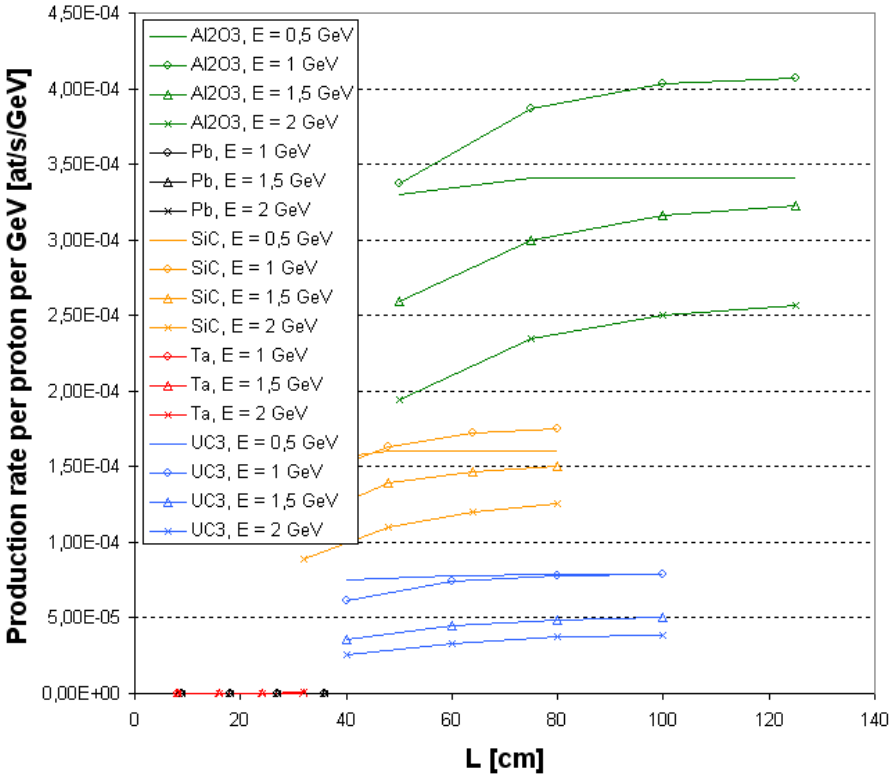

Figure 62: ^{9}Li production rate per incident proton per GeV (R = 18 mm, spallation model = INCL4/ABLA, the low energetic secondary neutron flux contribution is taken into account, CINDER evolution time = 1 ms).

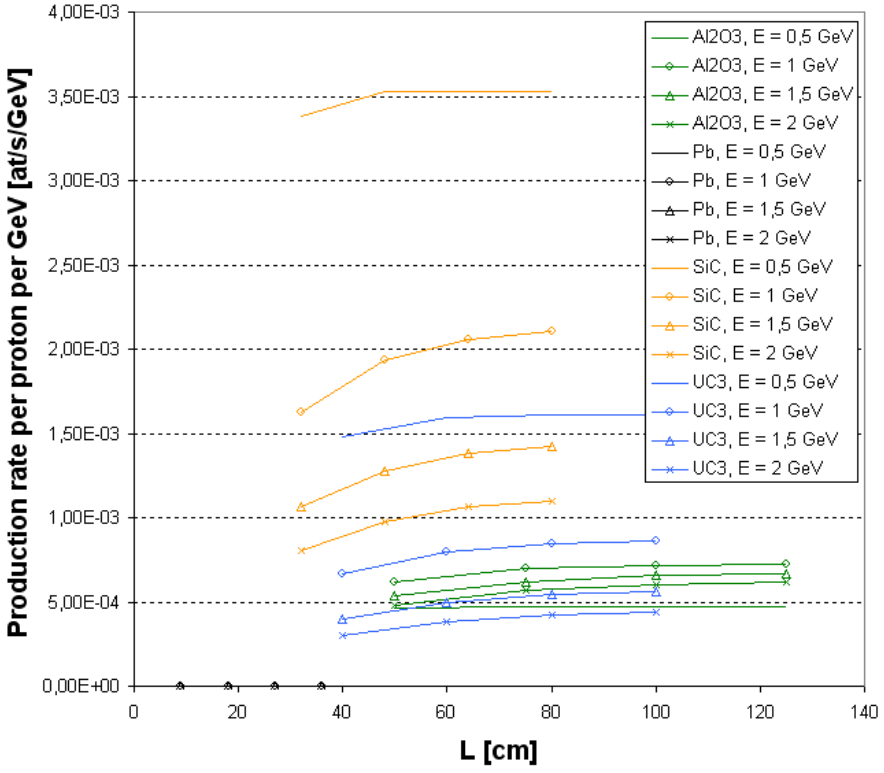

Figure 63: ^{9}Li production rate per incident proton per GeV (R = 18 mm, spallation model = CEM2k, the low energetic secondary neutron flux contribution is taken into account, CINDER evolution time = 1 ms).

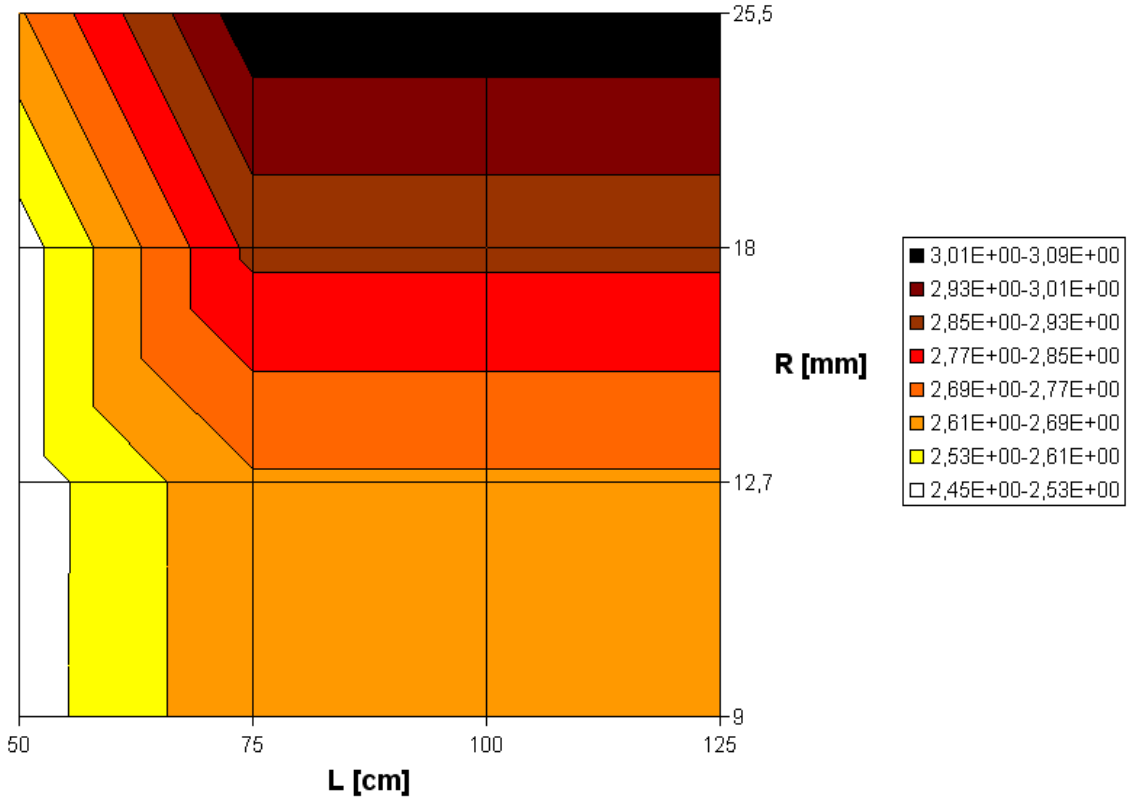

Figure 64: ^{11}Li production rate per incident proton [10^{-6} s^{-1}] as a function of target radius *R* and length *L*, (target = Al_2O_3, *E* = 1 GeV, model = INCL4/ABLA, the low energetic secondary neutron flux is taken into account, CINDER evolution time = 1 ms).

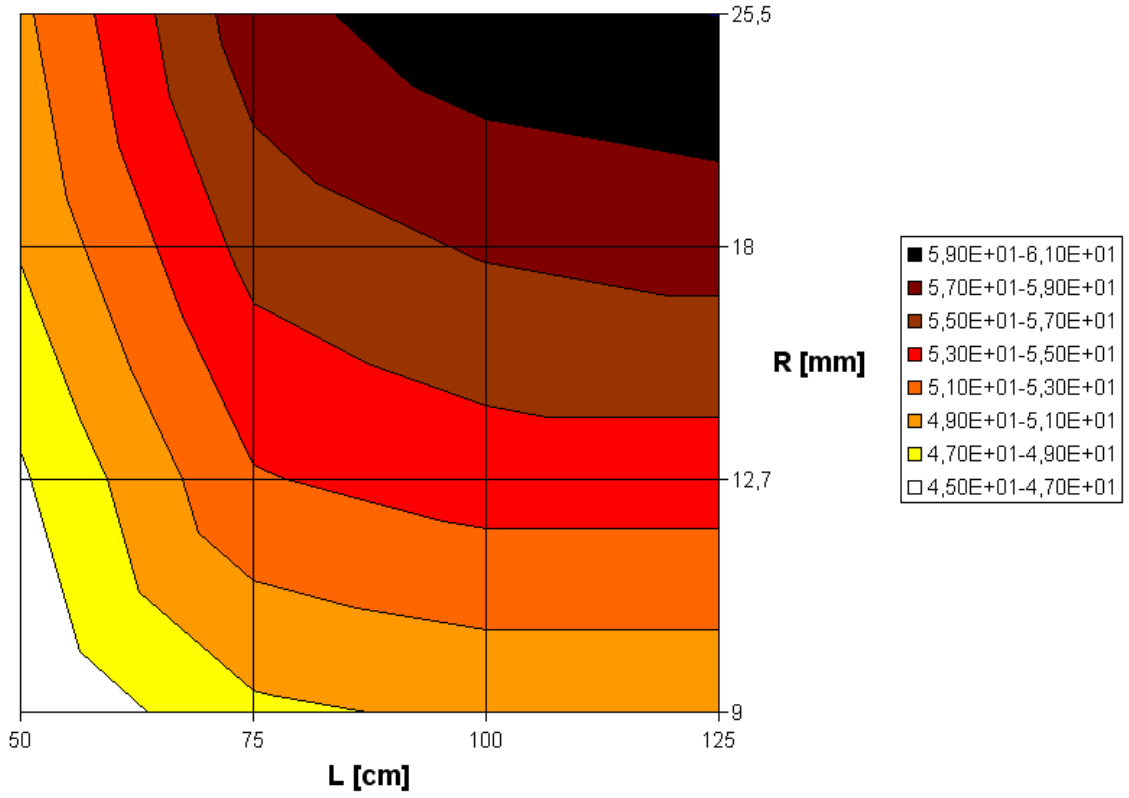

Figure 65: ^{11}Li production rate per incident proton [10^{-6} s^{-1}] as a function of target radius *R* and length *L*, (target = Al_2O_3, *E* = 1 GeV, model = CEM2k, the low energetic secondary neutron flux is taken into account, CINDER evolution time = 1 ms).

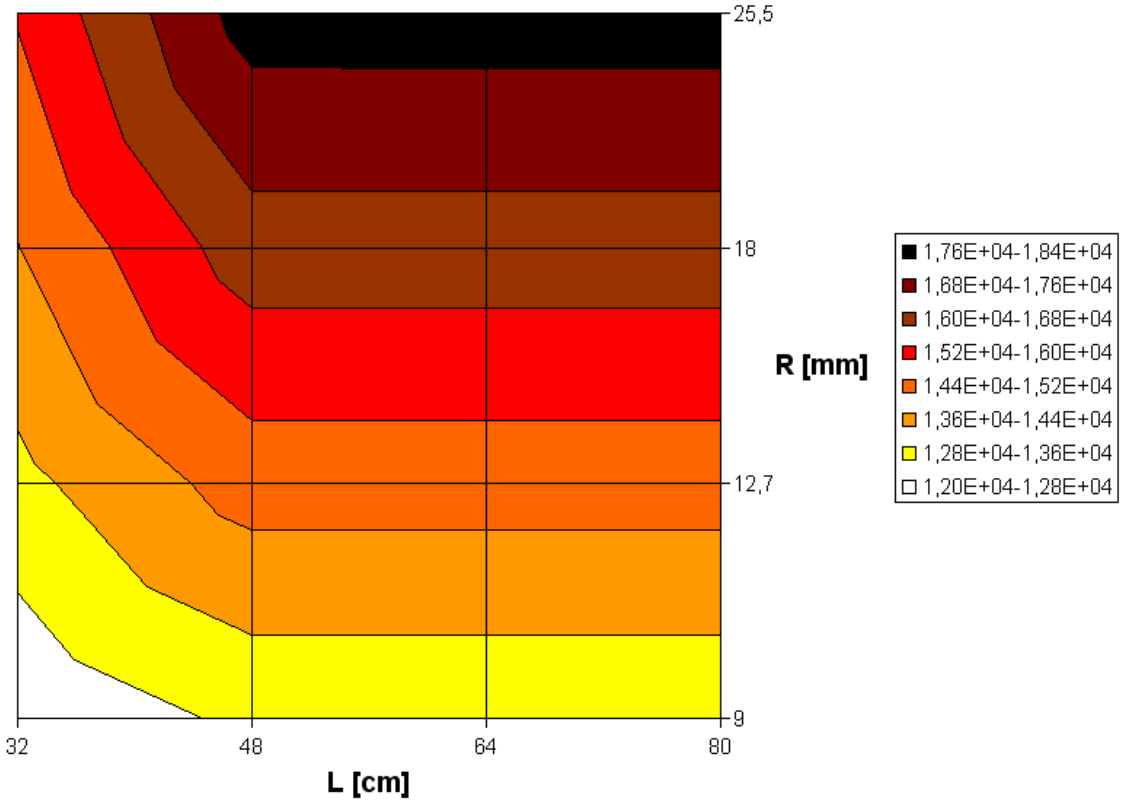

Figure 66: ^{7}Be production rate per incident proton [10^{-6} s^{-1}] as a function of target radius *R* and length *L*, (target = SiC, *E* = 0.5 GeV, model = INCL4/ABLA, the low energetic secondary neutron flux is taken into account, CINDER evolution time = 1 ms).

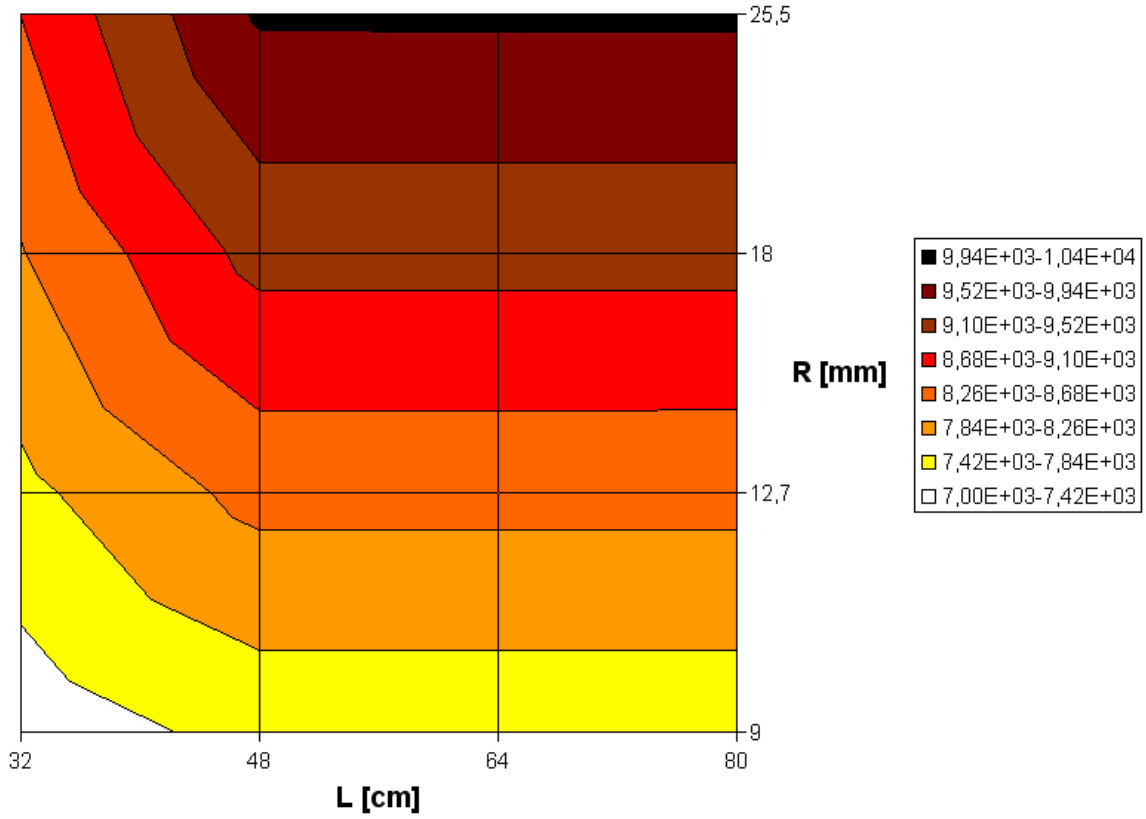

Figure 67: ^{7}Be production rate per incident proton [10^{-6} s^{-1}] as a function of target radius *R* and length *L*, (target = SiC, *E* = 0.5 GeV, model = CEM2k, the low energetic secondary neutron flux is taken into account, CINDER evolution time = 1 ms).

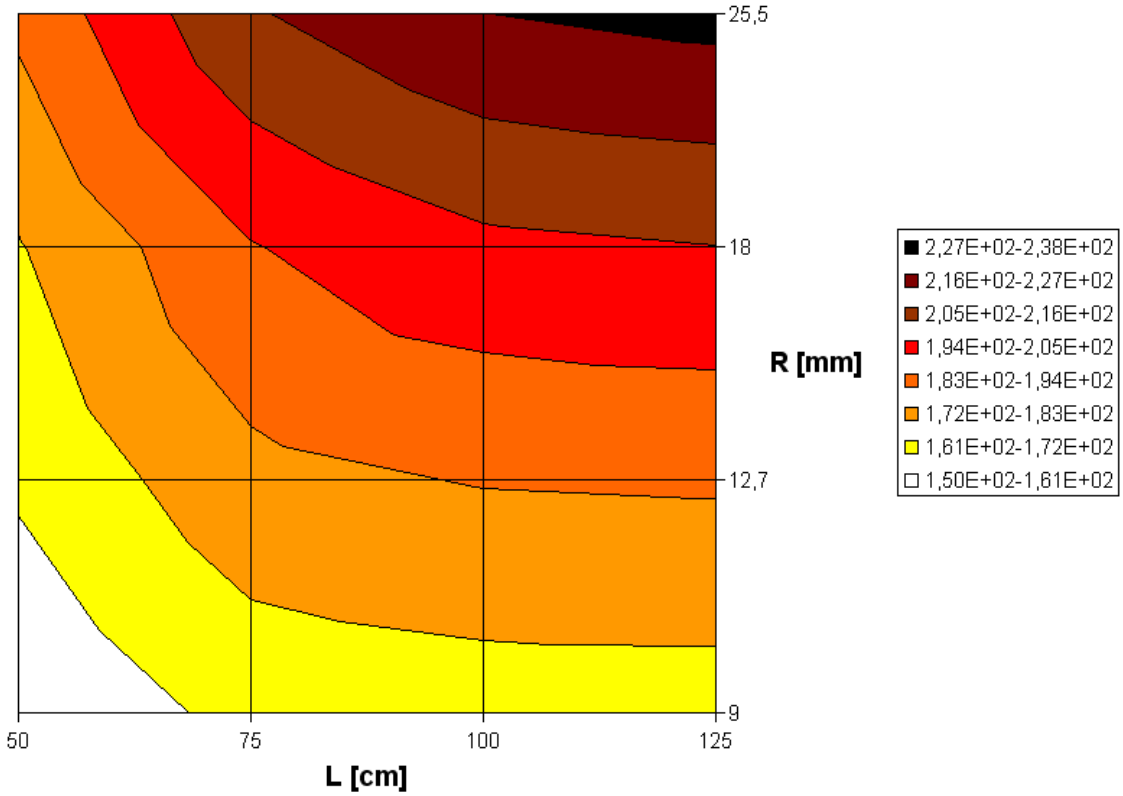

Figure 68: ^{11}Be production rate per incident proton [10^{-6} s^{-1}] as a function of target radius *R* and length *L*, (target = Al_2O_3, *E* = 1 GeV, model = INCL4/ABLA, the low energetic secondary neutron flux is taken into account, CINDER evolution time = 1 ms).

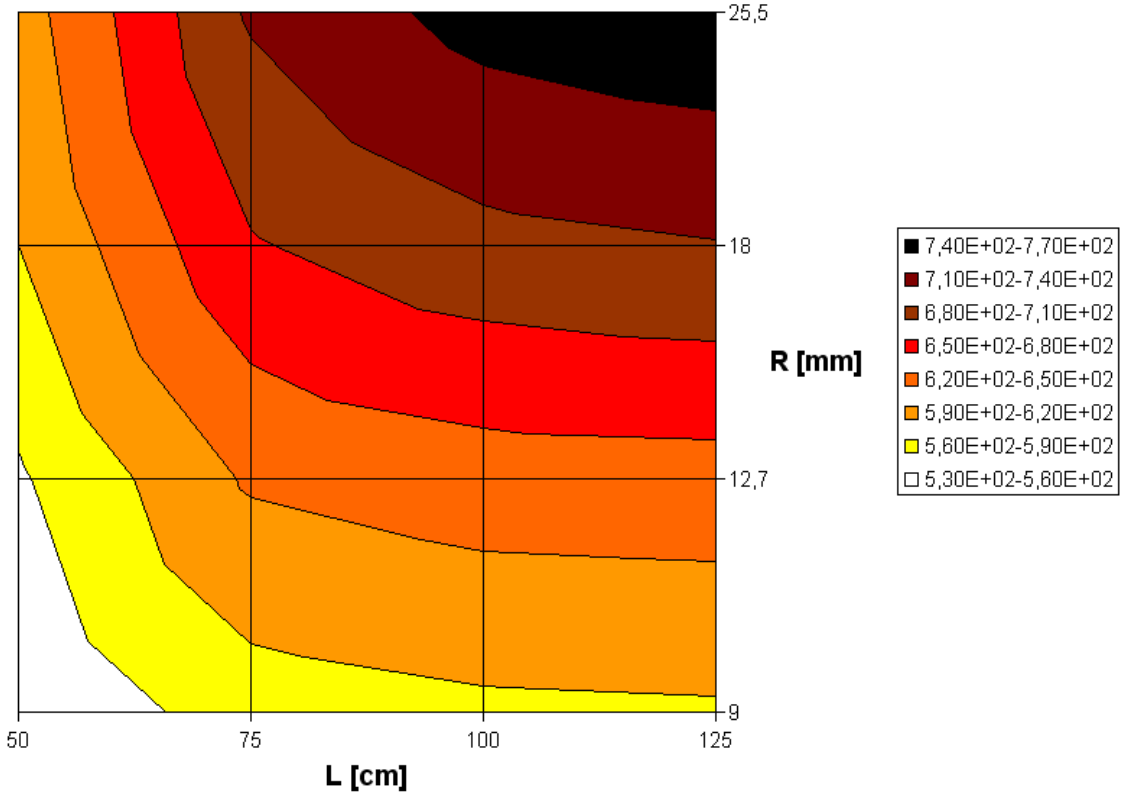

Figure 69: ^{11}Be production rate per incident proton [10^{-6} s^{-1}] as a function of target radius *R* and length *L*, (target = Al_2O_3, *E* = 1 GeV, model = CEM2k, the low energetic secondary neutron flux is taken into account, CINDER evolution time = 1 ms).

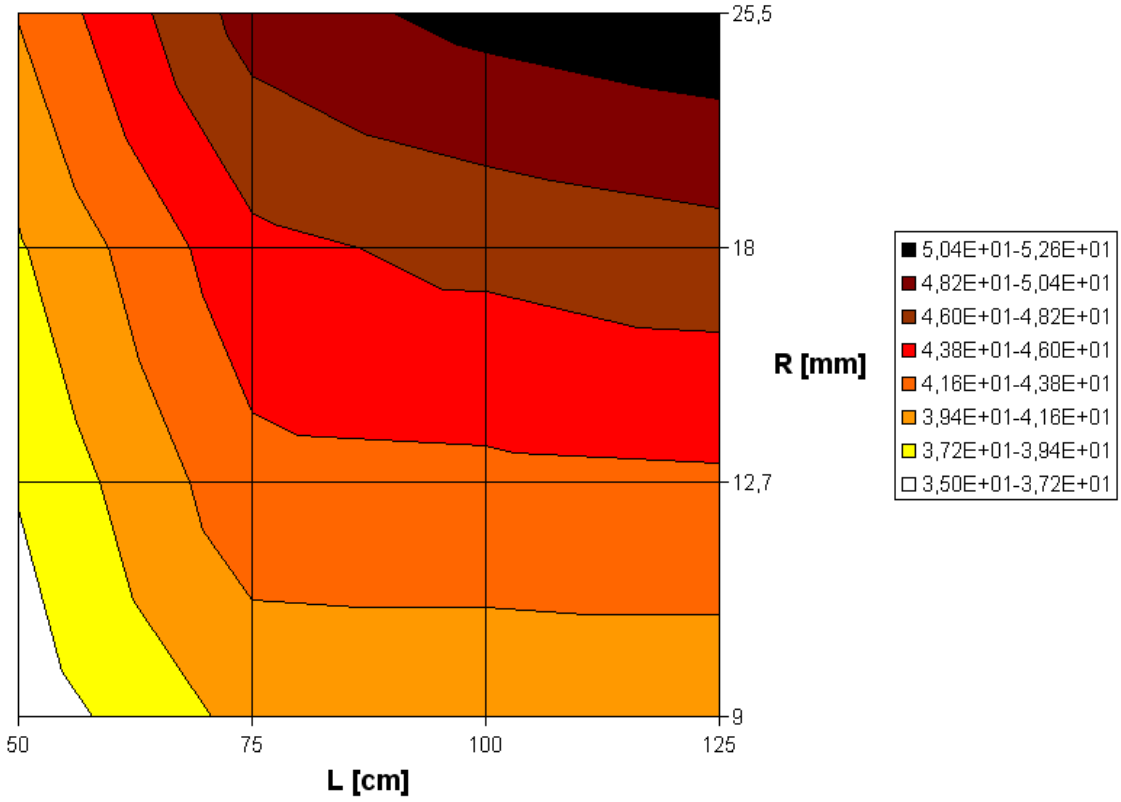

Figure 70: ^{12}Be production rate per incident proton [10^{-6} s^{-1}] as a function of target radius *R* and length *L*, (target = Al_2O_3, *E* = 1 GeV, model = INCL4/ABLA, the low energetic secondary neutron flux is taken into account, CINDER evolution time = 1 ms).

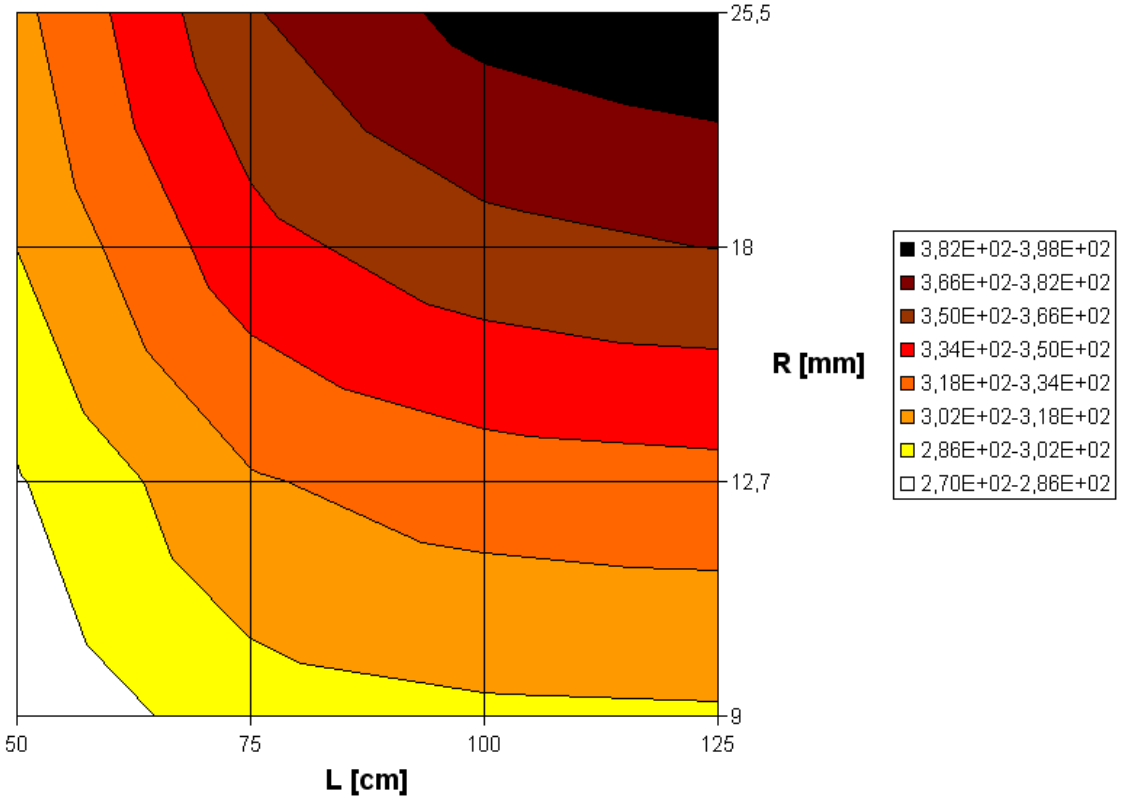

Figure 71: ^{12}Be production rate per incident proton [10^{-6} s^{-1}] as a function of target radius *R* and length *L*, (target = Al_2O_3, *E* = 1 GeV, model = CEM2k, the low energetic secondary neutron flux is taken into account, CINDER evolution time = 1 ms).

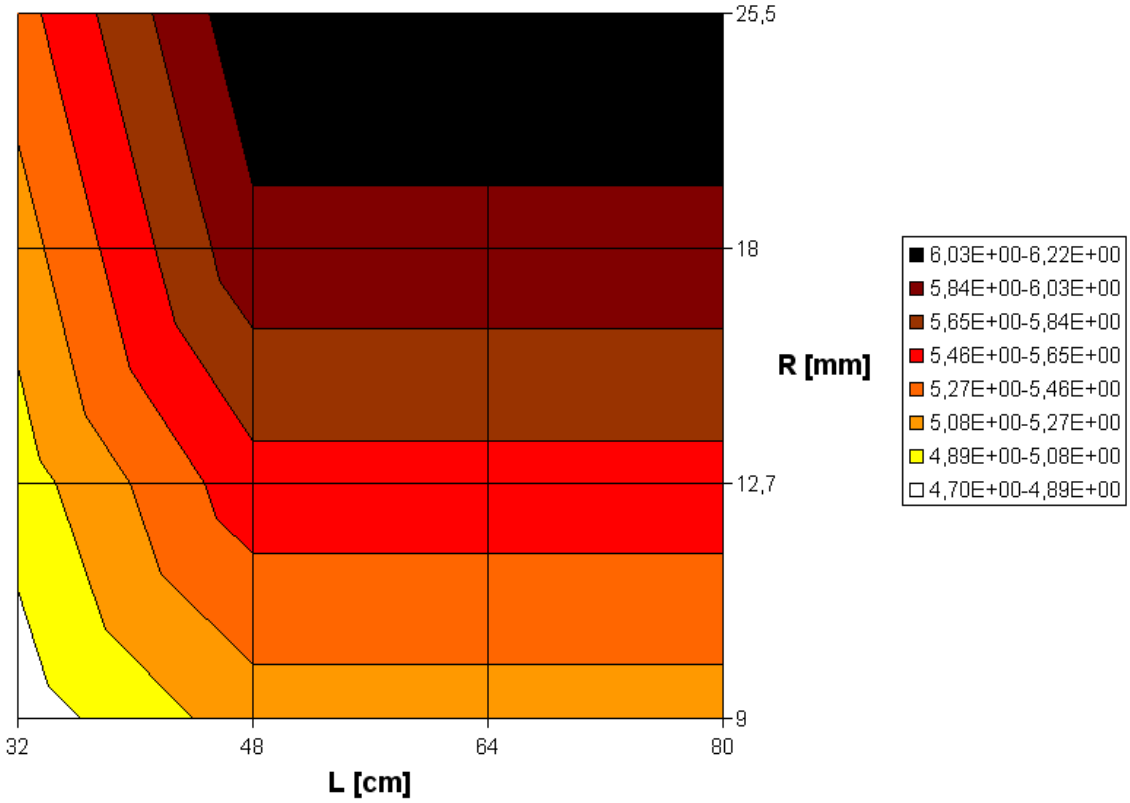

Figure 72: ^{17}Ne production rate per incident proton [10^{-6} s^{-1}] as a function of target radius *R* and length *L*, (target = SiC, *E* = 1 GeV, model = INCL4/ABLA, the low energetic secondary neutron flux is taken into account, CINDER evolution time = 1 ms).

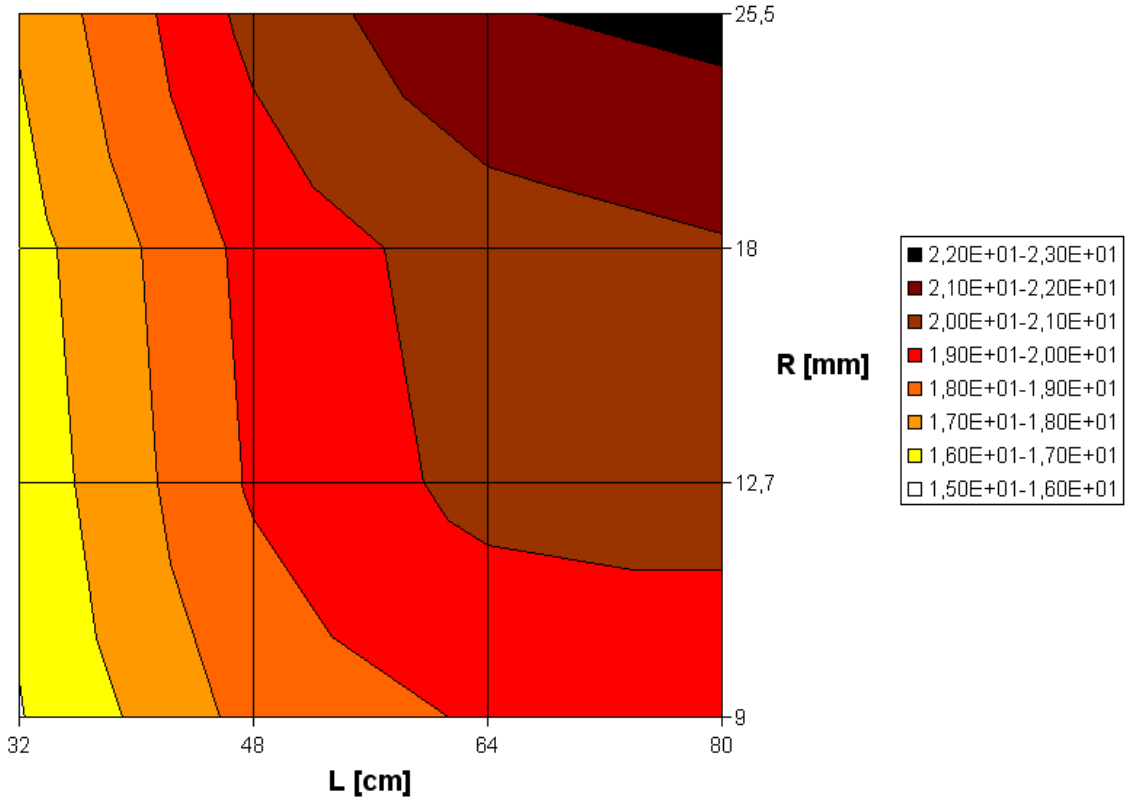

Figure 73: ^{17}Ne production rate per incident proton [10^{-6} s^{-1}] as a function of target radius *R* and length *L*, (target = SiC, *E* = 1 GeV, model = CEM2k, the low energetic secondary neutron flux is taken into account, CINDER evolution time = 1 ms).

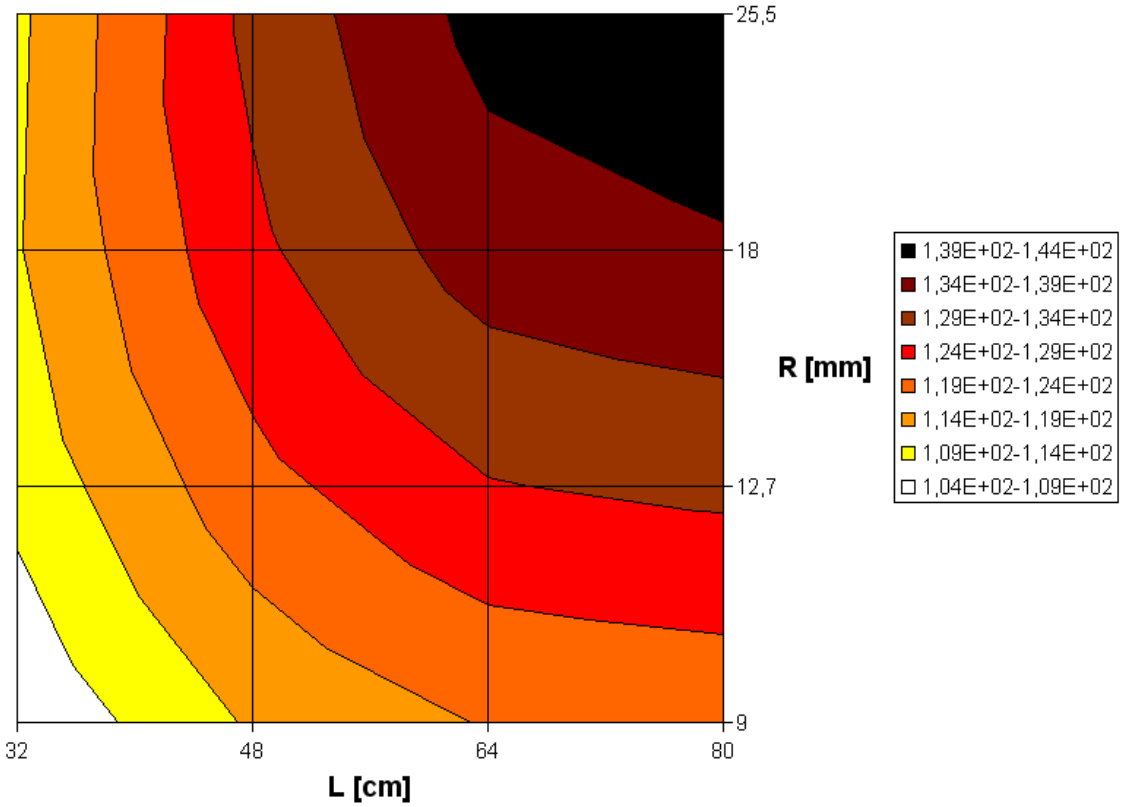

Figure 74: ^{18}Ne production rate per incident proton [10^{-6} s^{-1}] as a function of target radius *R* and length *L*, (target = SiC, *E* = 1 GeV, model = INCL4/ABLA, the low energetic secondary neutron flux is taken into account, CINDER evolution time = 1 ms).

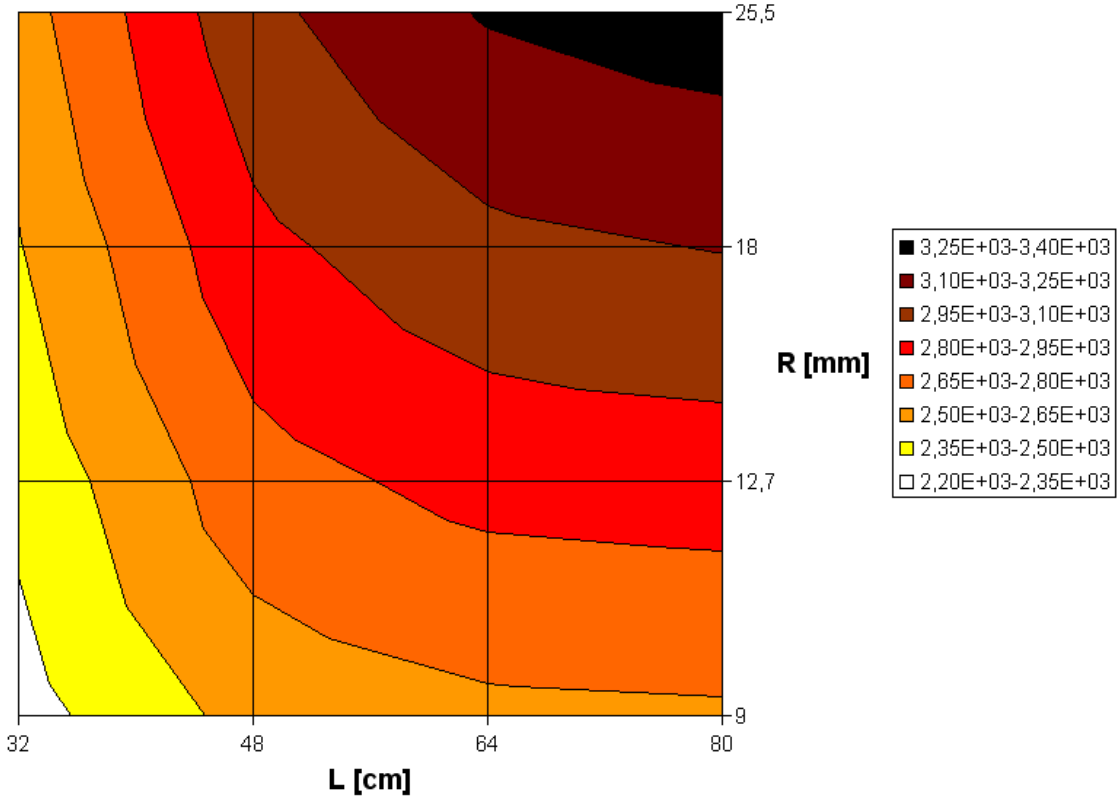

Figure 75: ^{18}Ne production rate per incident proton [10^{-6} s^{-1}] as a function of target radius *R* and length *L*, (target = SiC, *E* = 1 GeV, model = CEM2k, the low energetic secondary neutron flux is taken into account, CINDER evolution time = 1 ms).

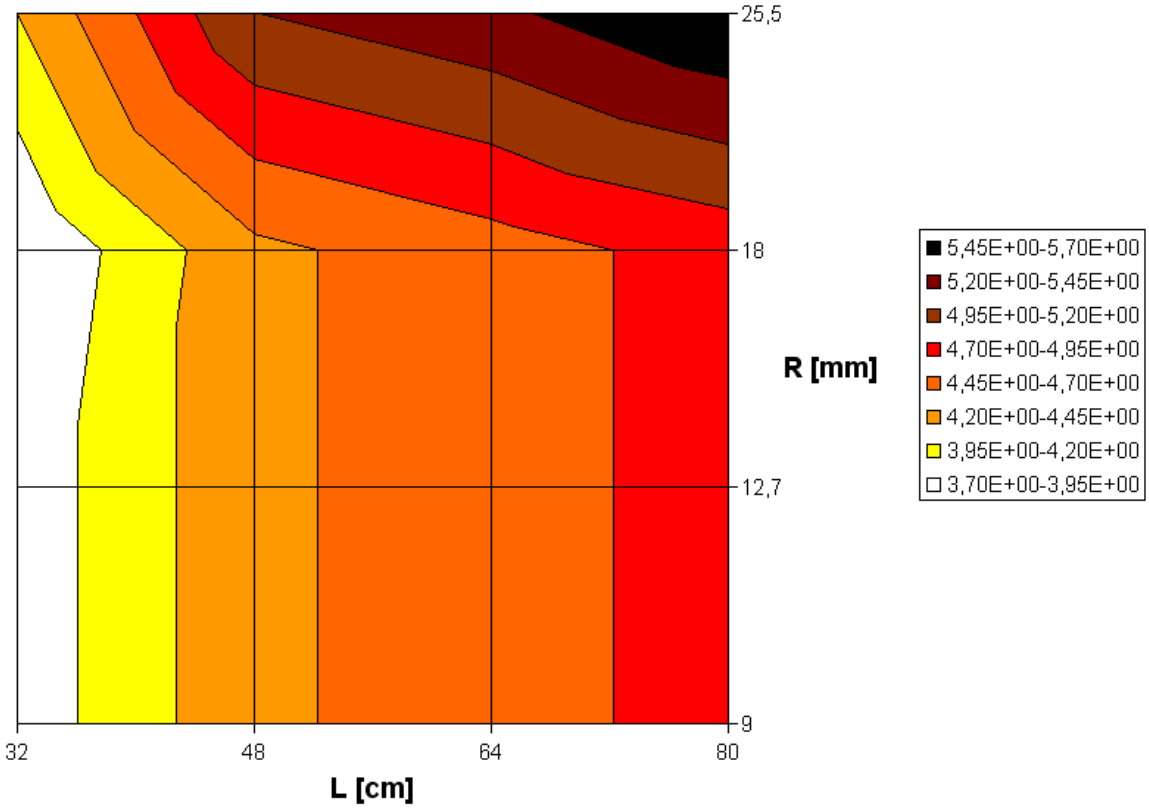

Figure 76: ^{25}Ne production rate per incident proton [10^{-6} s^{-1}] as a function of target radius *R* and length *L*, (target = SiC, *E* = 1 GeV, model = INCL4/ABLA, the low energetic secondary neutron flux is taken into account, CINDER evolution time = 1 ms).

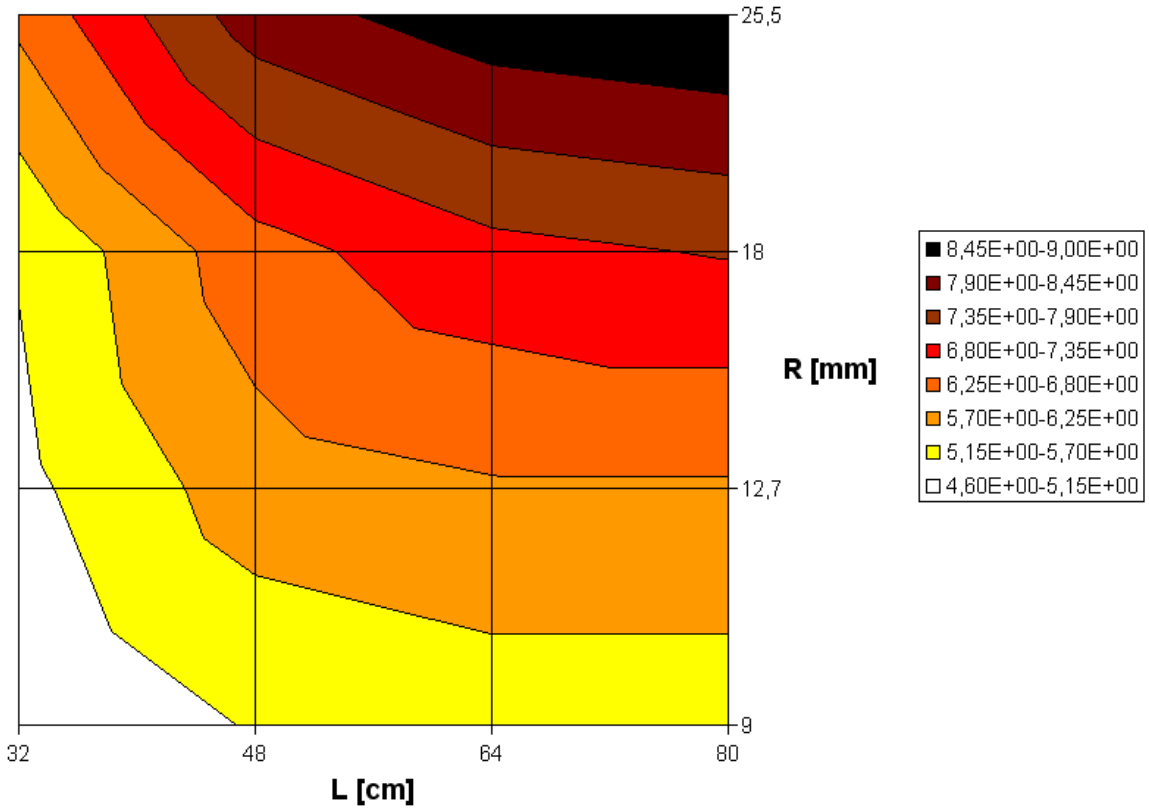

Figure 77: ^{25}Ne production rate per incident proton [10^{-6} s^{-1}] as a function of target radius *R* and length *L*, (target = SiC, *E* = 1 GeV, model = CEM2k, the low energetic secondary neutron flux is taken into account, CINDER evolution time = 1 ms).

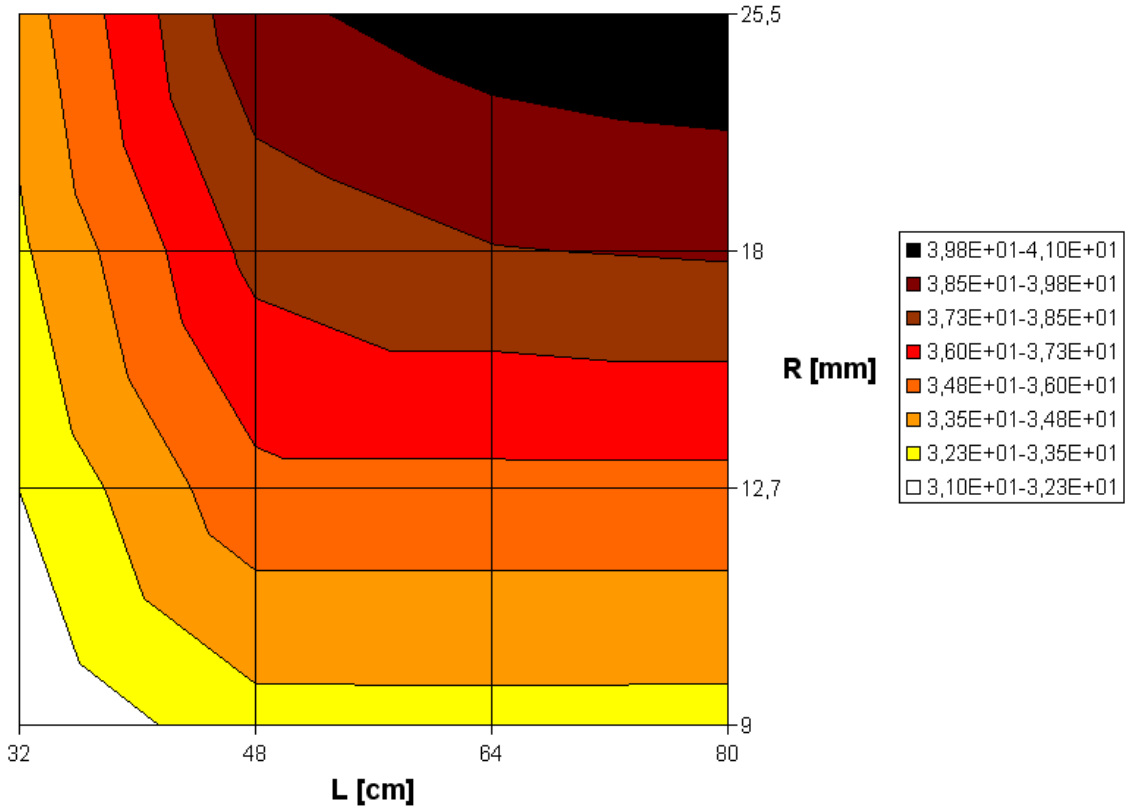

Figure 78: ^{20}Mg production rate per incident proton [10^{-6} s^{-1}] as a function of target radius *R* and length *L*, (target = SiC, *E* = 1 GeV, model = INCL4/ABLA, the low energetic secondary neutron flux is taken into account, CINDER evolution time = 1 ms).

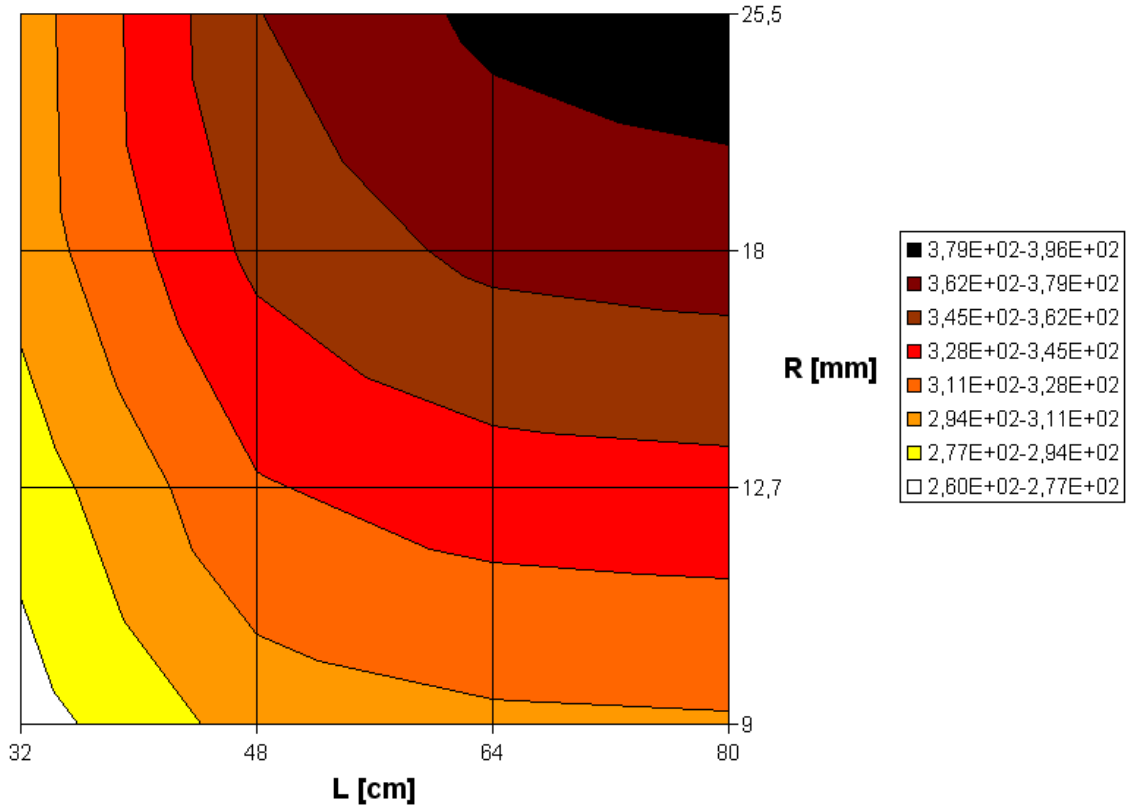

Figure 79: ^{20}Mg production rate per incident proton [10^{-6} s^{-1}] as a function of target radius *R* and length *L*, (target = SiC, *E* = 1 GeV, model = CEM2k, the low energetic secondary neutron flux is taken into account, CINDER evolution time = 1 ms).

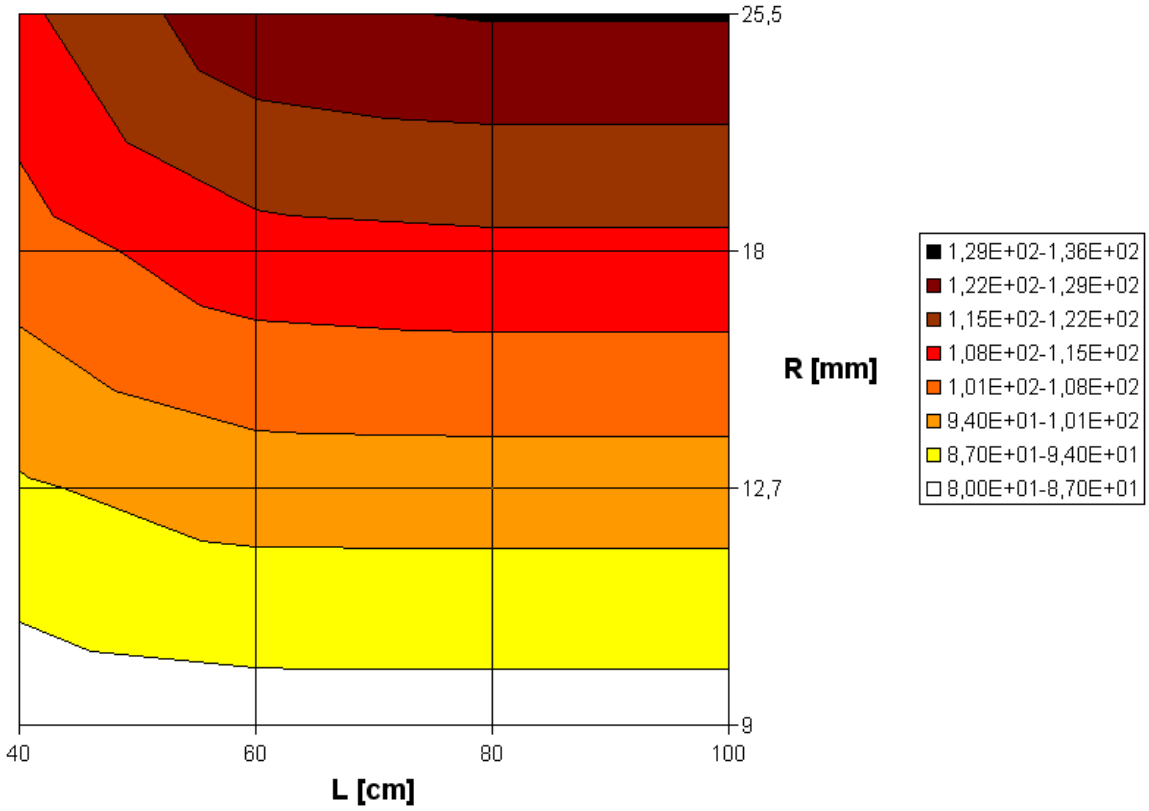

Figure 80: ^{72}Ni production rate per incident proton [10^{-6} s^{-1}] as a function of target radius *R* and length *L*, (target = UC_3, *E* = 1 GeV, model = INCL4/ABLA, the low energetic secondary neutron flux is taken into account, CINDER evolution time = 1 ms).

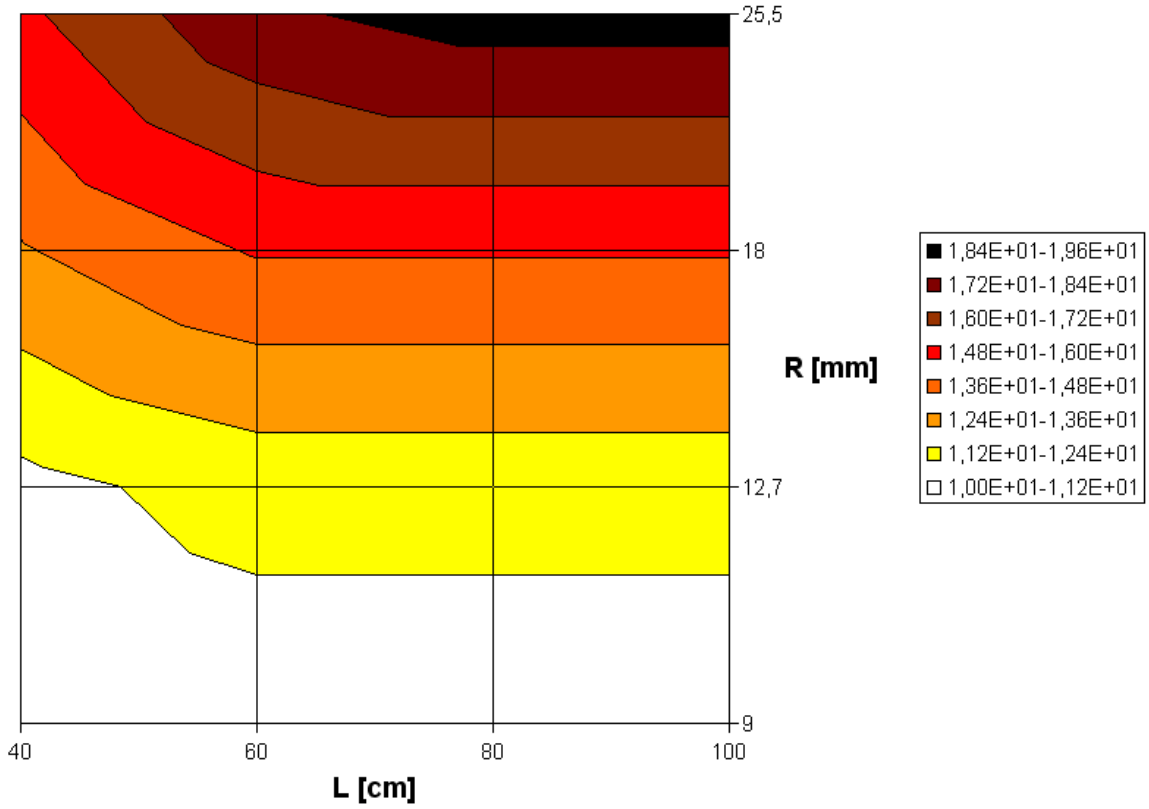

Figure 81: ^{72}Ni production rate per incident proton [10^{-6} s^{-1}] as a function of target radius *R* and length *L*, (target = UC_3, *E* = 1 GeV, model = CEM2k, the low energetic secondary neutron flux is taken into account, CINDER evolution time = 1 ms).

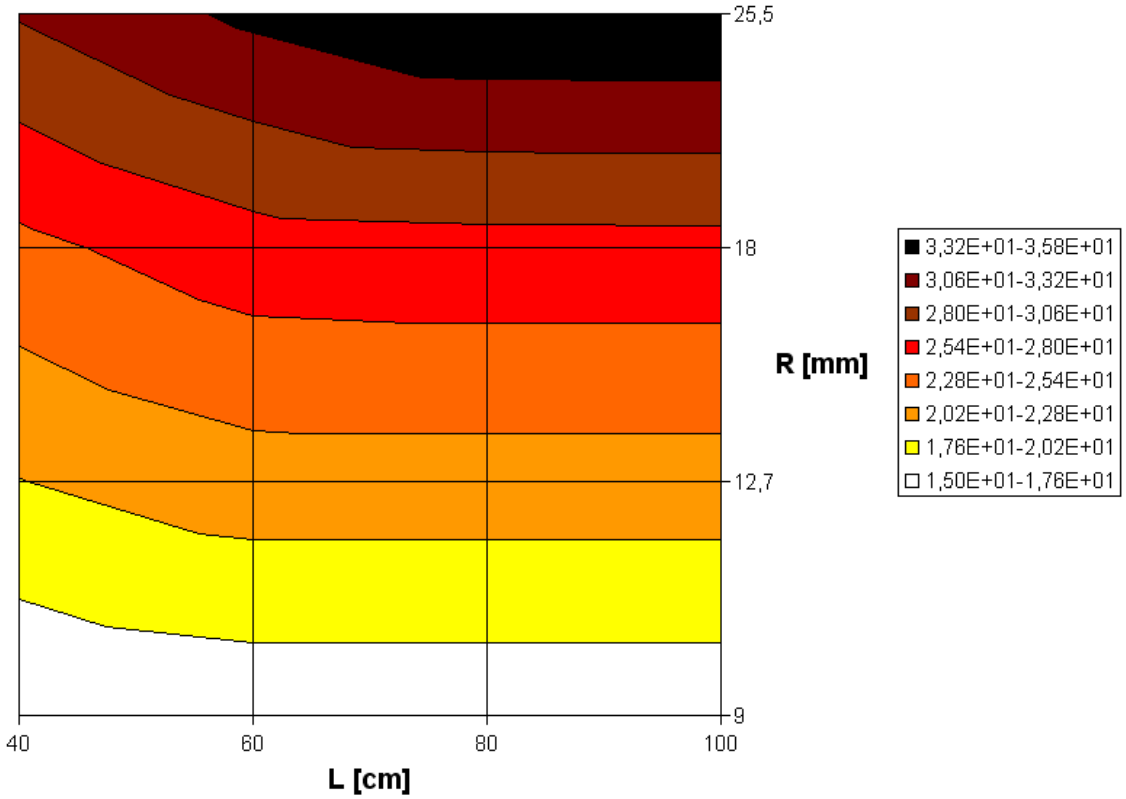

Figure 82: ^{81}Ga production rate per incident proton [10^{-6} s^{-1}] as a function of target radius *R* and length *L*, (target = UC_3, *E* = 0.5 GeV, model = INCL4/ABLA, the low energetic secondary neutron flux is taken into account, CINDER evolution time = 1 ms).

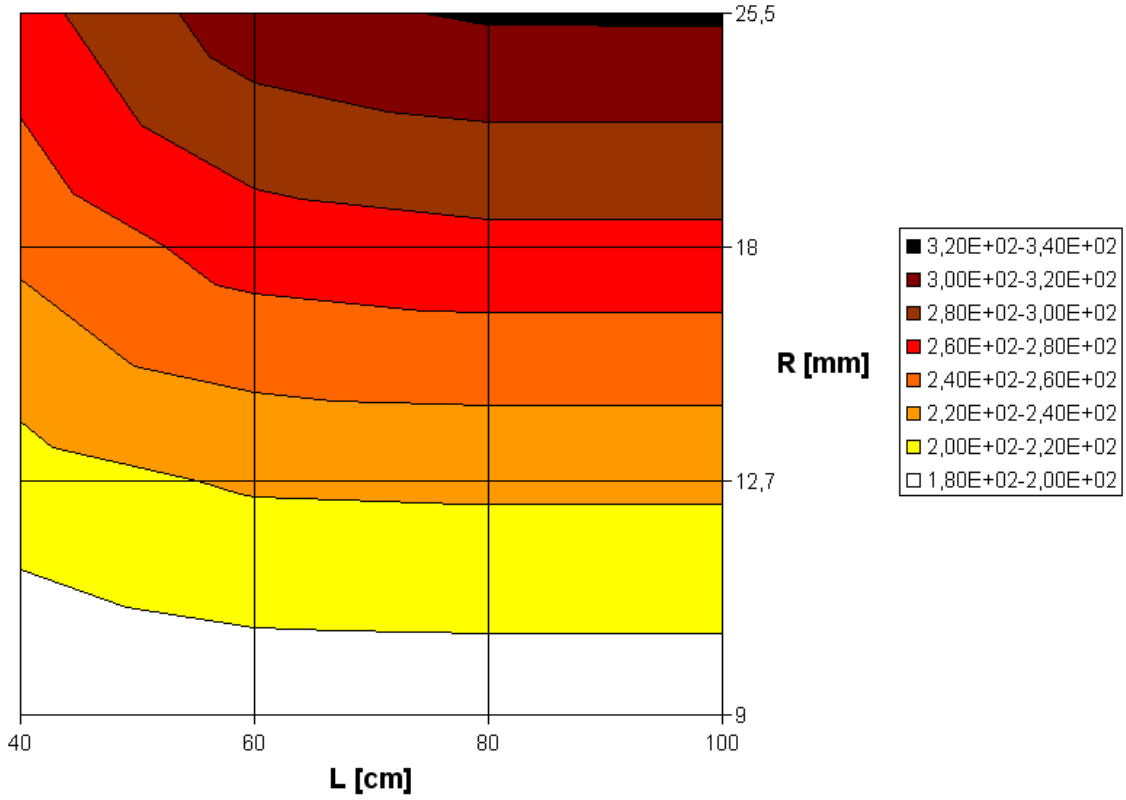

Figure 83: ^{81}Ga production rate per incident proton [10^{-6} s^{-1}] as a function of target radius *R* and length *L*, (target = UC_3, *E* = 0.5 GeV, model = CEM2k, the low energetic secondary neutron flux is taken into account, CINDER evolution time = 1 ms).

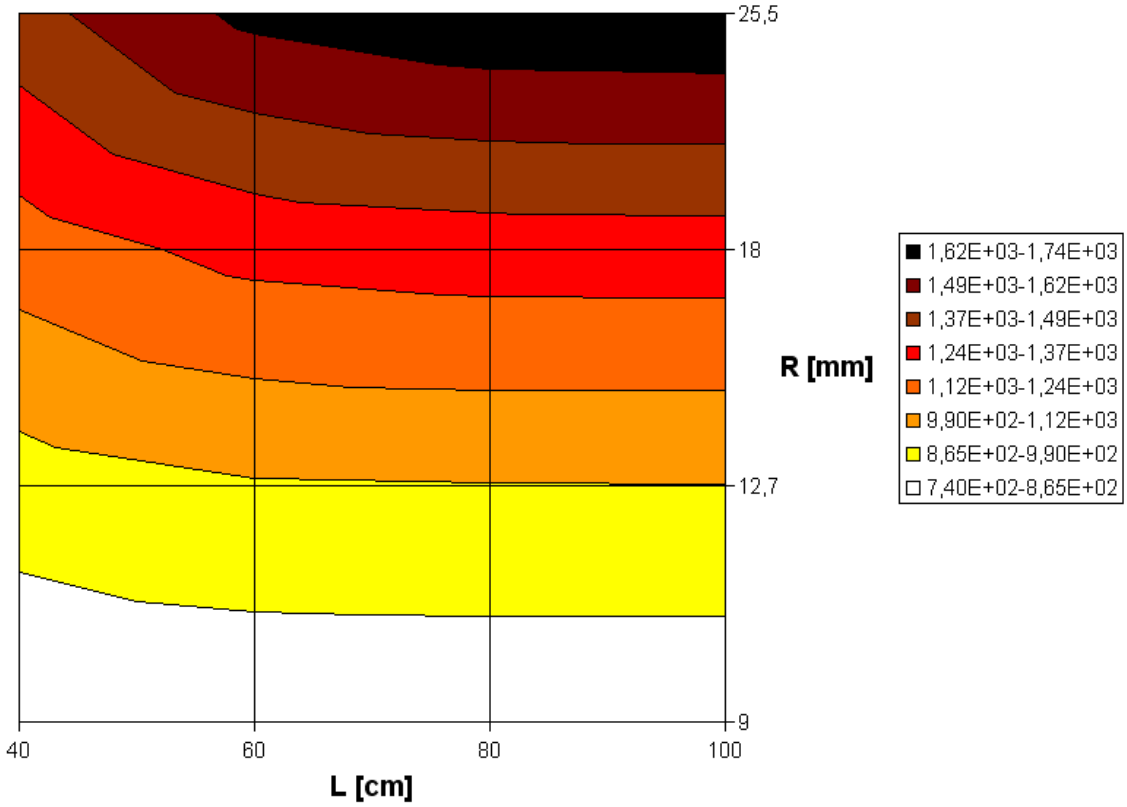

Figure 84: ^{92}Kr production rate per incident proton [10^{-6} s^{-1}] as a function of target radius *R* and length *L*, (target = UC_3, *E* = 0.5 GeV, model = INCL4/ABLA, the low energetic secondary neutron flux is taken into account, CINDER evolution time = 1 ms).

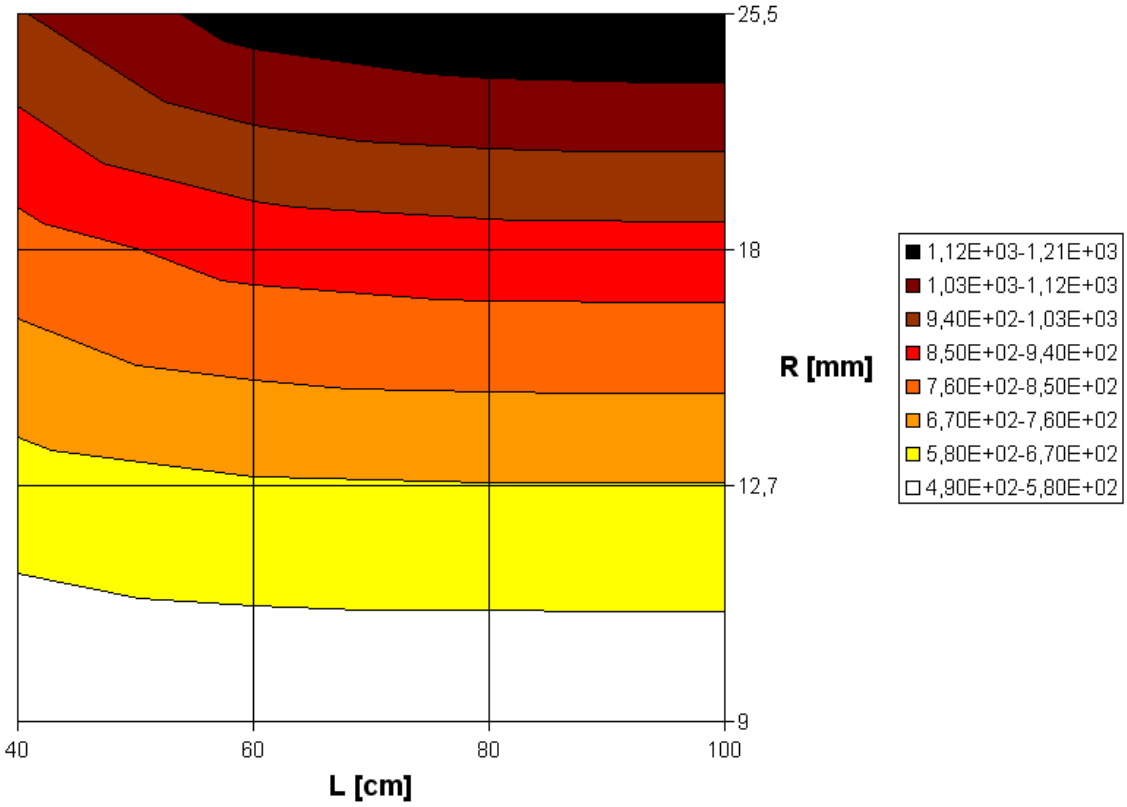

Figure 85: ^{92}Kr production rate per incident proton [10^{-6} s^{-1}] as a function of target radius *R* and length *L*, (target = UC_3, *E* = 0.5 GeV, model = CEM2k, the low energetic secondary neutron flux is taken into account, CINDER evolution time = 1 ms).

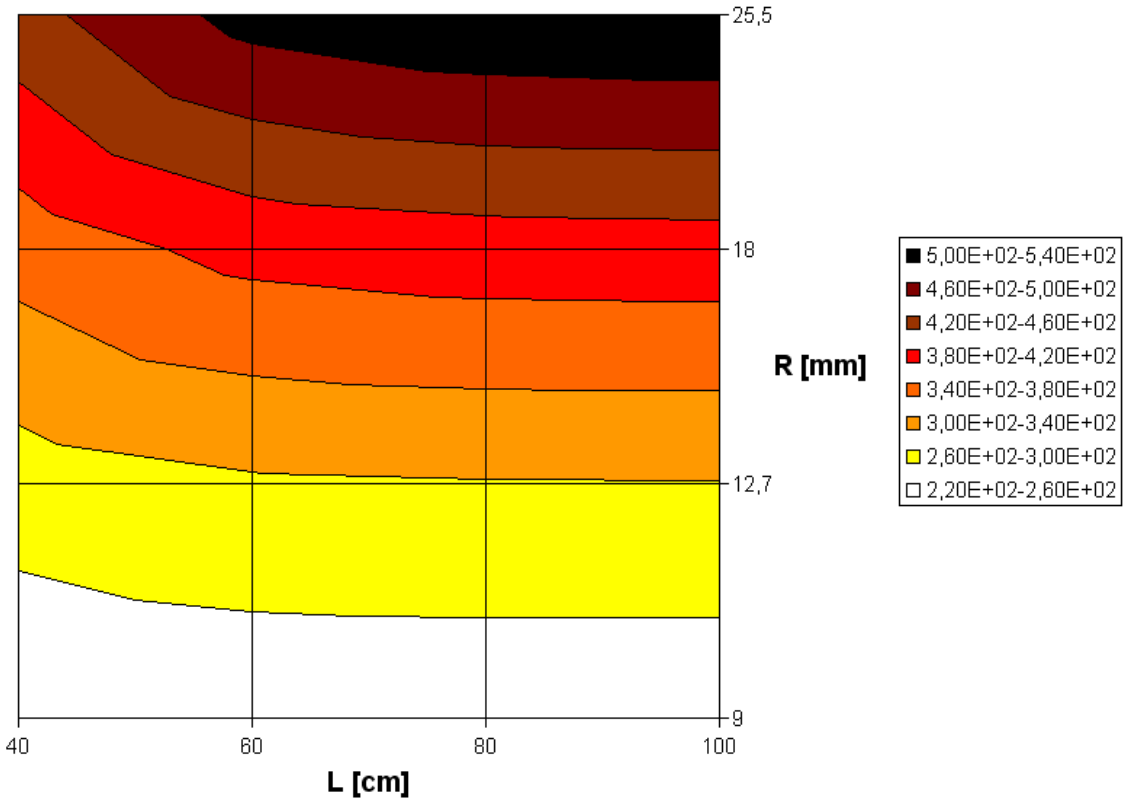

Figure 86: ^{132}Sn production rate per incident proton [10^{-6} s^{-1}] as a function of target radius *R* and length *L*, (target = UC_3, *E* = 0.5 GeV, model = INCL4/ABLA, the low energetic secondary neutron flux is taken into account, CINDER evolution time = 1 ms).

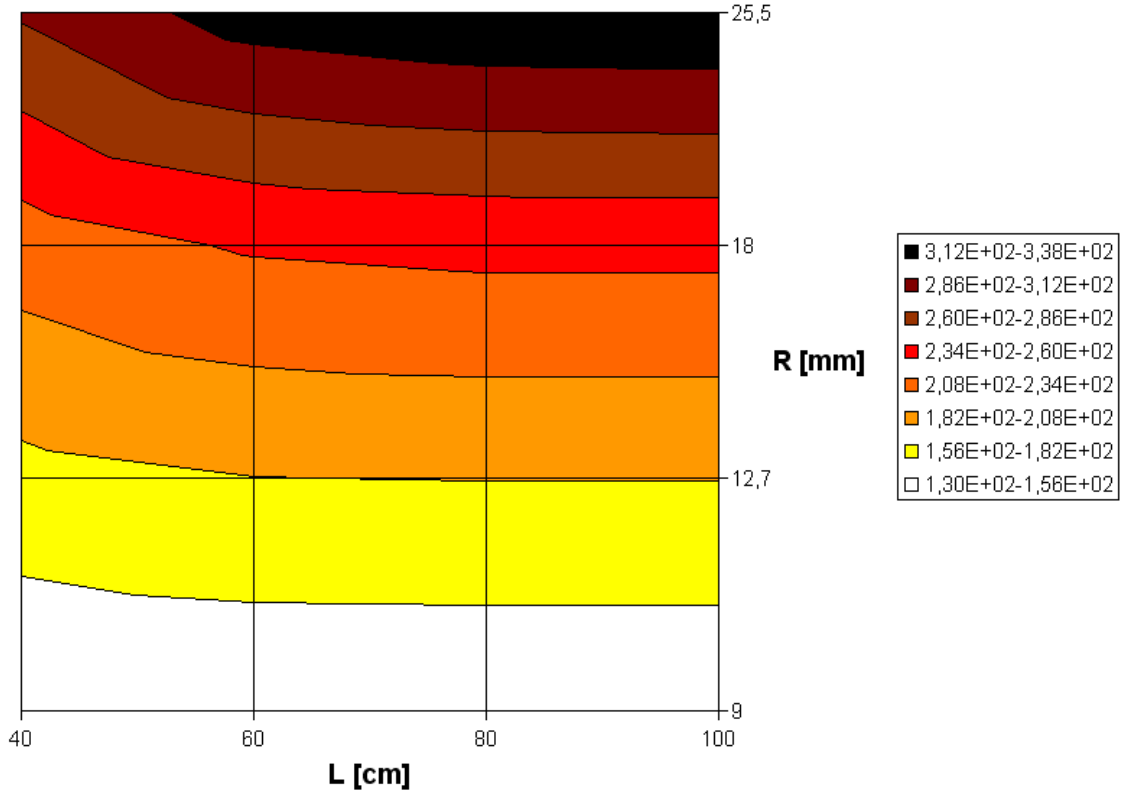

Figure 87: ^{132}Sn production rate per incident proton [10^{-6} s^{-1}] as a function of target radius *R* and length *L*, (target = UC_3, *E* = 0.5 GeV, model = CEM2k, the low energetic secondary neutron flux is taken into account, CINDER evolution time = 1 ms).

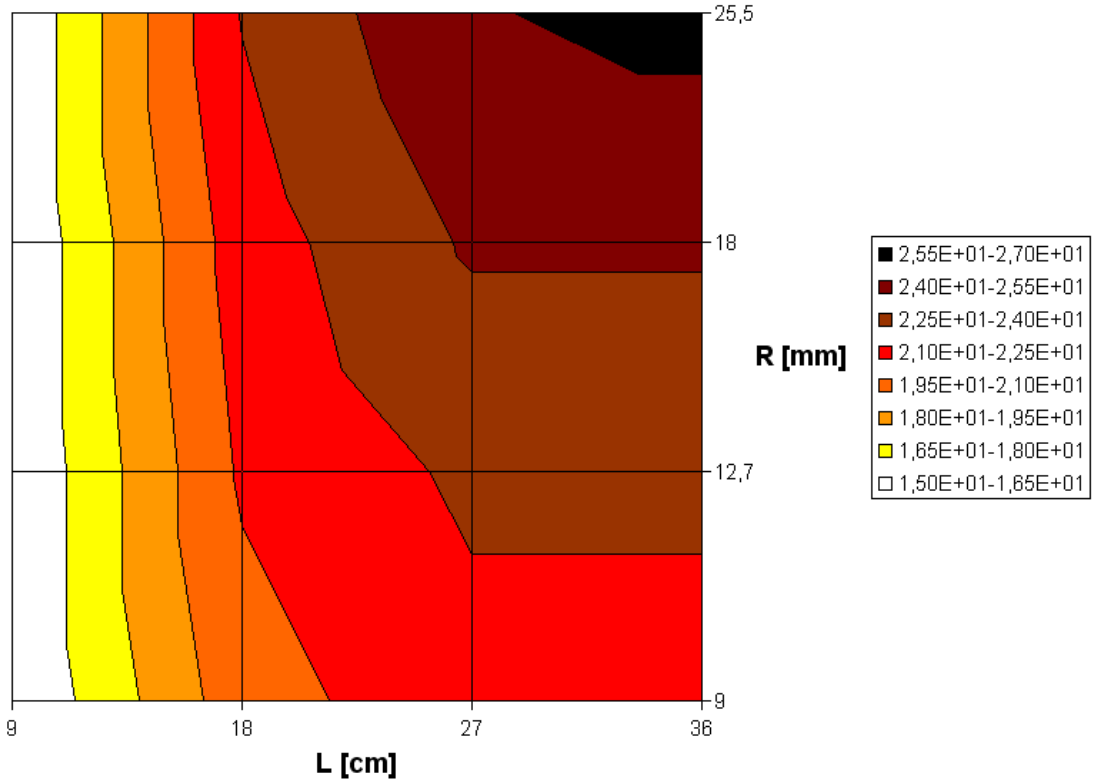

Figure 88: ^{180}Hg production rate per incident proton [10^{-6} s^{-1}] as a function of target radius *R* and length *L*, (target = Pb, *E* = 1 GeV, model = INCL4/ABLA, the low energetic secondary neutron flux is taken into account, CINDER evolution time = 1 ms).

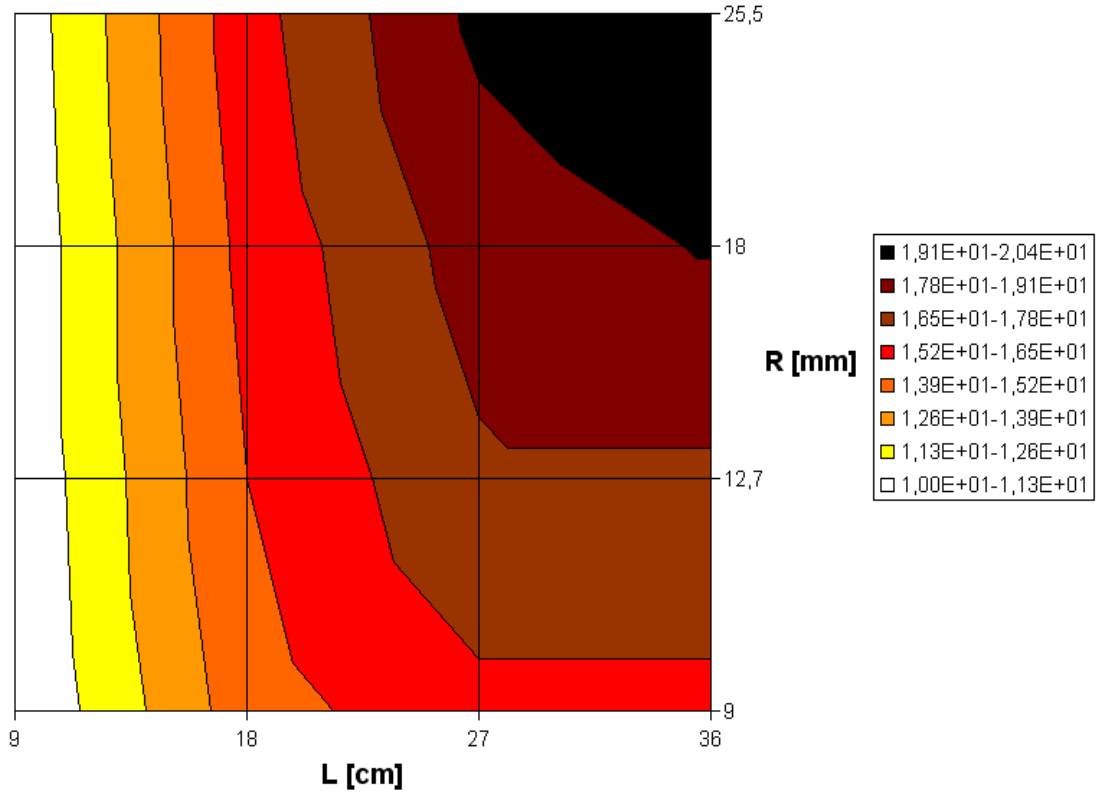

Figure 89: ^{180}Hg production rate per incident proton [10^{-6} s^{-1}] as a function of target radius *R* and length *L*, (target = Pb, *E* = 1 GeV, model = CEM2k, the low energetic secondary neutron flux is taken into account, CINDER evolution time = 1 ms).

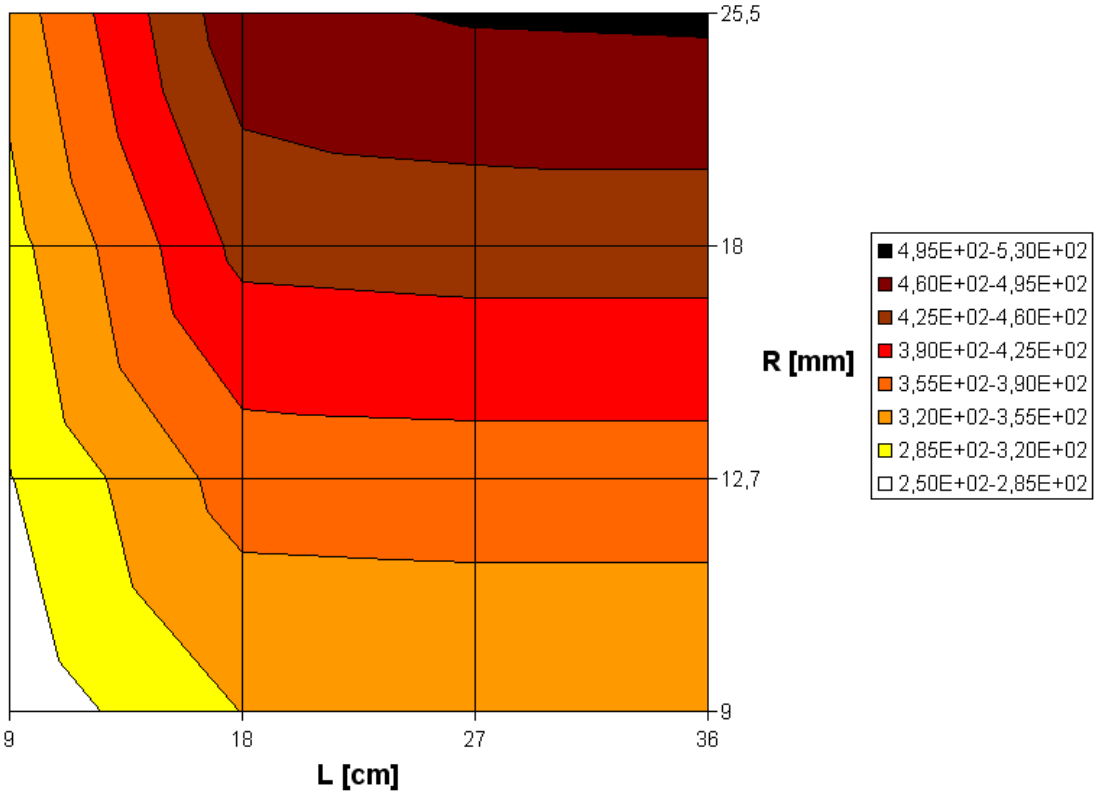

Figure 90: ^{206}Hg production rate per incident proton [10^{-6} s^{-1}] as a function of target radius *R* and length *L*, (target = Pb, *E* = 0.5 GeV, model = INCL4/ABLA, the low energetic secondary neutron flux is taken into account, CINDER evolution time = 1 ms).

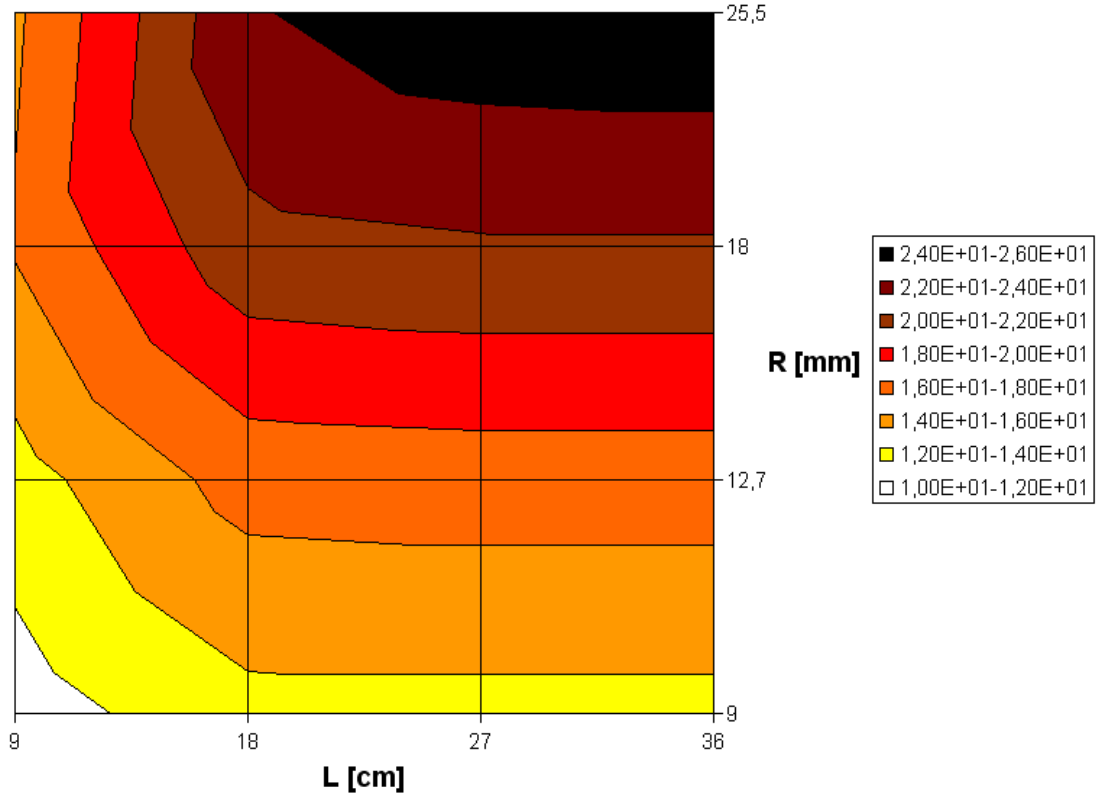

Figure 91: ^{206}Hg production rate per incident proton [10^{-6} s^{-1}] as a function of target radius *R* and length *L*, (target = Pb, *E* = 0.5 GeV, model = CEM2k, the low energetic secondary neutron flux is taken into account, CINDER evolution time = 1 ms).

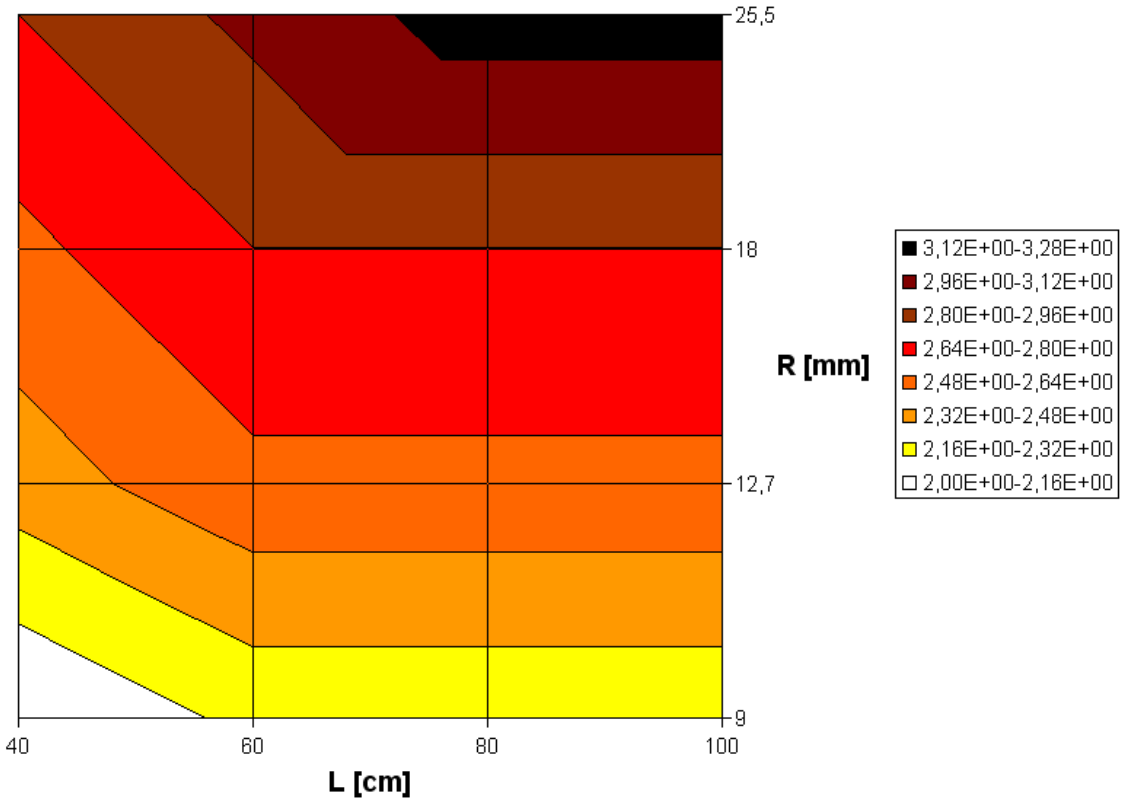

Figure 92: ^{205}Fr production rate per incident proton [10^{-6} s^{-1}] as a function of target radius *R* and length *L*, (target = UC_3, *E* = 1 GeV, model = INCL4/ABLA, the low energetic secondary neutron flux is taken into account, CINDER evolution time = 1 ms).

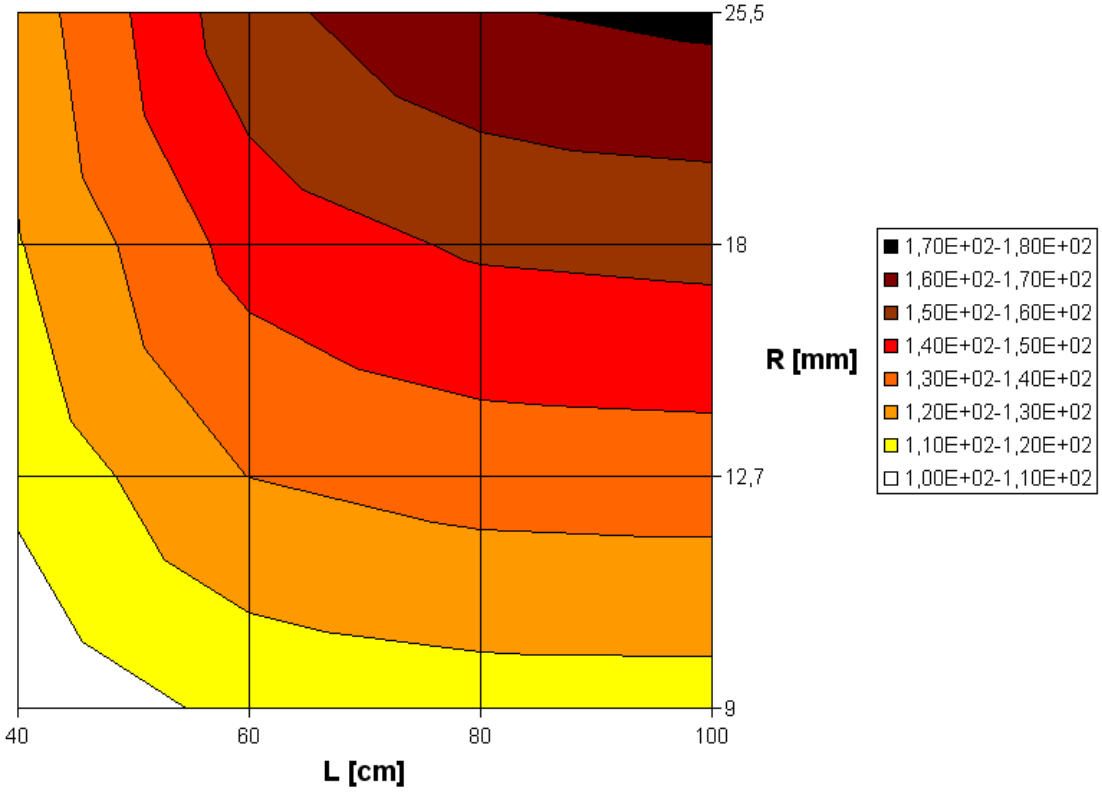

Figure 93: ^{205}Fr production rate per incident proton [10^{-6} s^{-1}] as a function of target radius *R* and length *L*, (target = UC_3, *E* = 1 GeV, model = CEM2k, the low energetic secondary neutron flux is taken into account, CINDER evolution time = 1 ms).

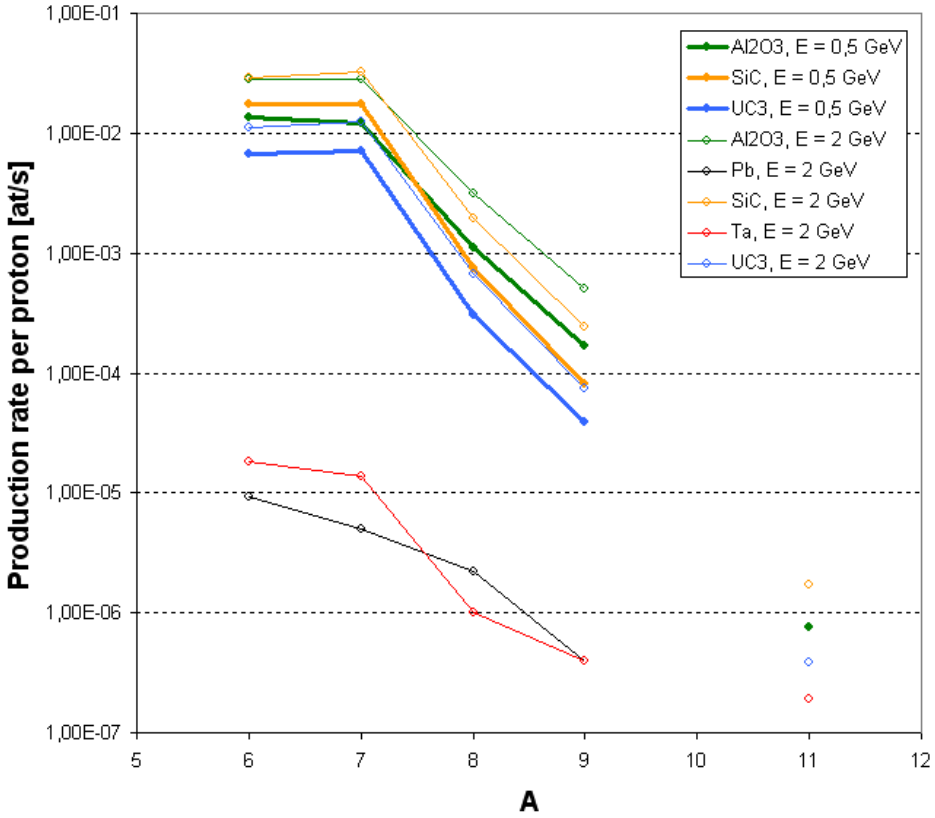

Figure 94: Li isotopic distribution (R = 18 mm, M = 2 kg, spallation model = INCL4/ABLA, the low energetic secondary neutron flux contribution is taken into account, CINDER evolution time = 1 ms).

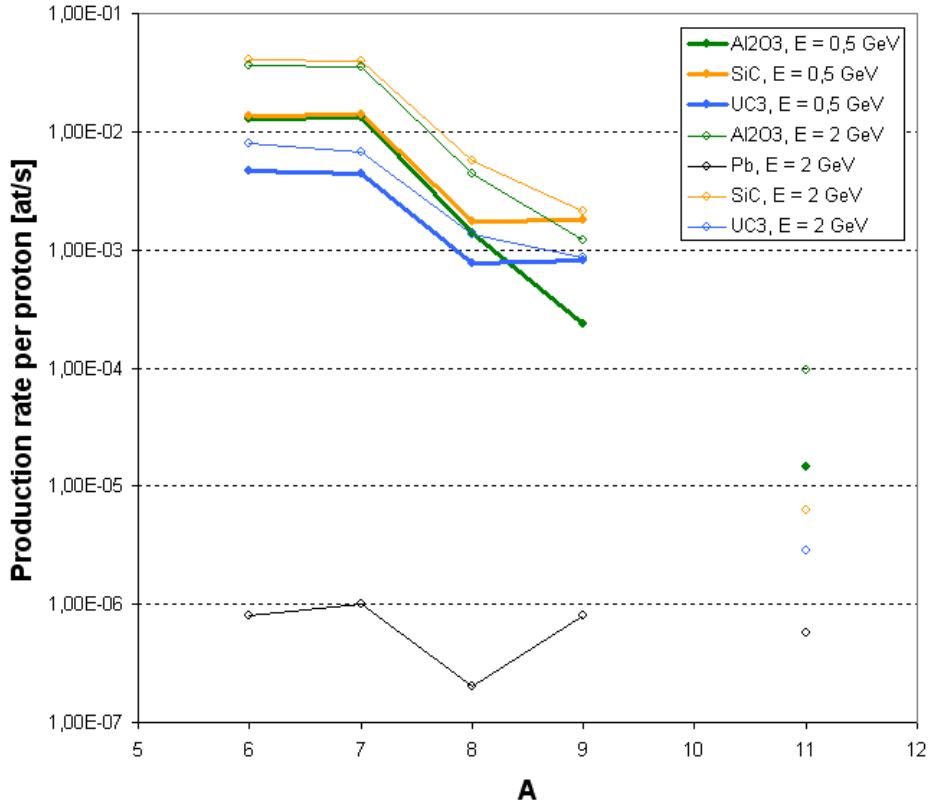

Figure 95: Li isotopic distribution (R = 18 mm, M = 2 kg, spallation model = CEM2k, the low energetic secondary neutron flux contribution is taken into account, CINDER evolution time = 1 ms).

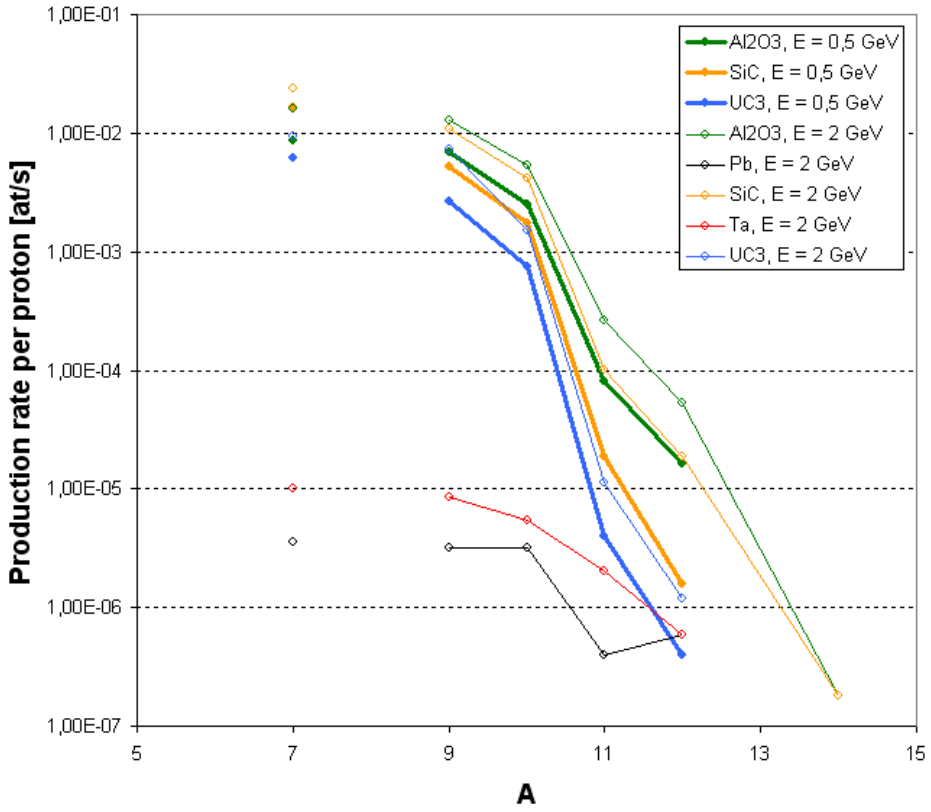

Figure 96: Be isotopic distribution (R = 18 mm, M = 2 kg, spallation model = INCL4/ABLA, the low energetic secondary neutron flux contribution is taken into account, CINDER evolution time = 1 ms).

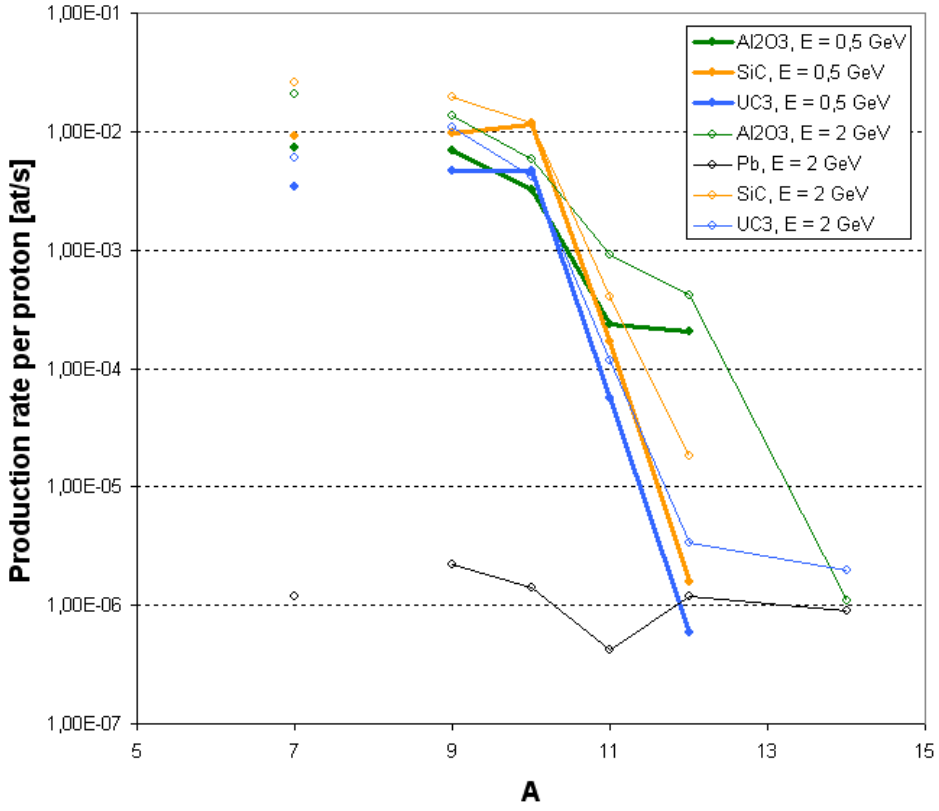

Figure 97: Be isotopic distribution (R = 18 mm, M = 2 kg, spallation model = CEM2k, the low energetic secondary neutron flux contribution is taken into account, CINDER evolution time = 1 ms).

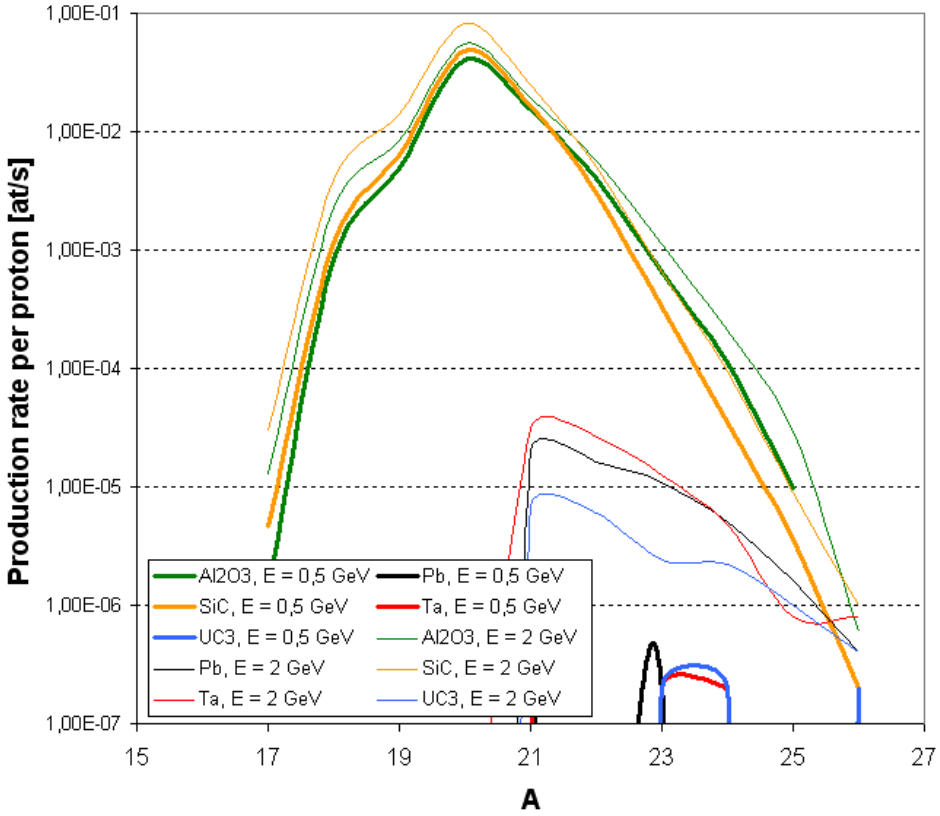

Figure 98: Ne isotopic distribution (R = 18 mm, M = 2 kg, spallation model = INCL4/ABLA, the low energetic secondary neutron flux contribution is taken into account, CINDER evolution time = 1 ms).

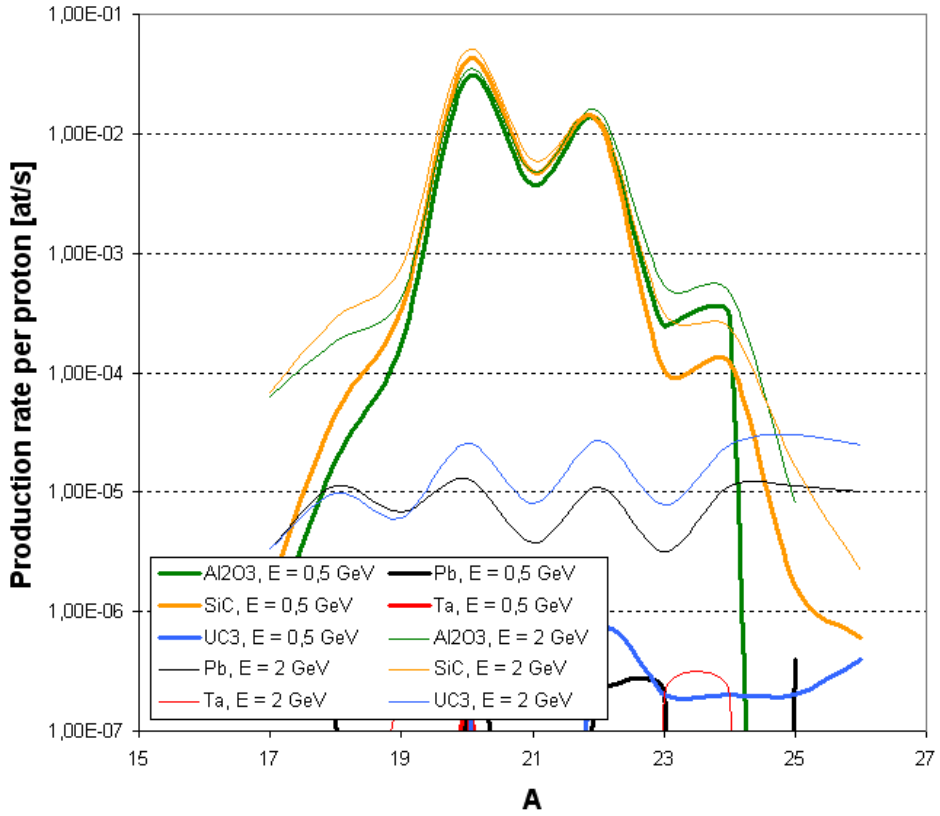

Figure 99: Ne isotopic distribution (R = 18 mm, M = 2 kg, spallation model = CEM2k, the low energetic secondary neutron flux contribution is taken into account, CINDER evolution time = 1 ms).

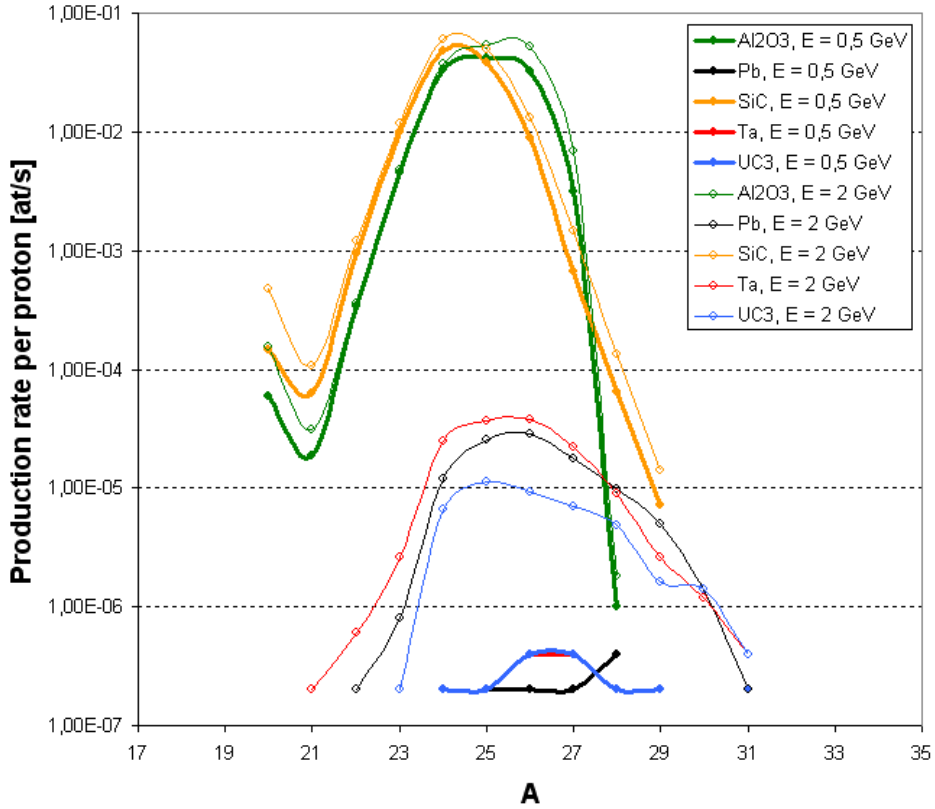

Figure 100: Mg isotopic distribution (R = 18 mm, M = 2 kg, spallation model = INCL4/ABLA, the low energetic secondary neutron flux contribution is taken into account, CINDER evolution time = 1 ms).

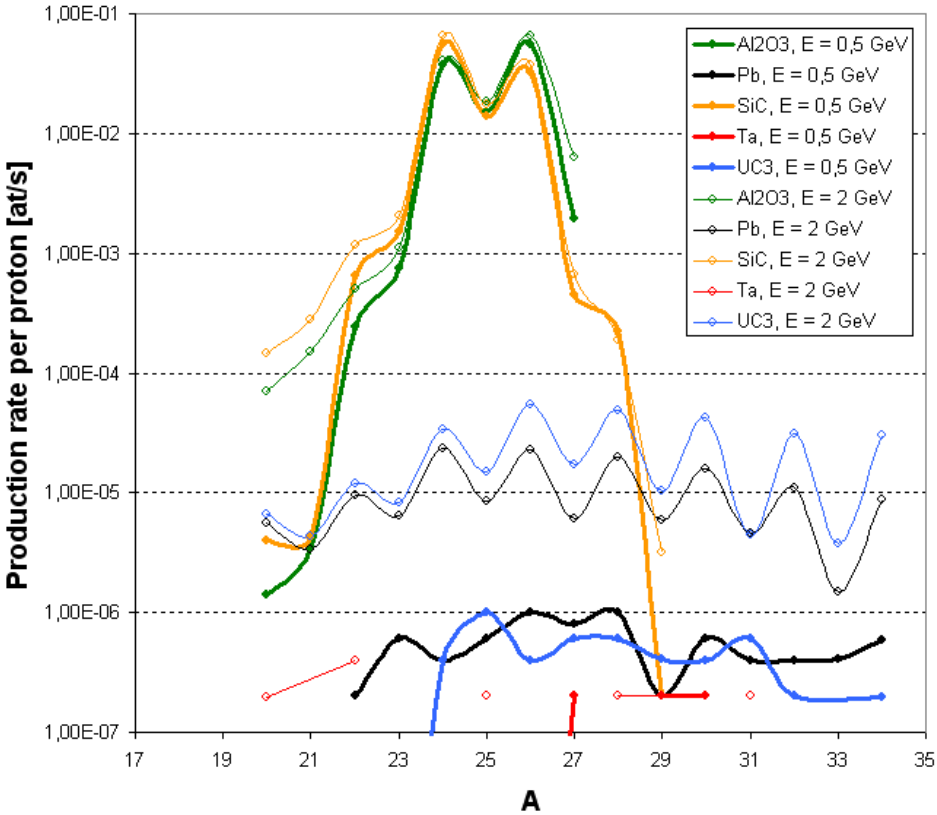

Figure 101: Mg isotopic distribution (R = 18 mm, M = 2 kg, spallation model = CEM2k, the low energetic secondary neutron flux contribution is taken into account, CINDER evolution time = 1 ms).

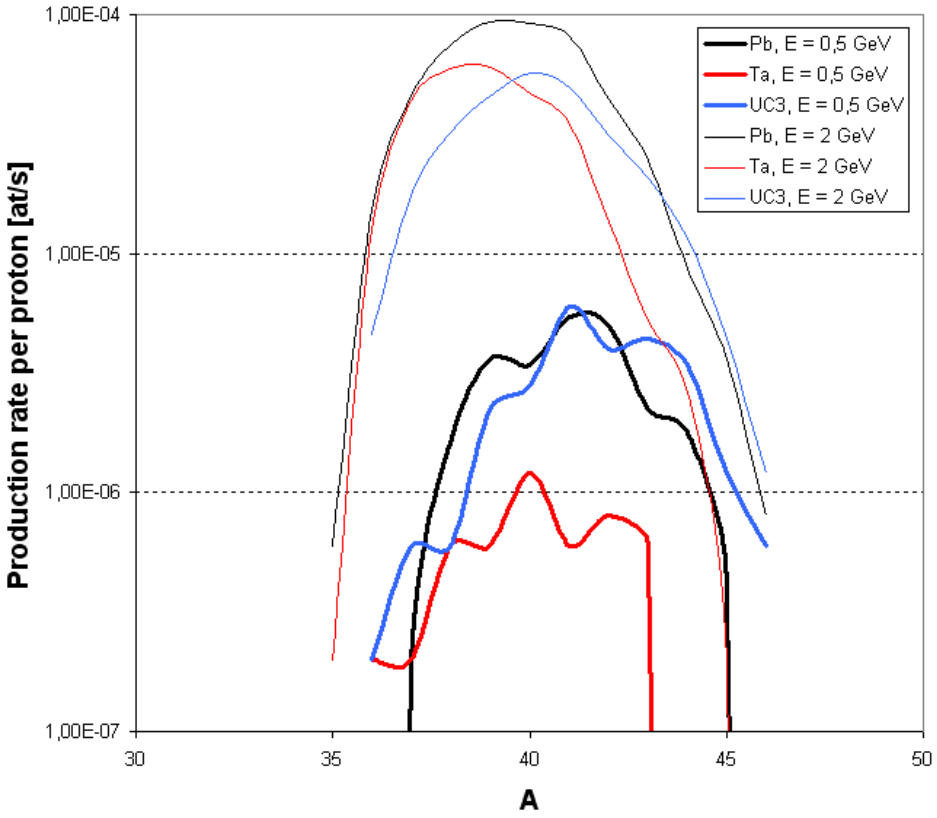

Figure 102: Ar isotopic distribution (R = 18 mm, M = 2 kg, spallation model = INCL4/ABLA, the low energetic secondary neutron flux contribution is taken into account, CINDER evolution time = 1 ms).

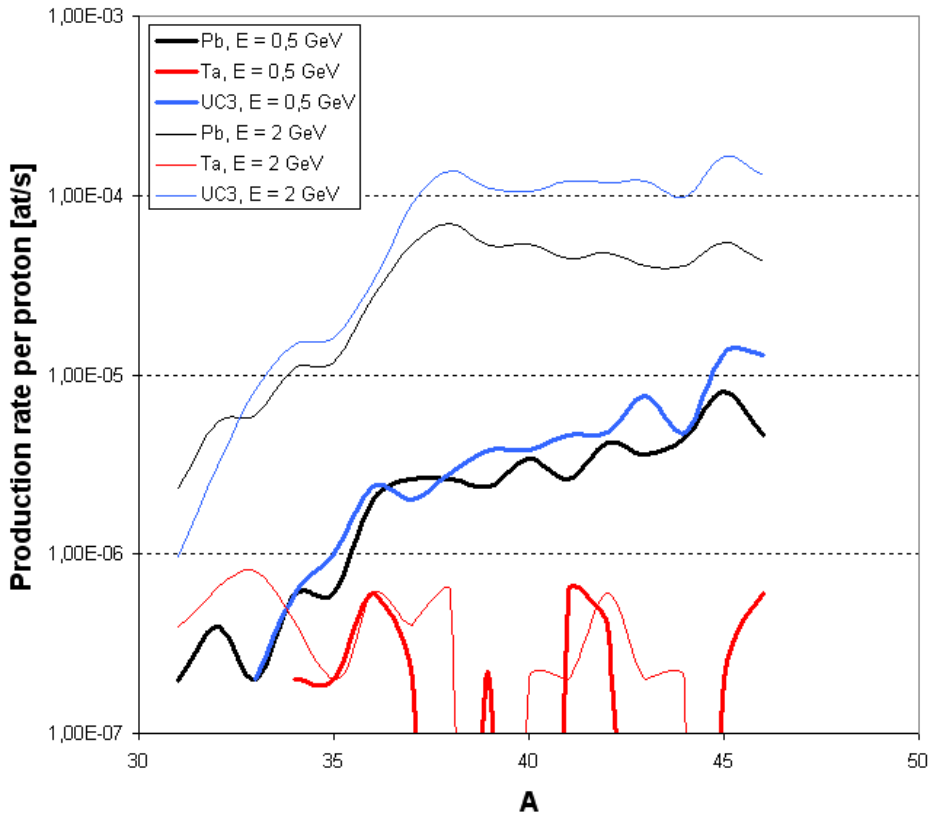

Figure 103: Ar isotopic distribution (R = 18 mm, M = 2 kg, spallation model = CEM2k, the low energetic secondary neutron flux contribution is taken into account, CINDER evolution time = 1 ms).

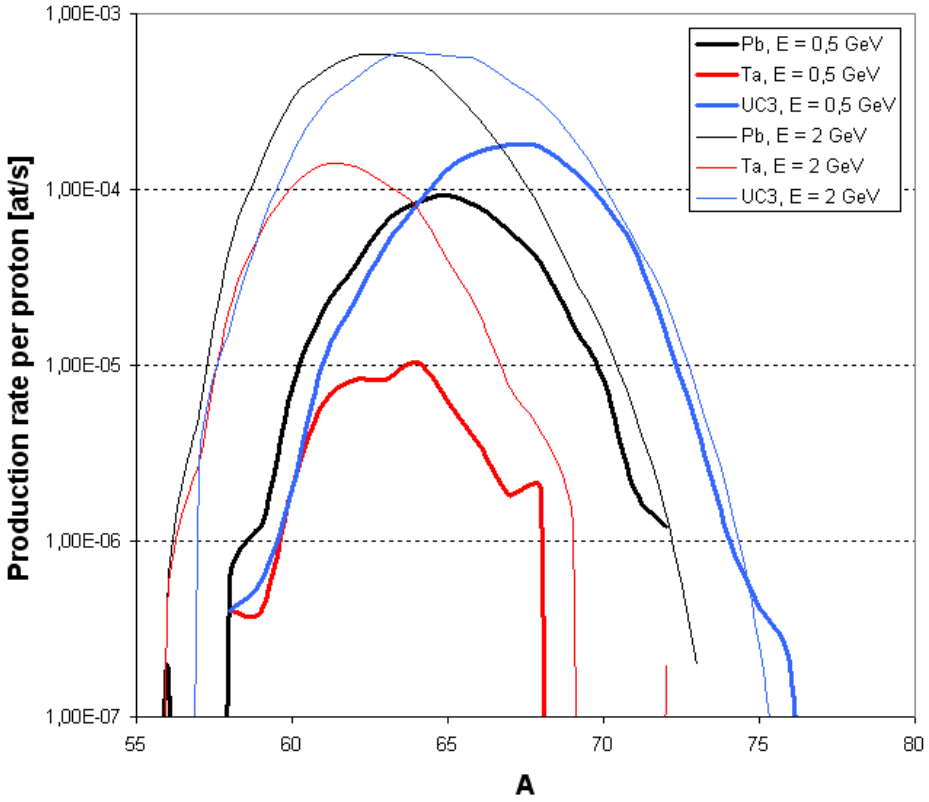

Figure 104: Ni isotopic distribution (R = 18 mm, M = 2 kg, spallation model = INCL4/ABLA, the low energetic secondary neutron flux contribution is taken into account, CINDER evolution time = 1 ms).

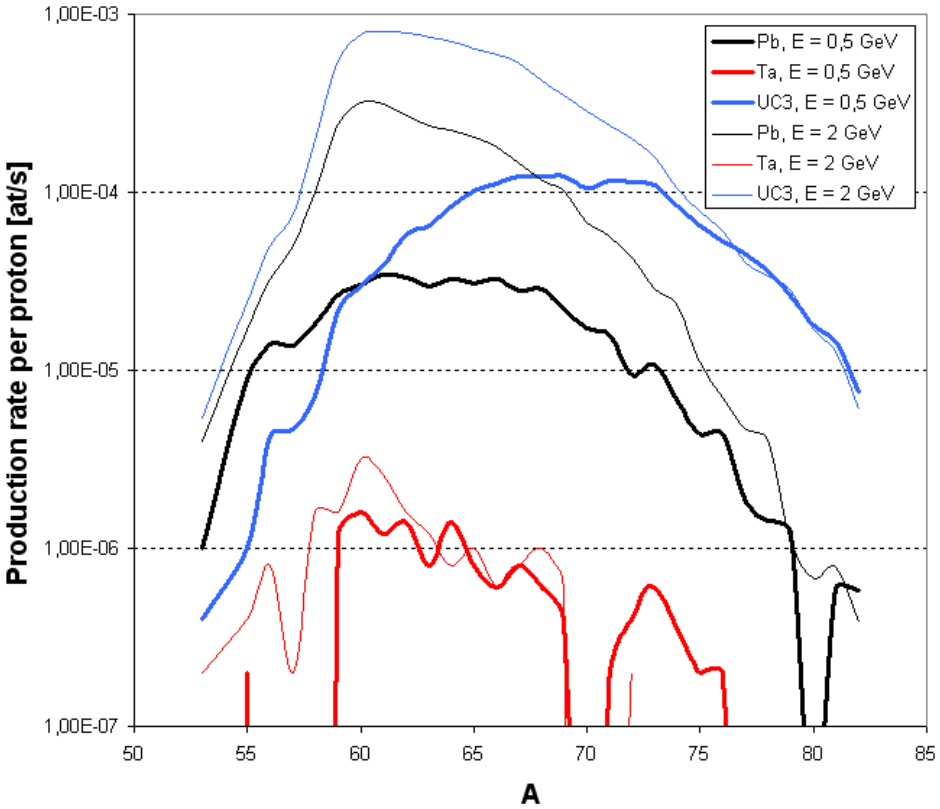

Figure 105: Ni isotopic distribution (R = 18 mm, M = 2 kg, spallation model = CEM2k, the low energetic secondary neutron flux contribution is taken into account, CINDER evolution time = 1 ms).

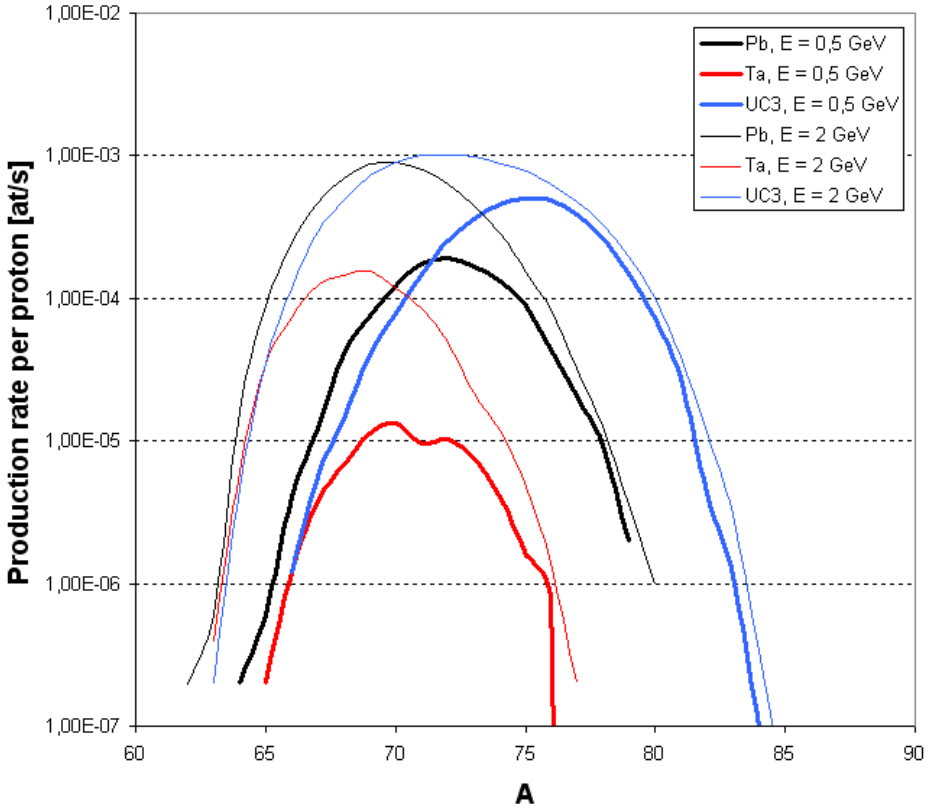

Figure 106: Ga isotopic distribution (R = 18 mm, M = 2 kg, spallation model = INCL4/ABLA, the low energetic secondary neutron flux contribution is taken into account, CINDER evolution time = 1 ms).

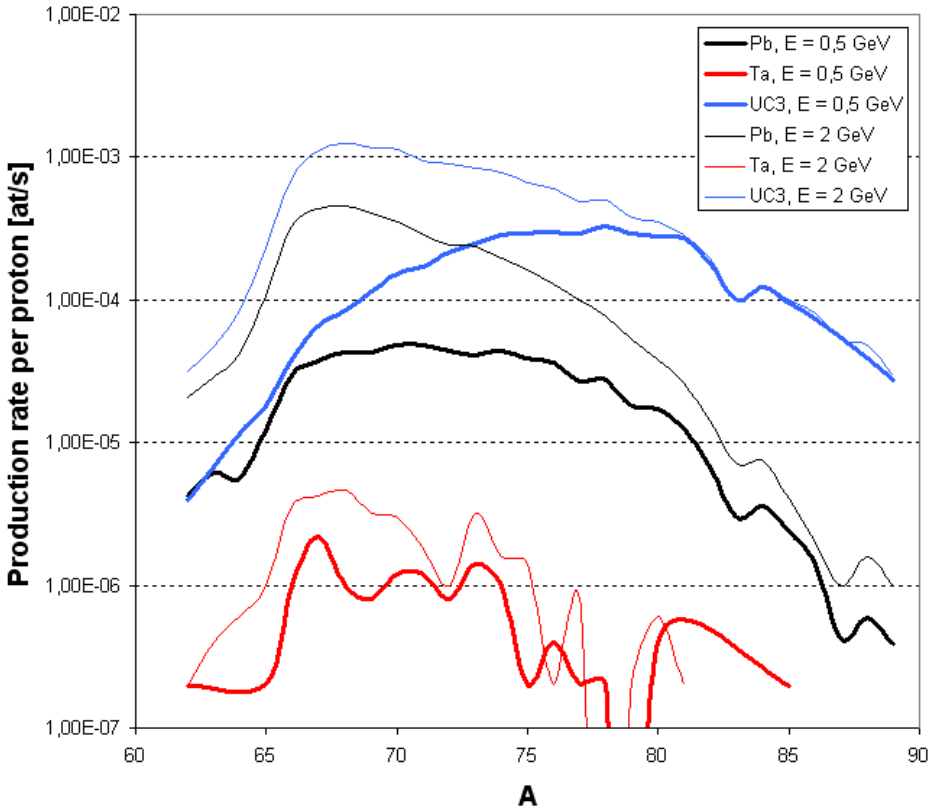

Figure 107: Ga isotopic distribution (R = 18 mm, M = 2 kg, spallation model = CEM2k, the low energetic secondary neutron flux contribution is taken into account, CINDER evolution time = 1 ms).

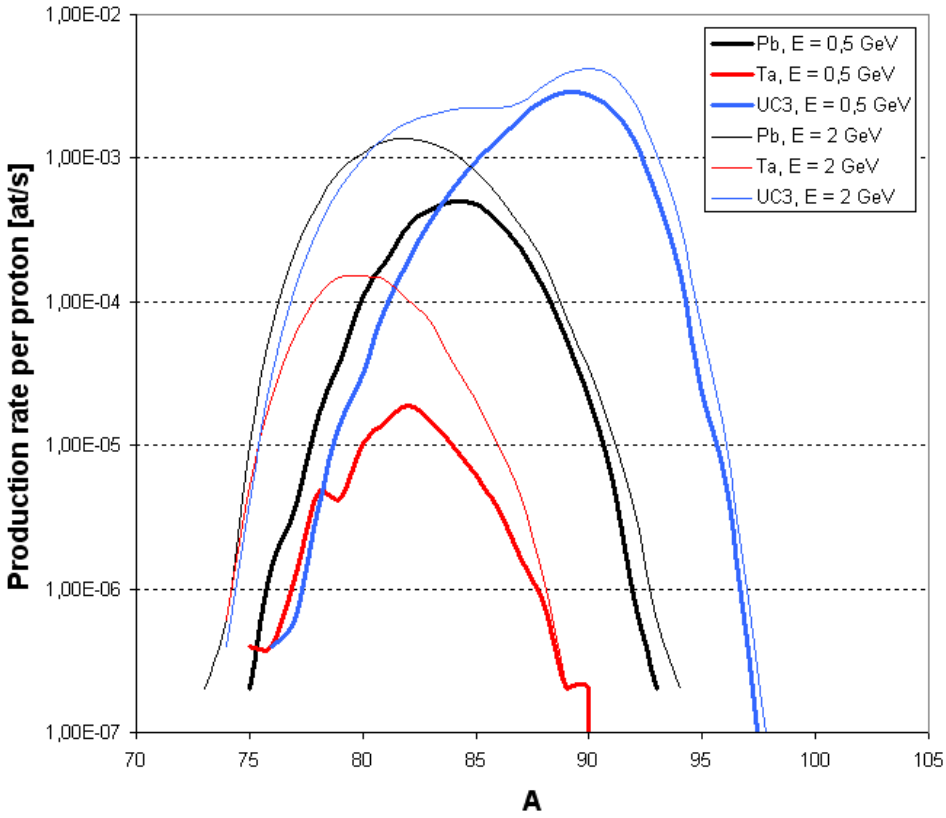

Figure 108: Kr isotopic distribution (R = 18 mm, M = 2 kg, spallation model = INCL4/ABLA, the low energetic secondary neutron flux contribution is taken into account, CINDER evolution time = 1 ms).

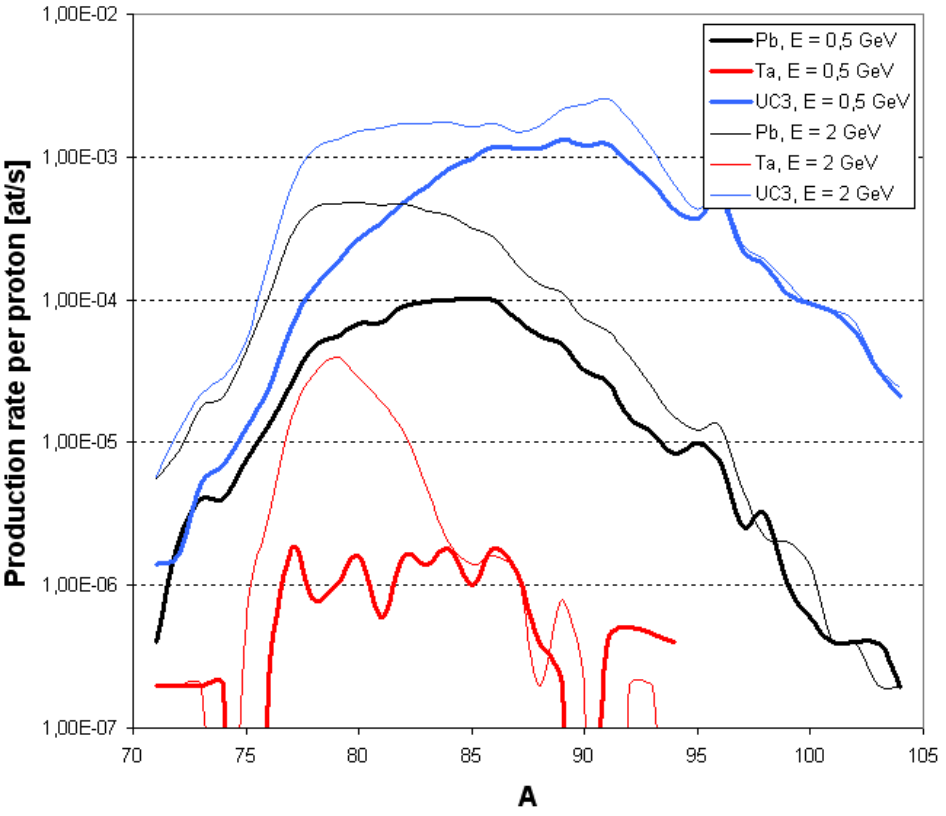

Figure 109: Kr isotopic distribution (R = 18 mm, M = 2 kg, spallation model = CEM2k, the low energetic secondary neutron flux contribution is taken into account, CINDER evolution time = 1 ms).

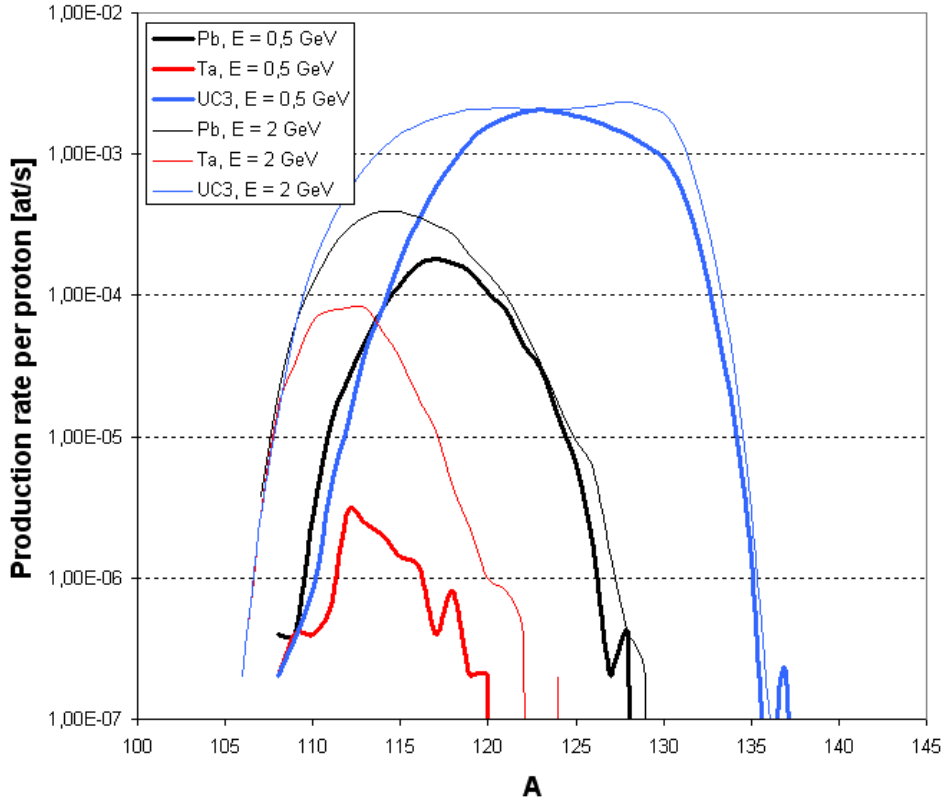

Figure 110: Sn isotopic distribution (R = 18 mm, M = 2 kg, spallation model = INCL4/ABLA, the low energetic secondary neutron flux contribution is taken into account, CINDER evolution time = 1 ms).

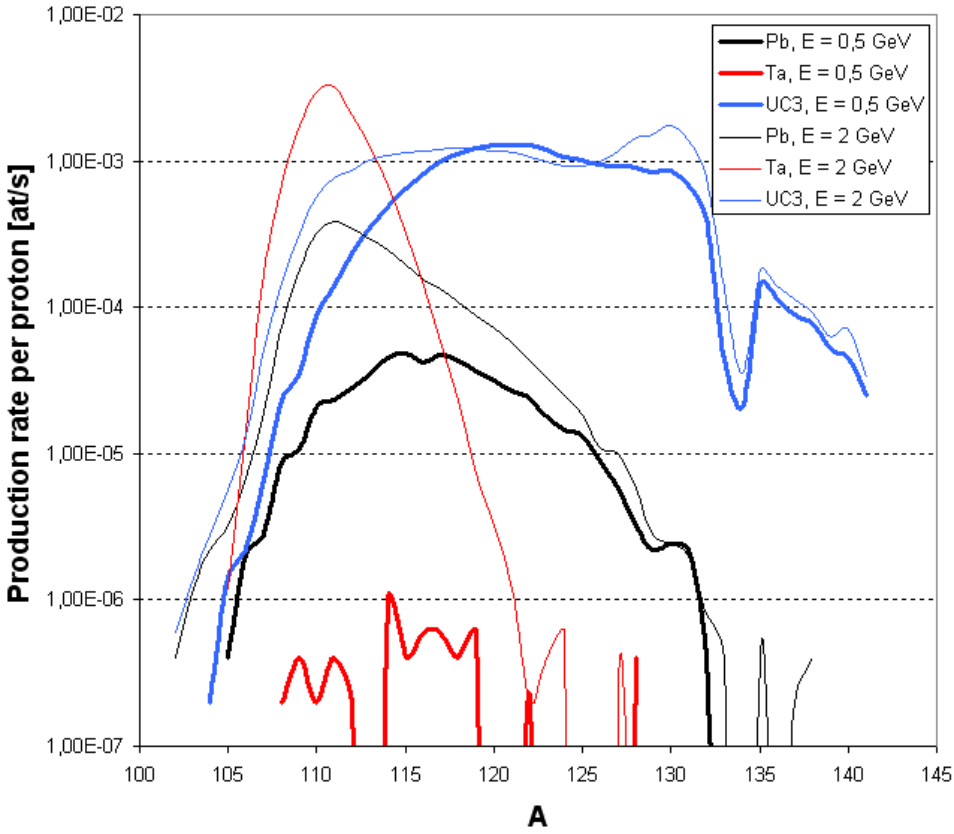

Figure 111: Sn isotopic distribution (R = 18 mm, M = 2 kg, spallation model = CEM2k, the low energetic secondary neutron flux contribution is taken into account, CINDER evolution time = 1 ms).

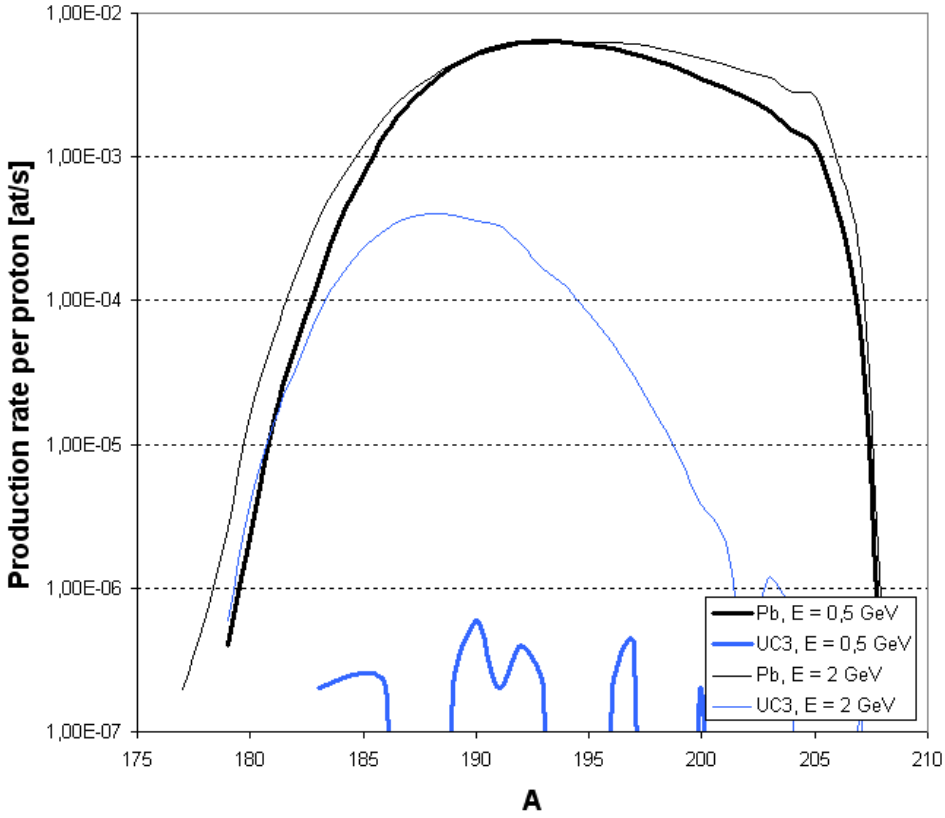

Figure 112: Hg isotopic distribution (R = 18 mm, M = 2 kg, spallation model = INCL4/ABLA, the low energetic secondary neutron flux contribution is taken into account, CINDER evolution time = 1 ms).

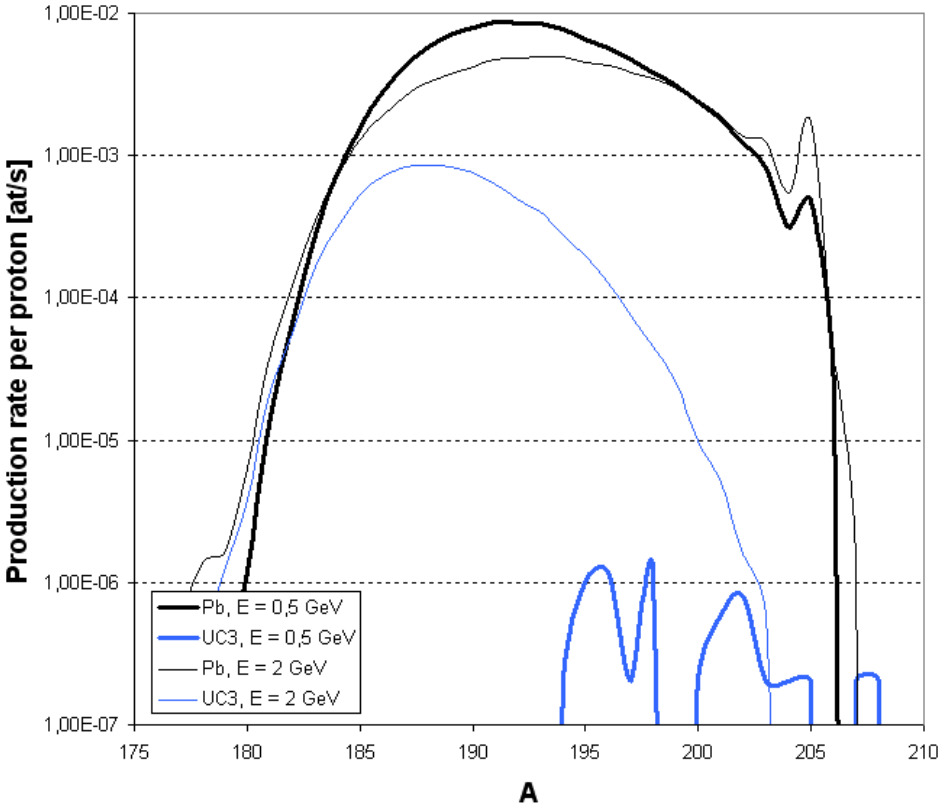

Figure 113: Hg isotopic distribution (R = 18 mm, M = 2 kg, spallation model = CEM2k, the low energetic secondary neutron flux contribution is taken into account, CINDER evolution time = 1 ms).

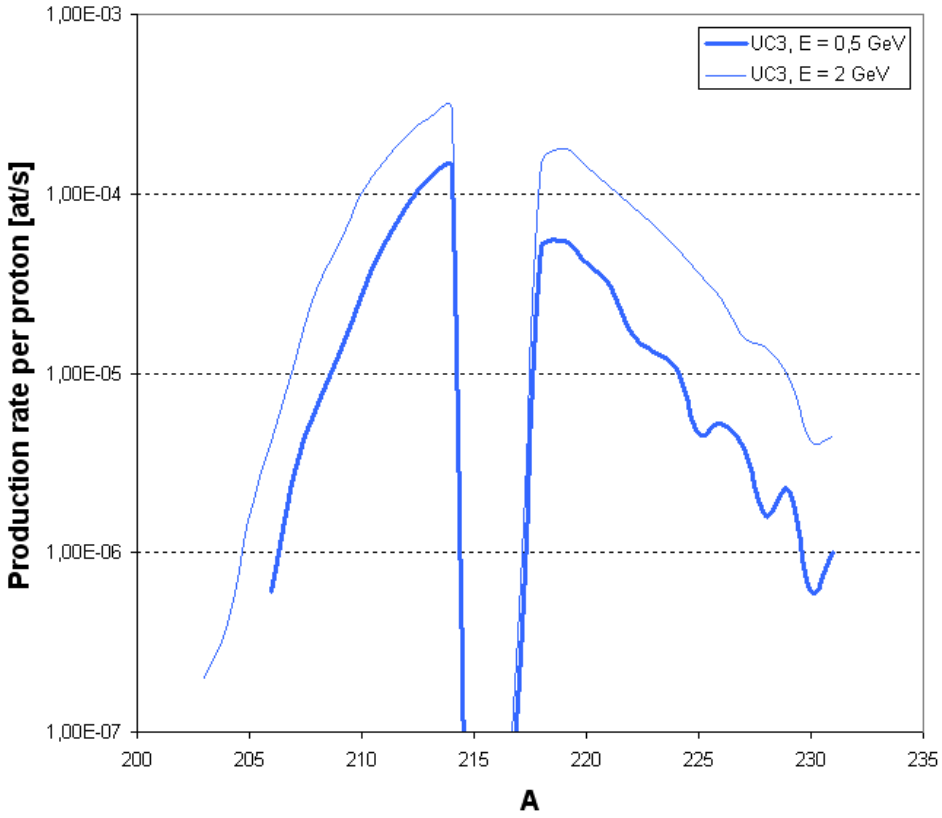

Figure 114: Fr isotopic distribution (R = 18 mm, M = 2 kg, spallation model = INCL4/ABLA, the low energetic secondary neutron flux contribution is taken into account, CINDER evolution time = 1 ms).

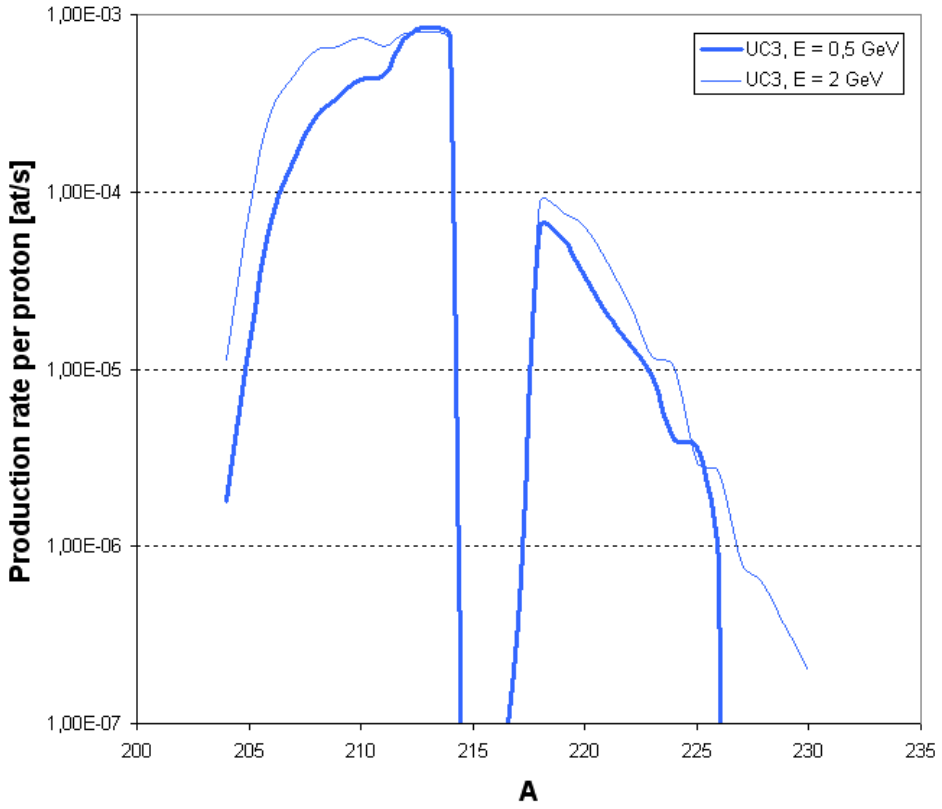

Figure 115: Fr isotopic distribution (R = 18 mm, M = 2 kg, spallation model = CEM2k, the low energetic secondary neutron flux contribution is taken into account, CINDER evolution time = 1 ms).

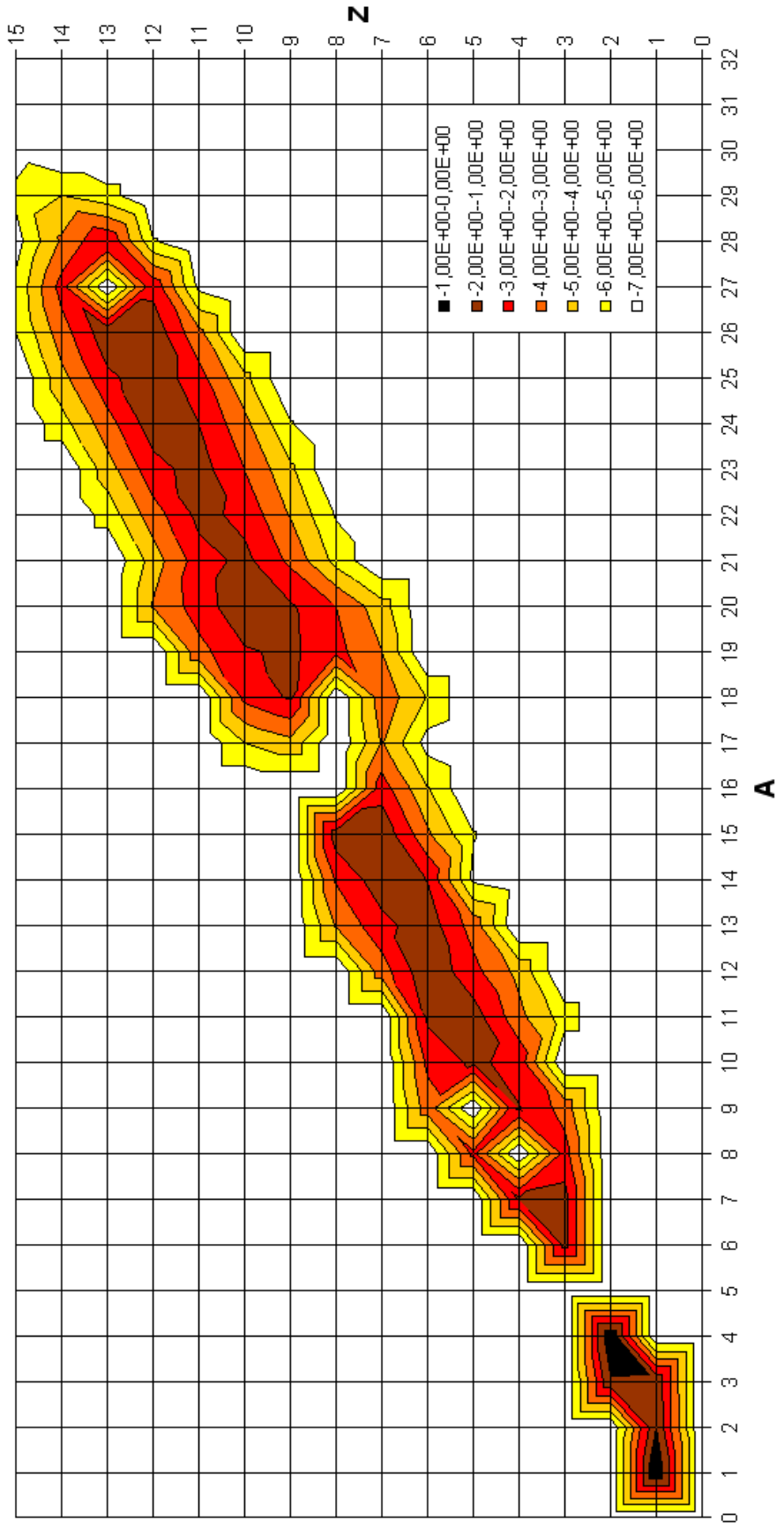

Figure 116: Nuclei production rate per incident proton [s^{-1}] in logarithmic scale (target = Al_2O_3, E = 1 GeV, R = 18 mm, L = 100 cm, model = INCL4/ABLA, the low energetic secondary neutron flux is taken into account, CINDER evolution time = 1 ms).

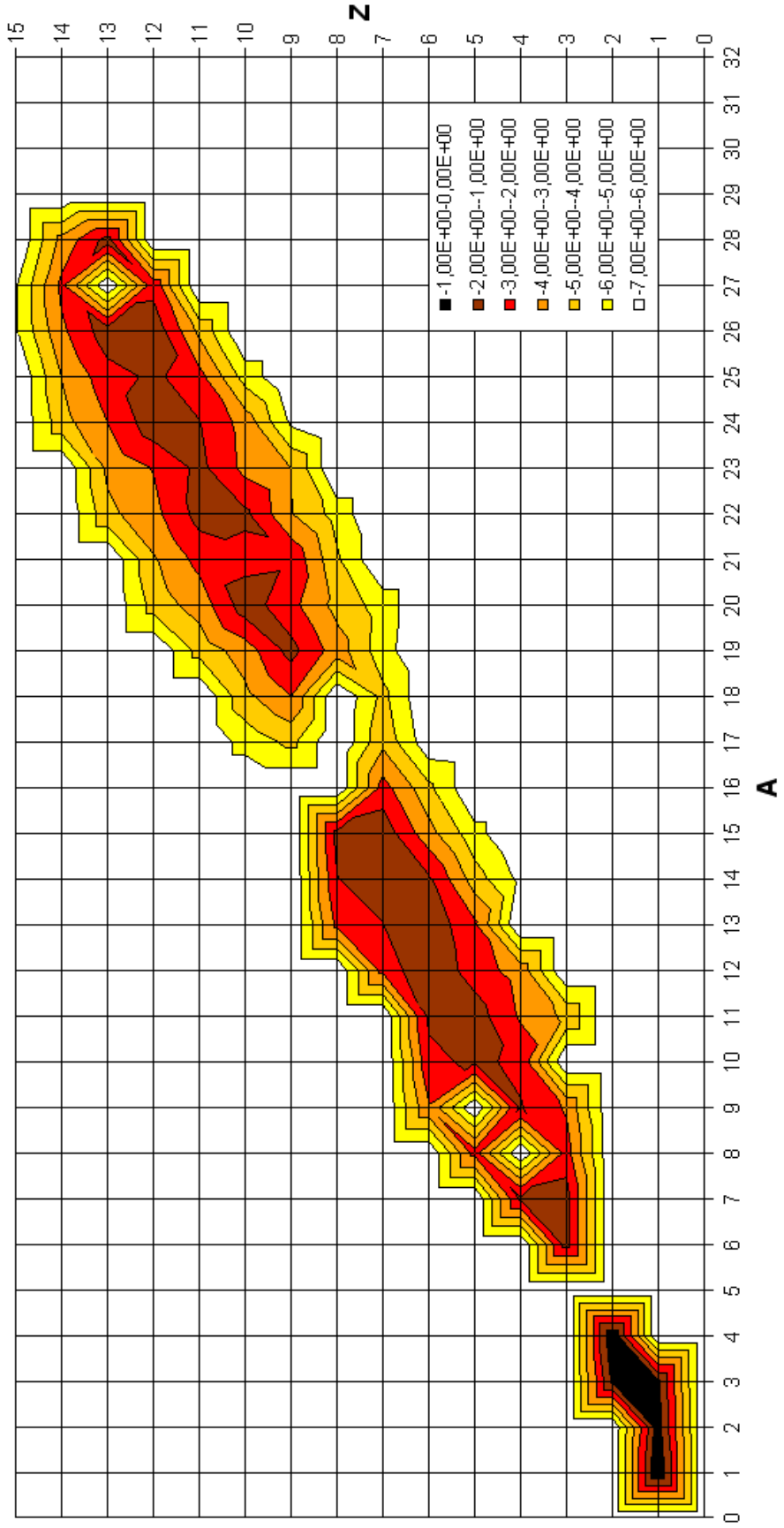

Figure 117: Nuclei production rate per incident proton [s^{-1}] in logarithmic scale (target = Al_2O_3, E = 1 GeV, R = 18 mm, L = 100 cm, model = CEM2k, the low energetic secondary neutron flux is taken into account, CINDER evolution time = 1 ms).

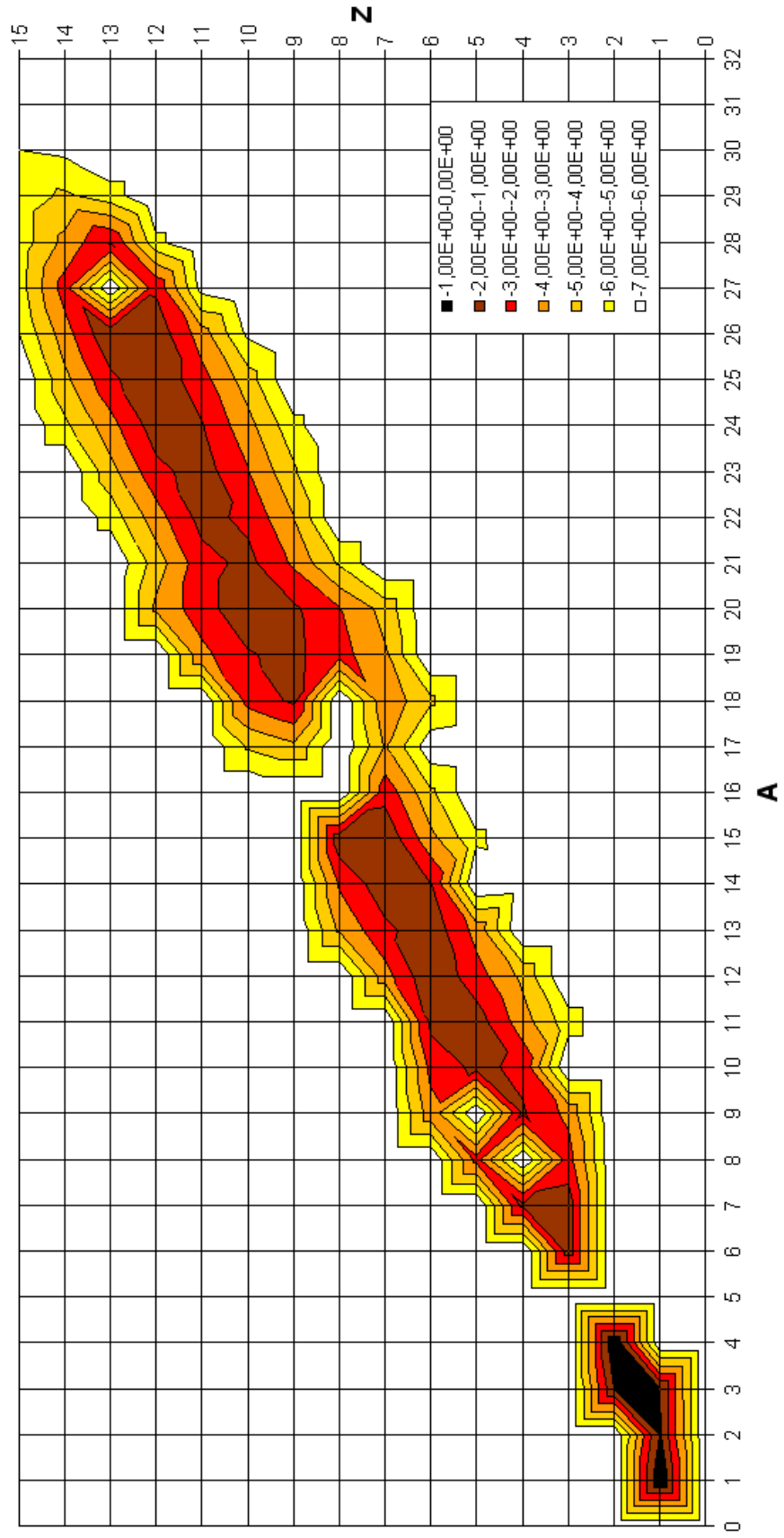

Figure 118: Nuclei production rate per incident proton [s^{-1}] in logarithmic scale (target = Al_2O_3, E = 2 GeV, R = 18 mm, L = 100 cm, model = INCL4/ABLA, the low energetic secondary neutron flux is taken into account, CINDER evolution time = 1 ms).

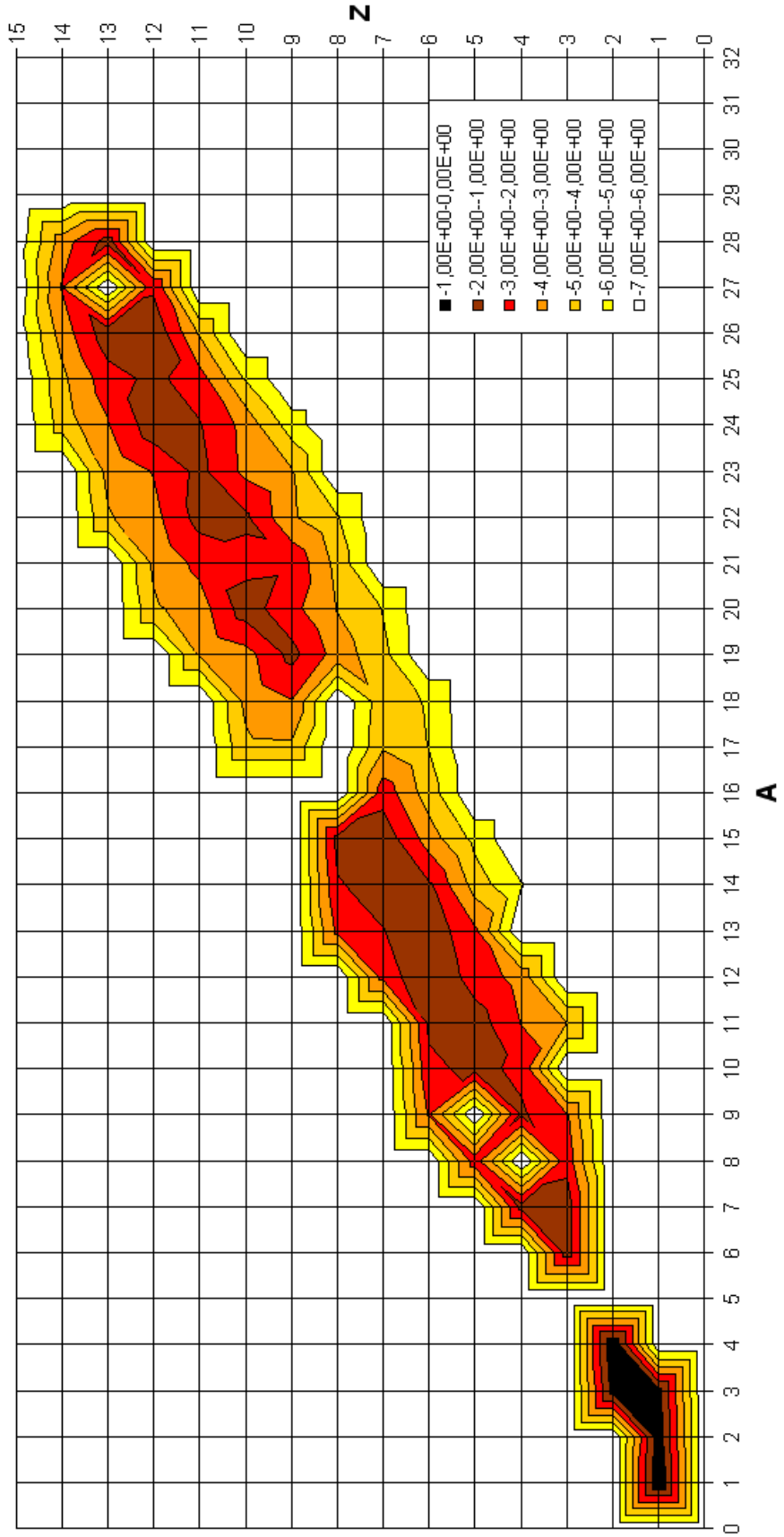

Figure 119: Nuclei production rate per incident proton [s^{-1}] in logarithmic scale (target = Al_2O_3, E = 2 GeV, R = 18 mm, L = 100 cm, model = CEM2k, the low energetic secondary neutron flux is taken into account, CINDER evolution time = 1 ms).

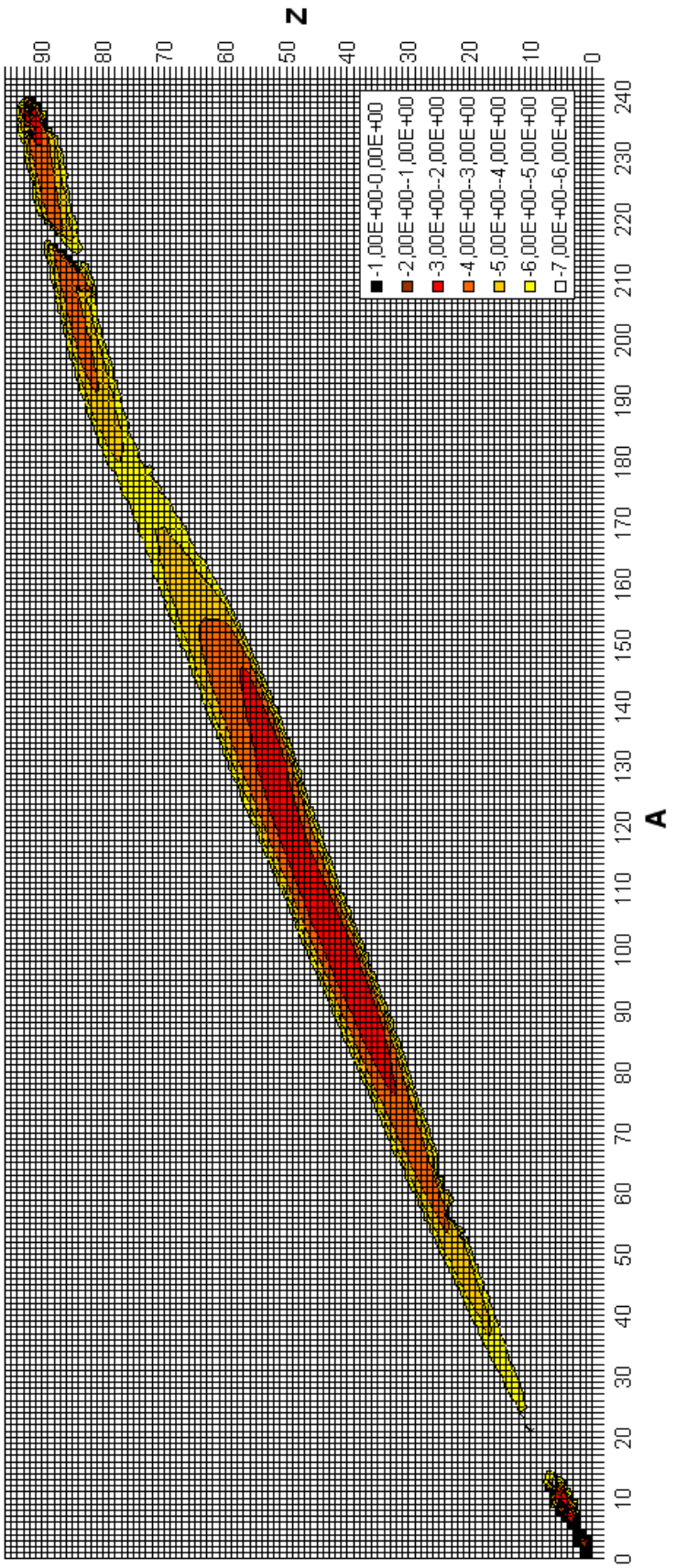

Figure 120: Nuclei production rate per incident proton [s^{-1}] in logarithmic scale (target = UC_3, E = 1 GeV, R = 18 mm, L = 80 cm, model = INCL4/ABLA, the low energetic secondary neutron flux is taken into account, CINDER evolution time = 1 ms).

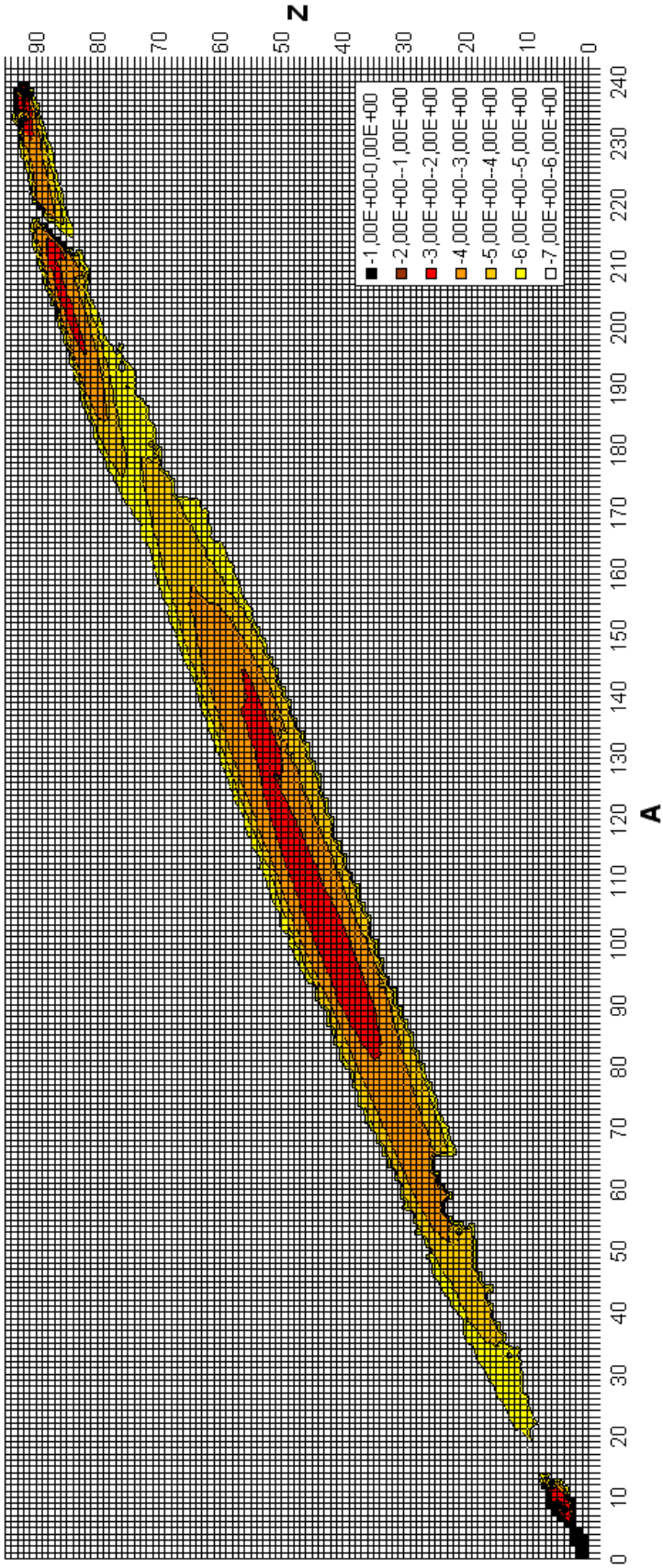

Figure 121: Nuclei production rate per incident proton [s^{-1}] in logarithmic scale (target = UC_3, E = 1 GeV, R = 18 mm, L = 80 cm, model = CEM2k, the low energetic secondary neutron flux is taken into account, CINDER evolution time = 1 ms).

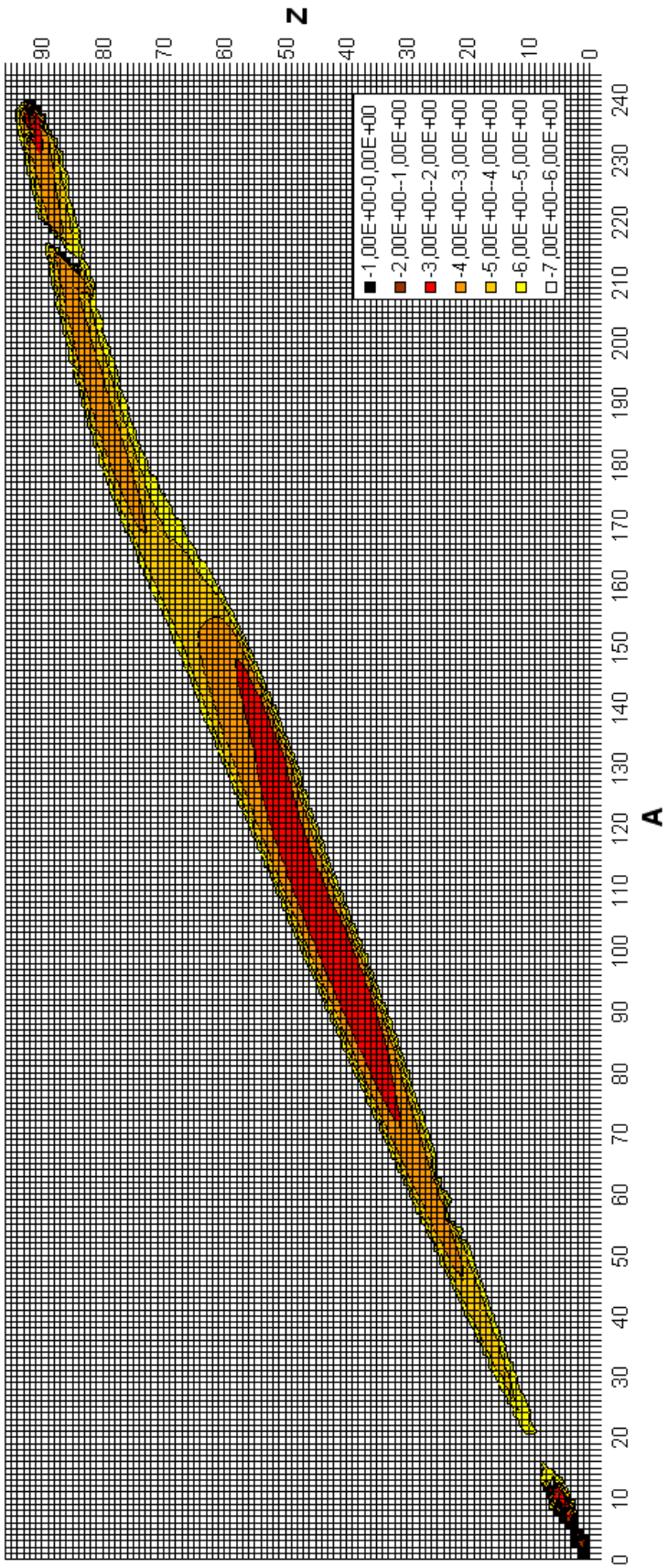

Figure 122: Nuclei production rate per incident proton [s^{-1}] in logarithmic scale (target = UC_3, E = 2 GeV, R = 18 mm, L = 80 cm, model = INCL4/ABLA, the low energetic secondary neutron flux is taken into account, CINDER evolution time = 1 ms).

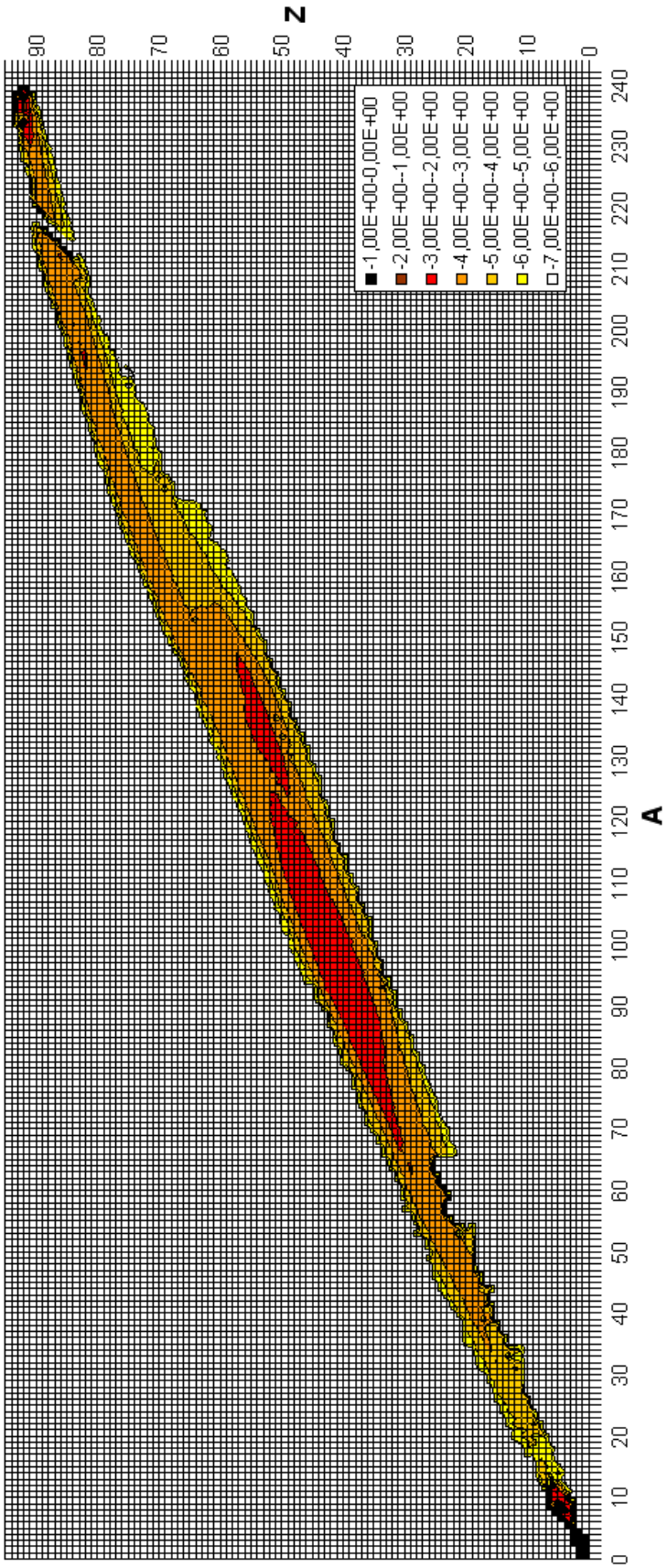

Figure 123: Nuclei production rate per incident proton [s^{-1}] in logarithmic scale (target = UC_3, E = 2 GeV, R = 18 mm, L = 80 cm, model = CEM2k, the low energetic secondary neutron flux is taken into account, CINDER evolution time = 1 ms).